THREE DIMENSIONAL SHAPE MODELING: SEGMENTATION, RECONSTRUCTION AND REGISTRATION

by

Jia Li

A dissertation submitted in partial fulfillment
of the requirements for the degree of
Doctor of Philosophy
(Electrical Engineering: Systems)
in The University of Michigan
2002

Doctoral Committee:

Professor Alfred O. Hero III, Chairperson
Associate Professor Jeffrey A. Fessler
Senior Research Scientist Kenneth F. Koral
Professor Charles R. Meyer

ABSTRACT

THREE DIMENSIONAL SHAPE MODELING: SEGMENTATION,
RECONSTRUCTION AND REGISTRATION

by
Jia Li

Chairperson: Alfred O. Hero III

Accounting for uncertainty in three-dimensional (3D) shapes is important in a large number of scientific and engineering areas, such as biometrics, biomedical imaging, and data mining. It is well known that 3D polar shaped objects can be represented by Fourier descriptors such as spherical harmonics and double Fourier series. However, the statistics of these spectral shape models have not been widely explored. This thesis studies several areas involved in 3D shape modeling, including random field models for statistical shape modeling, optimal shape filtering, parametric active contours for object segmentation and surface reconstruction. It also investigates multi-modal image registration with respect to tumor activity quantification.

Spherical harmonic expansions over the unit sphere not only provide a low dimensional polarimetric parameterization of stochastic shape, but also correspond to the Karhunen-Loéve (K-L) expansion of any isotropic random field on the unit sphere. Spherical harmonic expansions permit estimation and detection tasks, such as optimal shape filtering, object registration, and shape classification, to be performed directly in the spectral do-

main with low complexities. An issue which we address is the effect of center estimation accuracy on the accuracy of polar shape models. A lower bound is derived for the variance of ellipsoid fitting center estimator. Simulation shows that the performance of a maximum likelihood center estimator can approach the bound in low noise situations.

Due to the large number of voxels in 3D images, 3D parametric active contour techniques have very high computational complexity. A novel parametric active contour method with lower computational complexity is proposed in this thesis. A spectral method using double Fourier series as an orthogonal basis is applied to solving elliptic partial differential equations over the unit sphere, which control surface evolution. The complexity of the spectral method is $O(N^2 \log N)$ for a grid size of $N \times N$ as compared to $O(N^3)$ for finite element methods and finite difference methods. A volumetric penalization term is introduced in the energy function of the active contour to prevent the contour from leaking through blurred boundaries.

Multi-modal medical image registration is widely used to quantify tumor activity in radiation therapy patients. Rigid global registration sometimes cannot perfectly overlay the tumor volume of interest (VOI), e.g. segmented from a CT anatomical image, with the apparent position of a tumor in a SPECT functional image. We investigate a new local registration method which aligns the CT and SPECT tumor volumes by maximizing the SPECT intensity within the CT-segmented tumor VOI.

To my parents.

ACKNOWLEDGEMENTS

I would like to thank my dissertation advisor, Professor Alfred O. Hero, for his guidance and suggestions during my graduate course. I have learned considerably through his insight into problems. I owe a debt of gratitude to my associate advisor, Dr. Kenneth F. Koral. This dissertation could not have been done without his financial and spiritual support. I appreciate his tremendous caring about students. I also wish to express my sincere gratitude to Professors Jeffrey A. Fessler and Charles R. Meyer for their helpful discussions concerning my research, and their service on my dissertation committee.

I would like to thank my friends at the University of Michigan, Hua Xie, Bing Ma, Ying Li, Ziyuan Liu and Zhifang Li, for their warm friendship and help in difficult times. As women Ph.D. students, we went through the journey of graduate school and enjoyed our staying at Michigan together.

I am grateful to my husband, Qingchong Liu, for his patience and understanding during the past four years. I also cherish the color that my little daughter brought to me in the rough time. Finally, I would like to thank my parents for their never-ending love, encouragement and support. They created good education opportunities for me in the time of impoverishment and sacrificed a lot to complete me. I dedicate this thesis to my parents.

TABLE OF CONTENTS

LIST OF FIGURES

Figure

LIST OF TABLES

Table

LIST OF APPENDICES

Appendix

CHAPTER I

INTRODUCTION

1.1 Motivation

Enabled by the fast development of imaging techniques and computer hardware, there has been an explosive growth of three-dimensional (3D) image data collected from all kinds of physical sensors. The ability of a computer to properly understand and process these image data has permitted many applications to problems in computer vision and computer graphics. To achieve this ability, the first step is to extract object information from the image data, which can be characterized as an object learning procedure in machine intelligence. Examples of useful object information include: shape; color; texture; size; and its relative location to other objects in the scene. Such object information is widely used in many image processing applications including: 3D cartoon animations; video image processing; target detection in radar images; face recognition in security systems; and tumor dosimetry in nuclear medicine. For tasks geared toward object recognition and reconstruction, shape models are widely studied and used due to their insensitivity to changes in object color and surface texture, and their invariance to translation and scaling.

1.1.1 Statistical Shape Modeling

In the past two decades many shape modeling techniques have been developed for a large variety of applications. The goal of shape modeling is to use as few parameters as possible to describe as many shape details as possible. These two potentially conflicting requirements arise in two of the primary tasks of shape modeling: 1) object recognition; and 2) shape reconstruction. On the one hand, shape modeling should be parsimonious; one should use as few model parameters as possible so that the 3D objects can be efficiently stored and retrieved in object databases of manageable size for object matching and recognition. On the other hand, for the purpose of visual reconstruction, shape modeling should capture finer details, e.g., the high spatial frequencies in the shape. Development of classes of shape models that can bridge the gap between recognition and reconstruction has been an active research area in computer vision and computer graphics [34, 35, 54, 96, 99].

Although deterministic models are successfully employed in many applications, these models are incapable of reflecting any noise or other random variations within a class of shapes. In medical imaging, for instance, anatomical shape can change significantly during a treatment. It is highly desirable to have reliable statistical shape models that can characterize typical ranges of shape variation and capture meaningful statistical information. This information can be used to develop optimal algorithms for noise removal, object registration and segmentation, and establish tight bounds on achievable performance.

1.1.2 Image Segmentation and Registration in Medical Image Analysis

Heavily influenced by the fast development of image acquisition equipment, medical image analysis has evolved in the last twenty years from a multiplicity of directions. Among all the techniques, image segmentation and multi-modal image registration are of special interests to us because they are intensively used to quantify tumor activity in pa-

tients being treated by radiopharmaceutical therapy. Our research was partially supported by a grant awarded by National Cancer Institute. The broad, long-term objectives of the grant research are: 1)accurate tumor dosimetry from external imaging, and 2) effective-and-resource-conserving treatment of patients with malignant follicular lymphoma by the infusion of I-131 labeled anti-B1 monoclonal antibody (MAb) following infusion of a predose of non-radioactive anti-B1 MAb.

Image segmentation is a fundamental task in medical image analysis. In segmentation, objects of interest in the image are extracted so that we can analyze their properties. Such properties can include pixel (voxel) intensities; centroid location; shape and orientation. The information from object segmentations is routinely used in many different applications, such as: diagnosis [95]; treatment planning [65]; study of anatomical structure [33]; organ motion tracking [53]; and computer-aided surgery [5]. Object segmentation and statistical shape modeling serve and rely on each other. Figure 1.1 illustrates such a relationship. On the one hand, object segmentation generates noisy surface data which can be used to identify a shape model. On the other hand, statistical shape information acquired through estimated parameters in a statistical shape model can guide the segmentation procedure. Other applications, such as object registration, shape denoising and shape classification, can be enhanced by accurate object segmentation and statistical shape modeling.

Due to noise and sampling artifacts in medical images, conventional edge detection and thresholding techniques either fail to locate the object boundary or generate invalid boundaries that must be removed in a post-processing step. Deformable models have been developed to address these difficulties [27, 63, 77, 78]. Deformable models are curves and surfaces defined within an image domain that can deform under different forces to locate object boundaries. A more detailed description of deformable models will be given in

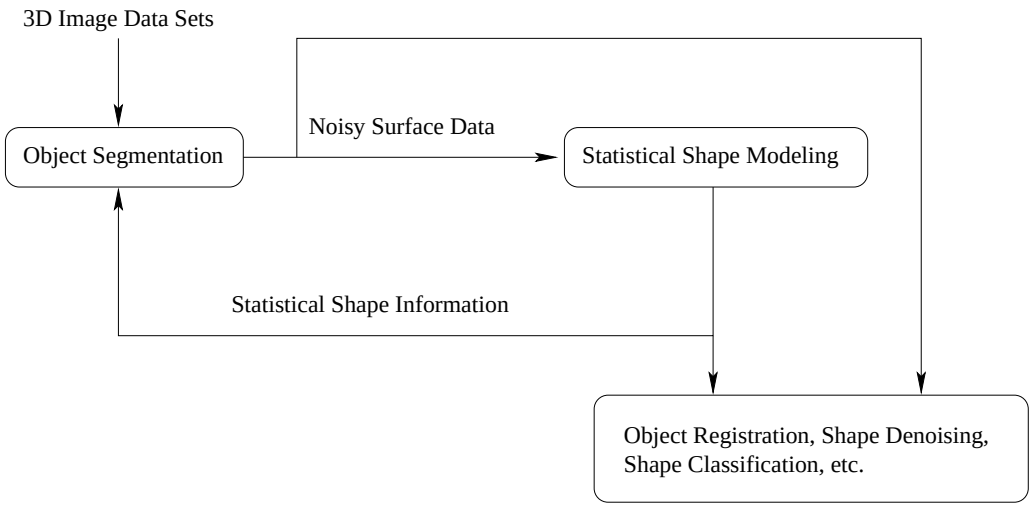

Figure 1.1: Relationship between image segmentation and shape modeling

Section 1.2.2. Although the existing deformable models can achieve satisfying results in 2D images, all of them have met difficulties in 3D imaging. The large number of voxels in 3D images causes significant growth of computational complexity, which is intolerable in most practical applications. This motivates us to find fast algorithms for 3D image segmentation.

Image registration is a classical procedure in image processing and analysis. It aligns two set of images so that corresponding coordinate points in the two images reflect the same physical location of the scene or 3D volume being imaged. Usually, the two set of images are obtained at different times, through different sensing systems, or from different viewpoints, so matching the two images allows us to compare or integrate the information contained in them. Due to the large diversity of data types in different applications, a wide range of techniques has been developed for different applications. These techniques can be classified either by the addressed registration problems or by the adopted methodologies. A good survey of these techniques is given in [17]. The focal application in this research is multi-modal medical image registration for tumor activity quantification. In this application, we must integrate structural information from computed tomography

images (CT) or magnetic resonance images (MRI) with functional information from radionucleic scanners such as positron emission tomography (PET) or single photon emission computed tomographys (SPECT). Such integration is necessary for anatomically locating and quantifying radioisotope uptake. Rigid registration methods that are driven by global measures, such as mutual information between two image sets, may have to sacrifice local fitting accuracy to achieve an optimal global volume registration. Such registrations may not yield an optimal estimate of the location of small tumors. This motivates us to find a local measure of fitting goodness to adjust global registration so that tumor volumes in CT and SPECT are aligned accurately.

1.2 Related Works

1.2.1 Shape Modeling: A General Review

To model a 3D object, we can use either a constructive solid geometry (CSG) representation or a surface boundary representation. Simple CSG descriptions can be specified in terms of a set of 3D volumetric primitives, such as blocks, cylinders, ellipsoids, cones etc., and a set of Boolean operators, such as union, intersection and difference. An advantage of CSG models is that they can accurately represent a simple shape with few parameters. Surface boundary representations, especially the mesh representation [10, 12, 47], use a larger number of parameters and therefore are better suited for reconstruction of complicated shapes. Hybrid modeling which combines the power of the above two modeling approaches has emerged in many applications. In [96], Terzopoulos introduced a hybrid deformable superquadrics model which incorporates the global shape parameters of a conventional superellipsoid with the local degrees of freedom of a spline. Cohen and Han [26, 54] have developed a hybrid hyperquadric by adding an exponential term to the hyperquadric equation which allows synthesis of an arbitrary number of concavities. How-

ever, these hybrid models rely on strong assumptions on the form of the object and need considerable human interaction for computation of the special parameters to characterize the local detail.

Fourier descriptors of surface boundaries have emerged as powerful alternatives to the above models. This kind of model represents the shape of polar surfaces in a linear combination of orthonormal basis functions and provides a radial surface description with respect to a selected origin inside the object. The basis functions are not limited to sinusoids; other orthogonal polynomials, such as spherical harmonics, are possible too. In [86], Persoon and Fu introduced Fourier descriptors for 2D curve representation. Staib and Duncan [92, 93] extended the technique of [86] to deformable templates in both 2D and 3D, and applied them to boundary localization. In [76], Matheny compared the errors of fitting various surface harmonics to an assortment of synthetic data and real range data obtained from laser scan of surfaces. In [53], anatomical shapes were studied and modeled by spherical harmonics. Fourier descriptors are attractive because they have the following features. First, the sets of Fourier basis functions are complete over the space of polar surfaces. Therefore any continuous and finite surface can be expanded as a linear combination of the countably infinite Fourier basis functions. Second, the basis functions are linear independent, which makes the corresponding parameters in the decomposition unique. Third, the basis functions are ordered in spatial frequency. This facilitates hierarchical "multi-resolution" shape decomposition where the truncation of the series controls the smoothness of the reconstruction. These properties make Fourier descriptors very useful both in object recognition and shape reconstruction. In object recognition, low order coefficients can be kept. The objects can be easily stored and retrieved in the databases because of the small size and hierarchical organization of the data structure. In the shape reconstruction problem, we can easily determine the truncation points according to a user-

specified accuracy requirement. There are two disadvantages of Fourier descriptors. One is that object center has to be estimated in advance. Another is that a large number of parameters must be employed to recover very fine details of the object because Fourier descriptors use global basis functions.

Many researchers have explored the area of statistical shape modeling [30, 45, 93, 103, 115]. The common procedure of these approaches is as follows: First extract shape features or shape parameters from training data sets. These features may include labeled "landmark" points [30, 45]; coefficients of the Fourier series [93]; or distance map [71]. Next, compute the mean and variance of the shape or shape parameters from the features extracted in the first step. Usually principle component analysis (PCA) is used to compute variance and characterize typical variations of the shape. Finally, the statistical properties of the shape are incorporated into a image processing algorithm to accomplish registration and segmentation.

Our approach is related to Staib's deformation model [93, 103] since we also use Fourier series as basis functions to model 3-D shapes. The novelty of our approach lies in treating the coarse segmentation result as a random field over the unit sphere and using the spectral theory of random fields over the sphere to obtain statistically uncorrelated shape parameters. Since 1950's, mathematicians have studied random field models for applications in earth science, astrophysics and electrical field theory [1]. Image processing researchers have used random field models for texture synthesis and classification [116, 40], and image segmentation [115]. Curiously, in shape modeling and analysis, random field models have not been widely studied. In this thesis, we propose an isotropic random field model for randomly oriented 3D star-shaped objects using spherical harmonics as the eigen-functions in a Karhunen-Loéve expansion of the random field. Based on the spectral theory of isotropic random fields, we address two problems. The first one

is optimal shape filtering: given noisy samples of surface boundary points, e.g. coarsely segmented from an object, find an optimal estimate of the true surface boundary. Using Wiener filtering theory, an orthogonal representation of random fields is applied to find the linear minimum mean square error surface estimator. The second problem is the 3D object registration problem. In [19] and [20], Burel proposed that spherical harmonics can be used to decompose 3D shapes to get invariants for object orientation estimation. Based on Burel's method and the statistical shape model developed in this thesis, we design a maximum likelihood estimator which can simultaneously estimate the spherical harmonic coefficients and register two 3D objects of different orientations.

We next turn to the problem of selecting the origin in the polar object representation. The accuracy and efficiency of Fourier descriptors are highly dependent on the choice of origin in the coordinate system. In [76], an ellipsoid fitting method was shown to be a good center estimation method for convex shapes. To link the accuracy of center estimation with the accuracy of shape modeling, we study the statistical properties of the center estimator. Both our theoretical derivation and our experimental results show that this center estimator is an efficient maximum likelihood estimator under low power Gaussian noise condition.

1.2.2 Image Segmentation and Registration

As pointed out in a survey by McInerney [77], deformable models (active contours) offer a unique and powerful approach to image analysis that combines geometry, physics, and approximation theory. Furthermore, the application of deformable contour models to segment structures in 2D and 3D images have recently enabled many advances in medical image analysis [22, 21, 27, 26, 52, 63, 75, 78, 108].

There are basically two types of deformable models (active contours): parametric deformable models [27, 26, 52, 63, 78, 108] and geometric deformable models [22, 21, 75].

The class of parametric deformable models originates from the “snake” introduced by Kass [63] which uses an energy-minimizing curve to locate boundaries in 2D imagery. The curve is obtained by solving an optimization problem to minimize the sum of an internal energy function, which penalizes curve roughness in the model, and an external energy function which attracts the curve to object boundary. Any modeling approach applied to this class must deal with sensitivities to initialization and noise. Different approaches adopt different internal and external energy functions. Chapter V will discuss the internal and external functions in detail for both 2D and 3D images. The geometric deformable models were proposed independently by Caselles in [21] and by Malladi in [75]. These methods are based on iterative optimization via the theory of curve evolution and are implemented via level set techniques. Unlike parametric active contours, which represent the contour explicitly as parameterized curves or surfaces, geometric active contours represent the evolving contour implicitly by a special level set function. This kind of evolving contour can split and merge freely without previous knowledge of the number of objects in the scene. In other words, such an evolving contour can handle the topology change automatically. The disadvantage of geometric active contours is that their computational complexity is much higher than that of parametric active contours. The level set function used by geometric active contour is defined over a 2D (3D) grid in the image plain (volume). In every evolution iteration, the geometric active contour method has to update the level set function at every grid point or at least at the grid points in a narrow band near the propagating front, which causes a heavy computational burden. This technique is especially burdensome for 3D images. Table 1.2.2 is taken from [36], which summarizes the advantages and disadvantages of parametric deformable models and geometric deformable models.

Although parametric deformable models usually have lower computational complexity

Table 1.1: Properties of parametric and geometric active contours. (From [36])

	Parametric Contours	Geometric Contours
Efficiency	⋆⋆⋆	⋆
Ease of Implementation	⋆⋆⋆	⋆⋆
Topology Change	No	Yes
Open Contours	Yes	No
Interactivity	Good	Poor

than geometric deformable models, they are still not very efficient in solving 3D segmentation problems. Parametric deformable models are implemented through minimizing an energy function via variational principles, which often leads to solving partial differential equations (PDE) for the surface function. Iterative methods, such as finite element methods (FEM) [27] and finite difference methods (FDM) [108] have been used to solve PDE's involved in this optimization problem. However, FEM/FDM have met difficulties for 3D imaging applications. The large number of voxels in 3D images causes significant growth of computation time which is intolerable in most practical applications. It is well known that spectral methods have a faster rate of convergence than that of FDM and FEM in solving PDE's [50]. This motivates us to explore the application of spectral methods to reduce the computation time for 3D deformable models. Based on the spherical geometry of star-shaped surfaces, we propose to use double Fourier series to solve the PDE defined over the unit sphere. The method is applied to segment both synthesized 3D images and X-ray CT images. It is shown that the new method preserves the merits of other parametric active contour methods while significantly reducing the computation time. Due to the generality of our mathematical formulation, the method can be easily applied to solve the surface reconstruction problem.

Over the past three decades, the very active research in the area of image registration has produced several different registration methods. The fundamental task of image reg-

istration is to find the spatial transformation needed to properly overlay two images. As explained in [17], this task can be decomposed into four major steps. The first step is to decide on the feature space to use for matching the images. Examples of commonly used features include: image intensities; extracted edges; corners; line intersections and centroids. The second step is to choose a similarity measure which evaluates the closeness of the feature set extracted from each image. The third step is to parameterize the spatial transformation. And the fourth step is to specify the searching strategies over these parameters in order to maximize the similarity measure. Two broad categories of registration techniques can be identified. First are those techniques that are based on salient features or surface, such as control-point matching or surface correlation. Here some form of anatomical structures has to be identified or segmented before registration. Salient features refer to specific pixels in the image which contain information indicating the presence of an easily distinguished meaningful characteristic in the image. The second category is based on matching image pixel (voxel) intensities. This category includes mutual information (MI) based registration techniques [100], which minimize the entropy of the joint histogram of grey level values of the two images. Both control-point matching [18, 49, 69, 74, 79] and pixel intensity techniques [28, 80, 100] are in common use for clinical applications.

For applications of radiotherapy treatment planning and response monitoring, it is often necessary to fuse SPECT and CT data sets so that the functional information and anatomical information can be integrated. Due to the low spatial resolution of SPECT, the ultimate accuracy of the estimate of tumor activity in therapy patients using CT-SPECT fusion is difficult to establish. Inaccuracy can be caused by “registration error” which in turn comes from several factors. Depending on the type of registration used, these factors include: 1) a non-rigid change in the body habitus between CT and SPECT, 2) a change in the tumor location relative to the large organs or relative to the skin markers, 3) a poor

choice of the control points that initialize a mutual information (MI) based registration, 4) a non-optimum choice of other parameters in MI registration, 5) a failure of maximum MI to yield a good registration even with the optimal choice of input parameters. In our application, we have noticed that a tumor volume of interest (VOI) from CT sometimes does not perfectly overlay the true position of the tumor in the SPECT image set. Furthermore, the magnitude of the difference between the activity estimate from the MI registration procedure and that from a perfect overlay is uncertain. As alternative, we explore the possibility of optimizing the estimate of tumor location and orientation with respect to within-VOI activity quantification. Control points matching or mutual information based registration is used to obtain an initial rigid transformation between CT and SPECT. A local optimization is then performed to fine tune the initial global registration, with the criterion of maximizing counts in VOIs of known tumors. The local optimization appears to be more resistant to overlay errors.

1.3 Thesis Contributions

The original contributions made by this dissertation are summarized as follows.

- We have compared two Fourier descriptors of 3D polar shapes and studied the related computational issues.

- We have developed a statistical shape model using the spectral theory of isotropic random field. We have proved that if the orientation of a 3D polar object is uniformly distributed in $SO(3)$, the observed radial function of this 3D object is an isotropic random field over the unit sphere S^2.

- For center estimation problem, we have established that the estimator of the ellipsoid parameter vector proposed by Bookstein is a maximum likelihood estimator when

the segmentation noise is Gaussian with low variance. A lower bound has also been derived for the variance of the center estimator under a Gaussian segmentation noise model.

- We have proposed a statistical shape model and a Wiener filtering strategy for optimal shape filtering.
- We have developed a maximum likelihood method to jointly estimate shape parameters and 3D rotation angles based on an isotropic Gaussian noise model.
- We have developed a fast algorithm for 3D object segmentation and surface reconstruction by applying spectral methods to solve elliptic PDE's over the unit sphere. We have introduced volumetric penalization to prevent contour leaking at broken boundaries or spurious edges.
- We have proposed a refinement of MI-based rigid CT-SPECT registration which enhances robustness by maximizing counts in segmented volumes of interest.

1.4 Organization of Thesis

This thesis is organized as follows. In Chapter II, we study spherical harmonics and double Fourier series on the sphere as two Fourier descriptors of surface boundaries. Related computational issues are discussed. The two descriptors are compared in terms of convergence rate and shape modeling accuracy. Chapter II also studies the statistical properties of the segmentation error and develops an orthogonal representation of isotropic random field over the unit sphere. The detailed proof of the Karhunen-Loéve expansion formula is also given in this chapter. In Chapter III, we investigate the center estimation problem for 3D shape. The ellipsoid fitting method proposed by Bookstein is described

and shown to be a maximum likelihood estimator of ellipsoid parameters when the segmentation noise level is low. A lower bound is derived to evaluate the performance of the ellipsoid fitting center estimator. In Chapter IV, two applications of statistical shape models are presented. The first application is Wiener filtering of a noisy surface boundary. The second application is joint estimation of shape parameters and 3D rotation angles by maximum likelihood. In Chapter V, a fast algorithm for 3D surface reconstruction and object segmentation is developed based on our shape modeling approach and solving PDE by double Fourier series expansion methods. A volumetric penalization term is introduced in the PDE to prevent contour leakage at broken or blurred boundaries. The segmentation is evaluated for both real medical images and synthesized images. Chapter VI proposes an adjustment to rigid CT-SPECT registration so as to better quantify tumor uptakes. Finally, Chapter VII contains conclusions and directions of future work related to this research.

CHAPTER II

STATISTICAL POLAR SHAPE MODELING BY FOURIER DESCRIPTORS

2.1 Introduction

Techniques of three dimensional shape modeling have been widely studied over the past two decades [9][30][93] [115][103]. Generally speaking, shape modeling is a fundamental process of combining physical measurement of objects with a mathematical model. In many computer vision related areas, such as pattern recognition, deformation and motion analysis, image registration and image retrieval, shape modeling techniques have been integrated with other techniques to achieve different goals. Models widely used in these applications include constructive solid geometry and surface boundary representations. In the rest of this thesis, "shape modeling" refers to surface boundary representations. Deterministic surface descriptions, such as polygons, B-splines and Fourier descriptors, have been well established [9]. Among these descriptions, the parametric representations that are object-centered and use a linear combination of basis functions, are of special interest to us. These mappings from spatial object space to parameter space provide a compact representation of the object and are useful for shape storage and reconstruction, noise filtering, and pattern recognition.

In this chapter, we investigate the properties of spherical harmonics and double Fourier

series as two Fourier descriptors for 3D polar shape modeling. We investigate both deterministic and statistic formulations of polar surface approximation. This chapter is organized as follows. Section 2.2 discusses the theoretical expression and computational issue of spherical harmonics and double Fourier Series. These two descriptors are compared in terms of convergence rate and shape modeling accuracy. Section 2.3 studies the statistical properties of the segmentation error and develops the orthogonal representation of isotropic random fields for statistical shape modeling. The detailed proof of the spectral theory is also given in this section. As it will be shown in Chapter IV, the spectral representation of isotropic random field can be applied to several tasks in image processing such as: Wiener filtering; shape classification; and object registration.

2.2 Deterministic Polar Shape Modeling by Fourier Descriptors

The main process of 3D deterministic shape modeling includes the following steps: 1) find the proper basis functions; 2) sample the 3D object surface; 3) compute the shape parameters through sampling data. The surface of a polar shape (star shape) object can be represented by its radial coordinate r with respect to a selected origin inside the object. r is a single value function of θ and ϕ, where (θ, ϕ) is a direction vector on the unit sphere. The unit sphere is defined as the sphere of radius 1 and centered at origin. Hereafter the unit sphere will be denoted by S^2, and coordinates on S^2 will be described by (θ, ϕ) or x, i.e. $(\theta, \phi) \in S^2$ or $x \in S^2$. To be accurate, 3D polar shapes are defined as shapes that have a boundary function in the form of $f : S^2 \to [0, \infty]$. Figure 2.1 illustrates polar and non-polar shapes in 2D.

Fourier descriptors represent polar shape objects as a linear combination of orthonormal basis functions. In the following, we will study shape modeling by spherical harmonics and double Fourier series over the unit sphere.

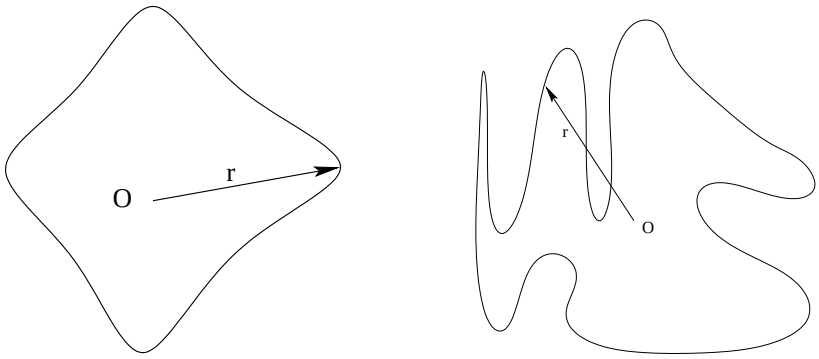

(a) polar shape (b) non-polar shape

Figure 2.1: Surface boundaries of star shape and non-star shape objects.

2.2.1 Spherical Harmonics

Spherical harmonics $\{Y_l^m(\theta, \phi)\}$ are special functions defined on the unit sphere [3] as

$$Y_l^m(\theta, \phi) = (-1)^m \sqrt{\frac{2l+1}{4\pi} \frac{(l-m)!}{(l+m)!}} P_l^m(\cos\theta) e^{im\phi} \tag{2.1}$$

where $\theta \in [0, \pi]$ is the polar angle, $\phi \in [0, 2\pi]$ is the azimuthal angle, $P_l^m(x)$ is the associated Legendre function [Appendix A.2], l is a non-negative integer, m is an integer in $[-l, l]$, and the normalization is chosen such that

$$\int_0^{2\pi} \int_0^{\pi} Y_l^m(\theta, \phi) Y_{l'}^{m'*}(\theta, \phi) \sin\theta d\theta \, d\phi = \delta_{l,l'} \delta_{m,m'}. \tag{2.2}$$

Here Y^* is the complex conjugate of Y, and $\delta_{m,m'}$ is the Kronecker delta function defined as the following

$$\delta_{m,m'} = \begin{cases} 1 & \text{if } m = m^{'}; \\ 0 & \text{otherwise.} \end{cases} \tag{2.3}$$

Figure 2.2 shows the polar angle θ and the azimuthal angle ϕ on the unit sphere.

Spherical harmonics are the angular portion of the solution to the Laplace equation in spherical coordinates, where azimuthal symmetry is not present [3] [Appendix A.1]. They are orthonormal and ordered in spatial frequency as a function of l and m. The set

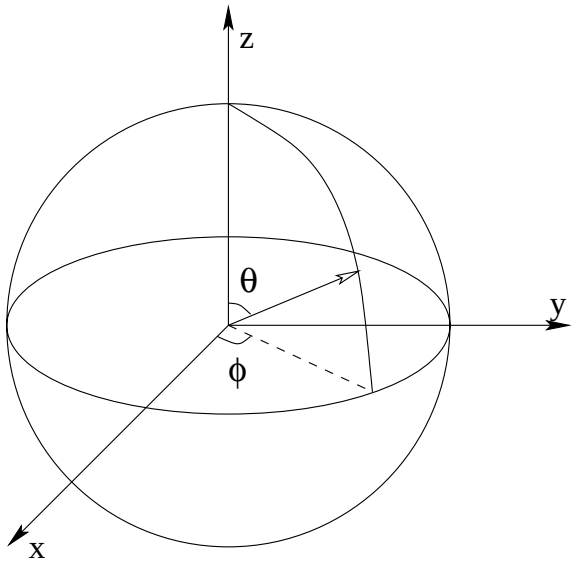

Figure 2.2: Direction vector (θ, ϕ) on the unit sphere. θ is the polar angle and ϕ is the azimuthal angle.

of spherical harmonics is also complete in the space of continuous functions over S^2 of finite energy. Therefore, any radial function $f : S^2 \to \mathbb{R}$, of polar shape object, can be expanded as a linear combination of spherical harmonics:

$$f(\theta, \phi) = \sum_{l=0}^{\infty} \sum_{m=-l}^{l} C_l^m Y_l^m(\theta, \phi) \tag{2.4}$$

where the coefficients C_l^m are uniquely determined by

$$C_l^m = \int_0^{\pi} \int_0^{2\pi} Y_l^{m*}(\theta, \phi) f(\theta, \phi) \sin\theta d\phi \, d\theta. \tag{2.5}$$

The right hand side of (2.4) is called the Laplace series, which converges uniformly. The sufficient conditions for the spherical harmonic expansion are given by Hobson in [59]. The corresponding series coefficients C_l^m are the shape model parameters. Since the values of surface functions are always real, the real and imaginary parts of shape parameters are constrained by the following relations:

$$\Re\{C_l^m\} = \begin{cases} -\Re\{C_l^{-m}\} & \text{m odd} \\ \Re\{C_l^{-m}\} & \text{m even} \end{cases} \tag{2.6}$$

$$\Im\{C_l^m\} = \begin{cases} \Im\{C_l^{-m}\} & \text{m odd} \\ -\Im\{C_l^{-m}\} & \text{m even} \end{cases} \tag{2.7}$$

2.2.2 Computing Laplace Series

As well known by all practitioners, computational complexity is always a big concern in 3D shape modeling. In this subsection, we discuss the computational complexity and the accuracy of modeling 3D polar shapes by spherical harmonics. Two different algorithms to compute the Laplace series, SVD and FFT, are compared in terms of complexity and accuracy.

2.2.2.1 SVD

Using singular value decomposition (SVD) to find the coefficients of spherical harmonics in the sense of least squared error was proposed in [41] and [76]. Let $r(\theta, \phi)$ denote the sample value of the radial coordinate in the direction (θ, ϕ) and $R(\theta, \phi)$ denote the radial function of the reconstructed shape using spherical harmonics. The least squared error approach requires the minimization of the following error function:

$$e = \sum_{(\theta,\phi)\in S_0} [r(\theta, \phi) - R(\theta, \phi)]^2 \tag{2.8}$$

where $S_0 \subset S^2$ is the sample set.

The function $R(\theta, \phi)$ is a Laplace series with complex coefficients. Since $Y_l^m(\theta, \phi)$ is a complex function and $Y_l^{-m}(\theta, \phi) = (-1)^m Y_l^{m*}(\theta, \phi)$, the real and imaginary parts of $Y_l^m(\theta, \phi)$, i.e. $\Re\{Y_l^m(\theta, \phi)\}$ and $\Im\{Y_l^m(\theta, \phi)\}$, are often used as basis functions in place of $Y_l^m(\theta, \phi)$ and $Y_l^{-m}(\theta, \phi)$ to simplify the computation. The functions $U_l^m(\theta, \phi) \triangleq \Re\{Y_l^m(\theta, \phi)\}$ and $V_l^m(\theta, \phi) \triangleq \Im\{Y_l^m(\theta, \phi)\}$ are also called Tesseral harmonics. Then, the reconstructed shape can be represented as

$$R(\theta, \phi) = \sum_{l=0}^{K} \sum_{m=0}^{l} A_l^m \, U_l^m(\theta, \phi) + B_l^m \, V_l^m(\theta, \phi). \tag{2.9}$$

where A_l^m and B_l^m are the coefficients of real values, and K is the highest order of basis functions in the shape modeling, which controls the fineness of surface detail that can be handled. The choice of K affects not only the modeling accuracy, but also the computational complexity for estimating the coefficients $\{A_l^m\}$ and $\{B_l^m\}$. The total number of coefficients is $(K+1)^2$ in equation (2.9). If the maximum likelihood method is employed to estimate the coefficients, which is essentially a nonlinear iterative optimization procedure, the computational complexity will be too high for large value of K. Users have to properly balance the accuracy of shape modeling and the amount of computation according to necessities in their applications.

A group of linear equations can be obtained if we write the equation (2.9) for every sampling direction (θ_i, ϕ_i), where i is the index of the sample set. Write them in matrix format, we have

$$\mathbf{r} = \mathbf{U}\mathbf{a} + \mathbf{V}\mathbf{b}. \tag{2.10}$$

where $\mathbf{r} = (r(\theta_1, \phi_1), \ldots, r(\theta_i, \phi_i), \ldots, r(\theta_N, \phi_N))^T$, $(\theta_i, \phi_i) \in S_0$ is a vector representing sampled surface values, $\mathbf{a} = (A_0^0, A_1^0, A_1^1, A_2^0, A_2^1, A_2^2, \ldots, A_K^K)^T$ and $\mathbf{b} = (B_0^0, B_1^0, B_1^1, B_2^0, B_2^1, B_2^2, \ldots, B$ are coefficients vectors to be estimated, $\mathbf{U}$ and $\mathbf{V}$ are matrices with $U_l^m(\theta_i, \phi_i)$ and $V_l^m(\theta_i, \phi_i)$ as their entries. For instance, $\mathbf{U}$ has the form as following:

$$\mathbf{U} = \begin{pmatrix} U_0^0(\theta_1,\phi_1) & U_1^0(\theta_1,\phi_1) & U_1^1(\theta_1,\phi_1) & \cdots & U_K^K(\theta_1,\phi_1) \\ U_0^0(\theta_2,\phi_2) & U_1^0(\theta_2,\phi_2) & U_1^1(\theta_2,\phi_2) & \cdots & U_K^K(\theta_2,\phi_2) \\ \vdots & \vdots & \vdots & \ddots & \vdots \\ U_0^0(\theta_N,\phi_N) & U_1^0(\theta_N,\phi_N) & U_1^1(\theta_N,\phi_N) & \cdots & U_K^K(\theta_N,\phi_N) \end{pmatrix}. \tag{2.11}$$

Let $\mathbf{X} = (\mathbf{U}, \mathbf{V})$ and $\mathbf{c} = (\mathbf{a}, \mathbf{b})^T$, we can rewrite equation (2.10) in the form:

$$\mathbf{r} = \mathbf{X}\mathbf{c}. \tag{2.12}$$

In this way, all shape parameters are put into a single vector and can be solved simulta-

neously by SVD method. In case where the number of sample points is greater than the number of parameters, the system is called *over-determined.* For over-determined systems, SVD provides a solution for the parameters that is the best approximation in the least square error sense. We can coarsely analyze the computational complexity of SVD method. Let N be the number of sampling points over S^2. To set up the matrix X, the spherical harmonics have to be computed at the N sampling points, which has a complexity of at least $O(N^2)$ for non-uniformly distributed sampling points. The SVD procedure usually has N^3 arithmetic operations. Therefore the computational complexity of this method should be around $O(N^3)$.

2.2.2.2 FFT

The spherical harmonic expansion is an extension of the special Fourier transform on unit sphere. Some researchers have explored fast algorithms similar to the 2D FFT for this expansion [37, 55, 89]. Although spherical harmonics comprise an orthogonal set in the continuous space, they are not orthogonal in discrete cases, such as for the sampled data. To approximate them by an orthogonal set on a discrete domain, we must associate them with weight functions. The difference and analogy of spherical harmonics orthogonal on a discrete set of points on the sphere were studied in [82]. This work makes it possible to adapt FFT analysis to spherical harmonics. It is desirable to sample a band-limited radial function in such a way that the original shape can be exactly recovered from the samples. In [39], Driscoll and Healy developed a sampling theorem and a fast algorithm to reduce the computational complexity of spherical harmonics for band-limited functions on unit sphere. The bandwidth was defined in terms of the highest order of spherical harmonics which have a non-zero coefficient.

Theorem 1 (Sampling Theorem over S^2 [39]) *Let $f(\theta, \phi)$ be a band-limited function on*

S^2 such that $f_l^m = 0$ for $l \geq b$. Then

$$f_l^m = \frac{\sqrt{2\pi}}{2b} \sum_{j=0}^{2b-1} \sum_{k=0}^{2b-1} a_j^{(b)} f(\theta_j, \phi_k) Y_l^{m*}(\theta_j, \phi_k), \tag{2.13}$$

for $l < b$ and $|m| \leq l$. Here f_l^m is the spherical harmonic coefficient of f, $\theta_j = \pi j/2b$, $\phi_k = \pi k/b$, and the coefficients $a_j^{(b)}$ are determined by the equation

$$a_0^{(b)} P_l(\cos\theta_0) + a_1^{(b)} P_l(\cos\theta_1) + \cdots + a_{2b-1}^{(b)} P_l(\cos\theta_{2b-1}) = \sqrt{2}\delta_{l,0}. \tag{2.14}$$

The fast algorithm was named as "FFT" over S^2 and has a computational complexity of $O(N(\log N)^2)$. We will compare its performance with SVD method in the next section.

2.2.2.3 Experimental Results

As aforementioned, both the SVD method and the FFT method can be employed to compute the coefficients in the spherical harmonic expansion. We compare their characters and performance by some experiments. All the computation in the experiment was completed on a Sun Ultra-10 workstation via MATLAB. Four different shapes are modeled by spherical harmonics basis in our experiments. Three of them have global implicit expressions as: $(\frac{x}{10})^2 + (\frac{y}{9})^2 + (\frac{z}{7})^2 = 1$, $x^4 + y^4 + z^4 = 1$ and $(\frac{x}{10})^6 + (\frac{y}{9})^6 + z^6 = 1$. The last one is the surface of a 3D medical organ, a liver manually segmented from X-ray CT image. Figure 2.3 shows these shapes. Notice that some sharp corners of the liver are missing in the shape of liver due to the finite number of spherical harmonic functions used in the model. The normalized residual error of shape modeling is defined as following

$$\text{err}(K) = \frac{\sqrt{\sum_{i=0}^{N-1} \sum_{j=0}^{M-1} [r(\theta_i, \phi_j) - R_K(\theta_i, \phi_j)]^2/(NM)}}{\sum_{i=0}^{N-1} \sum_{j=0}^{M-1} r(\theta_i, \phi_j)/(NM)}, \tag{2.15}$$

where K is the highest order of spherical harmonics employed, $\theta_i = i\frac{\pi}{N}$, $\phi_j = j\frac{2\pi}{M}$, $r(\theta, \phi)$ and $R_K(\theta, \phi)$ represent the original shape and the reconstructed shape respectively. $\text{err}(K)$ is solely caused by the truncation of the Laplace series. For shapes with limited spatial

frequency, such as the unit sphere, err(K) vanishes when K is greater than the radial function bandwidth.

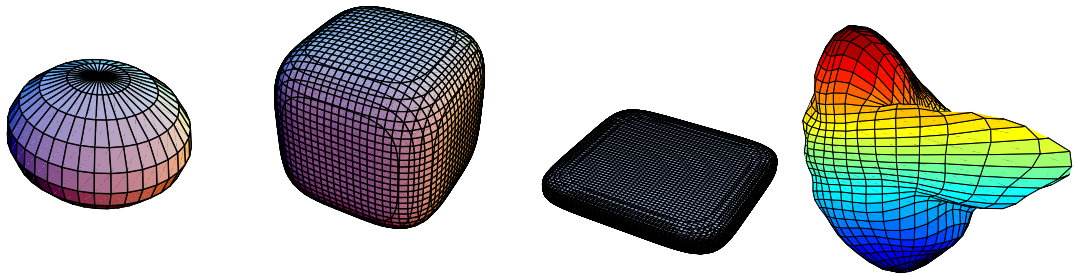

(a) (b) (c) (d)

Figure 2.3: 3D shapes used in the shape modeling experiments: (a) $(\frac{x}{10})^2+(\frac{y}{9})^2+(\frac{z}{7})^2 = 1$; (b) $x^4 + y^4 + z^4 = 1$; (c) $(\frac{x}{10})^6 + (\frac{y}{9})^6 + z^6 = 1$; (d) Segmented liver modeled by spherical harmonics, $K = 14$

First, we test modeling accuracies for different shapes. Figure 2.4 shows the residual error of shape modeling versus the highest order of spherical harmonics employed in the SVD method. It can be seen that the residual errors decrease exponentially with K, the highest order of spherical harmonics used. As expected, the decreasing speed is shape dependent. The more irregular the shape is, the slower is the decreasing speed of the residual modeling error. Using spherical harmonics with the highest order as $K = 14$, the residual error is $1.37 \cdot 10^{-7}$ for the ellipsoidal surface, $1.45 \cdot 10^{-4}$ for the shape defined by $x^4 + y^4 + z^4 = 1$, $3.74 \cdot 10^{-2}$ for the medical organ liver, and $7.95 \cdot 10^{-2}$ for the shape defined by $(\frac{x}{10})^6 + (\frac{y}{9})^6 + z^6 = 1$. One can expect the representation order needed for relevant 3D polar medical objects to be in the range $10 \leq K \leq 20$, and the corresponding magnitudes of residual error be in the range from 10^{-4} to 10^{-2}.

In the second experiment, we compared the accuracies of FFT method and SVD method. The same surface sampling data was used by these two methods. Figure 2.5 plot the residual error of shape modeling versus the highest order of spherical harmonics

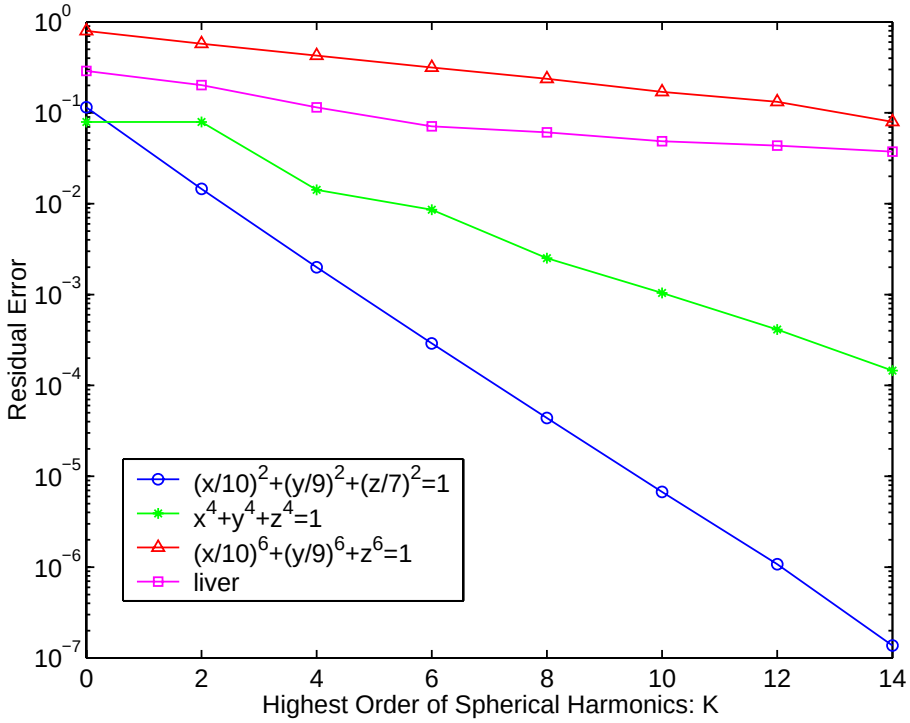

Figure 2.4: Error versus the order of the spherical harmonics for the four different surfaces shown in Figure 2.3.

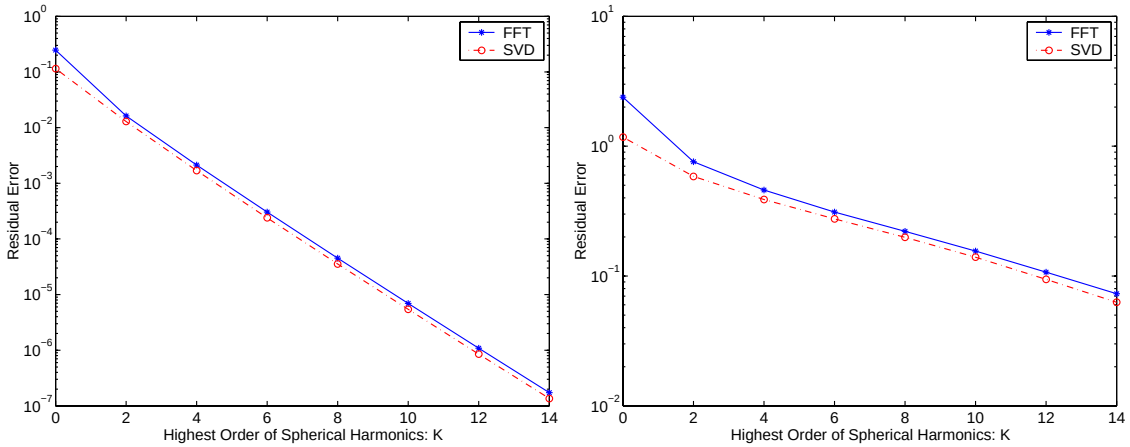

(a) $(\frac{x}{10})^2 + (\frac{y}{9})^2 + (\frac{z}{7})^2 = 1$ (b) $(\frac{x}{10})^6 + (\frac{y}{9})^6 + z^6 = 1$

Figure 2.5: Accuracy comparison between the FFT method and the SVD method.

for both the FFT method and the SVD method. (a) is the modeling result of the ellipsoidal surface, and (b) is the modeling result of the surface defined by $(\frac{x}{10})^6 + (\frac{y}{9})^6 + z^6 = 1$. It

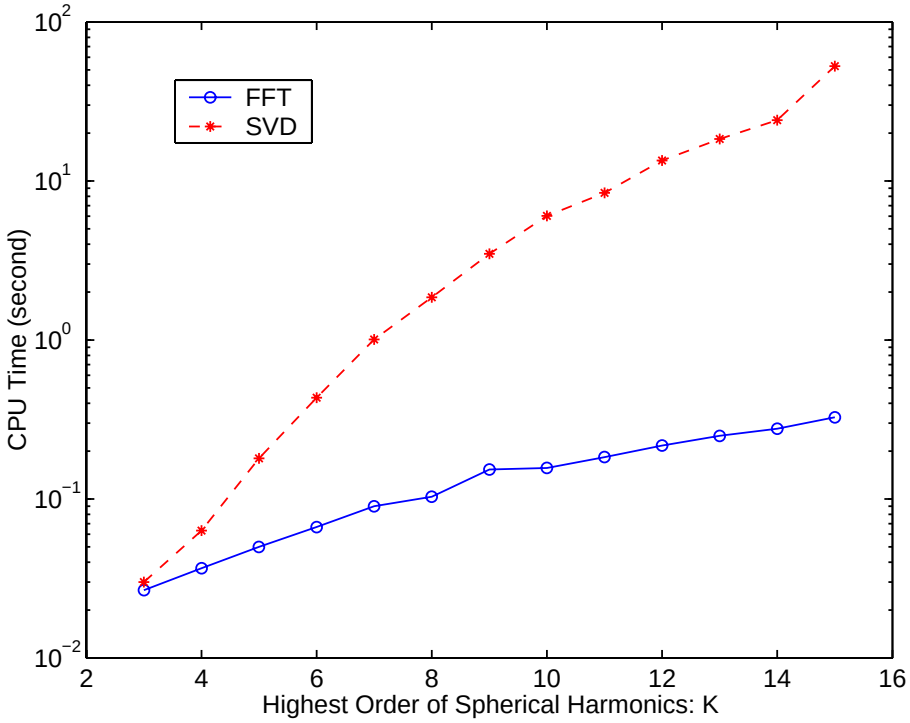

Figure 2.6: CPU time comparison for the SVD method and the FFT method.

can be seen that for the same value of K, the errors of SVD and FFT have the same order of magnitude, although the one for the SVD method is slightly smaller. This is because the FFT method requires the function to be band-limited which may not be true for an arbitrary polar surface function. When a shape contains spatial frequencies that have to be modeled by spherical harmonics higher than K, there will be aliasing phenomenon in the FFT method.

Finally, we compare the computation time of the two methods. Figure 2.6 plots the CPU time required by the SVD method and the FFT method versus K, the highest order of spherical harmonics in modeling. The slope of the circled line is very close to that of $K^2(\log K)^2$ (especially for $K > 10$), which suggests that the complexity of FFT method is $O(N(\log N)^2)$ where N is the total number of sampling points. The slope of starred line is in between of the slopes of K^5 and K^6. This means the complexity of SVD is approximately $O(N^3)$. Through the above comparison of CPU time, we can say that the

computational complexity of SVD method is much higher than that of FFT method.

The following conclusions can be drawn for shape modeling by spherical harmonic functions:

① For normal 3D polar shape objects, i.e., not as irregular as $(\frac{x}{10})^6 + (\frac{y}{9})^6 + z^6 = 1$, the highest order of spherical harmonics needed for modeling is in the range $10 \leq K \leq 20$, and the magnitude of modeling error will be in the range $(10^{-6}, 10^{-3})$.

② The SVD method and the FFT method give similar modeling accuracy if the surface sampling data sets used by two methods are same.

③ The FFT method requires the sampling points to be uniformly distributed on θ and ϕ. It has very low computational complexity.

④ The SVD method has the advantage that the sampling points can be arbitrarily distributed on the sphere. This allows to apply a higher sampling rate in surface areas of large Gaussian curvatures, and a lower sampling rate for relatively flat areas. However, its computational complexity is much higher than that of the FFT method.

2.2.3 Double Fourier Series

The simplest form of double Fourier series (DFS) arises in an expansion of scalar functions of two variables over a rectangular domain $[a, b] \times [c, d]$. The basis functions of such a DFS are separable, i.e. a product of two sets of 1-D basis functions on $[a, b]$ and $[c, d]$, respectively. When these two sets of basis functions are complex trigonometric systems, an arbitrary function $f(x, y)$ defined in this rectangle can be decomposed into a

double trigonometric series, i.e.,

$$\begin{aligned} f(x,y) &= \sum_{m=0}^{\infty}\sum_{n=0}^{\infty} a_{mn}^{cc}\cos(mx)\cos(ny) + \sum_{m=0}^{\infty}\sum_{n=0}^{\infty} a_{mn}^{cs}\cos(mx)\sin(ny) \\ &\quad \sum_{m=0}^{\infty}\sum_{n=0}^{\infty} a_{mn}^{sc}\sin(mx)\cos(ny) + \sum_{m=0}^{\infty}\sum_{n=0}^{\infty} a_{mn}^{ss}\sin(mx)\sin(ny). \end{aligned} \quad (2.16)$$

where a_{mn}^{cc}, a_{mn}^{cs}, a_{mn}^{sc} and a_{mn}^{ss} are the corresponding coefficients. Following traditional nomenclature, we use double Fourier series to denote double trigonometric series throughout this thesis. In the context of 3D shape modeling, the radial function of any 3D polar surface $R(\theta,\phi)$ is a function of two variables defined over the rectangle $[0,\pi]\times[0,2\pi)$. Therefore $R(\theta,\phi)$ can be expanded by double Fourier series. Notice that the spherical geometry of unit sphere is different from the geometry of rectangle, which imposes some conditions on the double Fourier series expansion of radial functions. We will discuss this immediately in the next section.

2.2.4 Computing Double Fourier Series

In this section, we discuss how to compute the double Fourier series of radial function $R(\theta,\phi)$ to avoid the pole problem which often accompanies computation in spherical geometry. Topologically, the unit sphere is a two-dimensional manifold. However, the

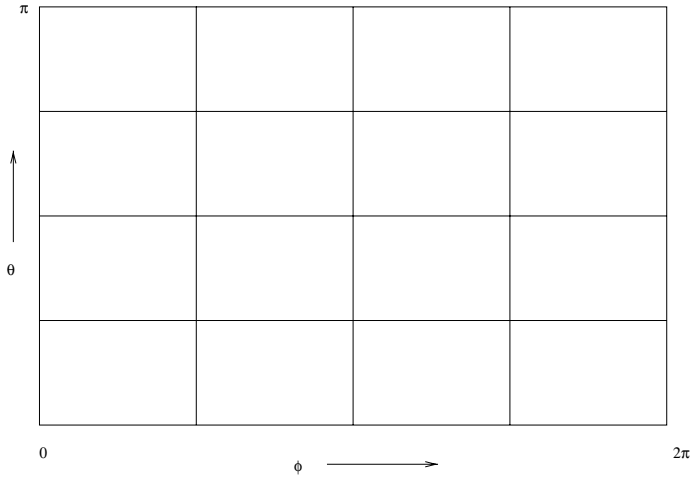

Figure 2.7: The rectangle $[0,2\pi)\times[0,\pi)$.

geometry of sphere is fundamentally different from that of the rectangle shown in Figure 2.7. For example, the surface of a torus is also defined over $[0, \pi] \times [0, 2\pi]$ and can be unwrapped into a cylinder, then into a rectangle, but the surface of sphere can not be unwrapped in such a way into a rectangle [14].

The difficulty in applying DFS to polar shapes is due to the boundary conditions imposed at the two poles $(\theta, \phi) \in \{(0, \phi), (\pi, \phi)\}$. First, the radial function $R(\theta, \phi)$ is expanded by a 1-D Fourier series in longitude with truncation M,

$$R(\theta, \phi) = \sum_{m=-M}^{M} R_m(\theta) e^{im\phi}, \tag{2.17}$$

where $R_m(\theta) = \frac{1}{K} \sum_{k=0}^{K-1} R(\theta, \phi_k) e^{-im\phi_k}$, $\phi_k = 2\pi k/K$ and $K = 2M$. Next, we expand $R_m(\theta)$ in a Fourier series that accounts for the pole boundary conditions at $\theta = 0, \pi$. These boundary conditions are [14]:

$$R_m(\theta) = \begin{cases} \text{finite}, & m = 0, \\ 0, & m \neq 0, \end{cases} \tag{2.18}$$

$$\frac{d}{d\theta} R_m(\theta) = \begin{cases} \text{finite}, & \text{odd } m, \\ 0, & \text{even } m. \end{cases} \tag{2.19}$$

The condition on $R_m(\theta)$ is to ensure that the approximated $f(\theta, \phi)$ is continuous at poles, while the condition on $\frac{d}{d\theta} R_m(\theta)$ is to avoid second-order poles in applying spectral method to solve Laplace equation over the unit sphere [83]. If we use sine or cosine series alone as basis functions to expand $R_m(\theta)$, they will not meet the above boundary conditions. For example, let $R_m(\theta) = \sum_n R_{n,m} \cos n\theta$. When m is odd, $R_m(\theta) \sin(m\phi)$ will be discontinue at the poles unless some additional constraints are imposed on $R_{n,m}$ [8, 111, 112].

In [25] Cheong proposed the following expansion

$$\begin{aligned} R_m(\theta) = &\quad \textstyle\sum_{n=0}^{J-1} R_{n,0} \cos n\theta, && m = 0, \\ R_m(\theta) = &\quad \textstyle\sum_{n=1}^{J} R_{n,m} \sin n\theta, && \text{odd } m, \\ R_m(\theta) = &\quad \textstyle\sum_{n=1}^{J} R_{n,m} \sin\theta \sin n\theta, && \text{even } m \neq 0. \end{aligned} \tag{2.20}$$

Cheong's expansion of $R_m(\theta)$ does not make explicit use of the cosine series for even m and avoids the imposition of a constraint that the sum of expansion coefficients should vanish. We adopt this expansion in our approach.

To avoid possible singularities arising from dividing by $\sin(\phi)$ on poles in the case of even $m(\neq 0)$, we use interior grids in the latitude variable, e.g., $\theta_j = (j + 0.5)\pi/J$, $j = 0, 1, 2, \ldots, J-1$. The spectral coefficients $R_{n,m}$ can be calculated by fast sine or cosine transforms on these interior grids:

$$\begin{aligned} R_{n,m} = &\quad \tfrac{b}{J} \textstyle\sum_{j=0}^{J-1} R_m(\theta_j) \cos(n\theta_j), && m = 0 \\ R_{n,m} = &\quad \tfrac{c}{J} \textstyle\sum_{j=0}^{J-1} R_m(\theta_j) \sin(n\theta_j), && \text{odd } m \\ R_{n,m} = &\quad \tfrac{c}{J} \textstyle\sum_{j=0}^{J-1} (\frac{R_m(\theta_j)}{\sin\theta_j}) \sin(n\theta_j), && \text{even } m \neq 0 \end{aligned} \tag{2.21}$$

where $b = 1$ for $n = 0$ and $b = 2$ for $n > 0$, $c = 1$ for $n = J$ and $c = 2$ for $n < J$.

2.2.5 Comparison of Spherical Harmonics and Double Fourier Series

In the last few sections, we have shown that both spherical harmonics and double Fourier series can be applied to expand radial functions of polar shape objects. In [13, 14], Boyd has made a good comparison of three orthogonal basis functions for general problems related to spherical geometry, which includes spherical harmonics, double Fourier series and Chebyshev polynomials.

Spherical harmonics and double Fourier series have some common characteristics. They both use Fourier series to represent the longitudinal dependence of the radial de-

scriptor $R(\theta, \phi)$, i.e.,

$$R(\theta, \phi) = \sum_{m=-\infty}^{\infty} R_m(\theta) e^{im\phi} \tag{2.22}$$

where m is the zonal wavenumber and must be an integer. They differ in their choices of expansion functions in latitude. Spherical harmonics use associated Legendre functions $P_l^m(\cos\theta)$, while double Fourier series use the modified Fourier series to expand $R_m(\theta)$. Both spherical harmonics and double Fourier series are complete on the unit sphere S^2.

To illustrate the accuracies of shape modeling by spherical harmonics and DFS, we apply these expansions to an ellipsoid surface and a metasphere surface. The metasphere surface is defined as $\mathbf{X} = (x(\theta, \phi), y(\theta, \phi), z(\theta, \phi))$, where

$$\begin{aligned} x(\theta, \phi) &= (a_x + b_x \cos(m_x\theta)\cos(n_x\phi))\sin(\theta)\cos(\phi), \\ y(\theta, \phi) &= (a_y + b_y \cos(m_y\theta)\cos(n_y\phi))\sin(\theta)\sin(\phi), \\ z(\theta, \phi) &= (a_z + b_z \cos(m_z\theta)\cos(n_z\phi))\cos(\theta). \end{aligned} \tag{2.23}$$

Here (a_x, a_y, a_z) is the metasphere radius in the directions of three axes, (b_x, b_y, b_z) is the ripple amplitude of harmonic components on the metasphere, (m_x, m_y, m_z) and (n_x, n_y, n_z) are the ripple frequencies [102, 107].

Figure 2.8 and Figure 2.9 show multi-resolution representations of the ellipsoid and the metasphere, separately. We can see that when spherical harmonics model and the double Fourier series model use same number of coefficients, the difference between these models is very small. A numerical comparison of modeling accuracy is plotted in Figure 2.10. For the regular ellipsoidal shape, truncated spherical harmonics and double Fourier series show exactly the same rate of convergence in their order. Note that double Fourier series has a small advantage in accuracy for the regular ellipsoid. For the metasphere, which contains higher spatial frequencies, double Fourier series also has a faster convergent rate and better accuracy. Here the SVD method was used to compute the coefficients

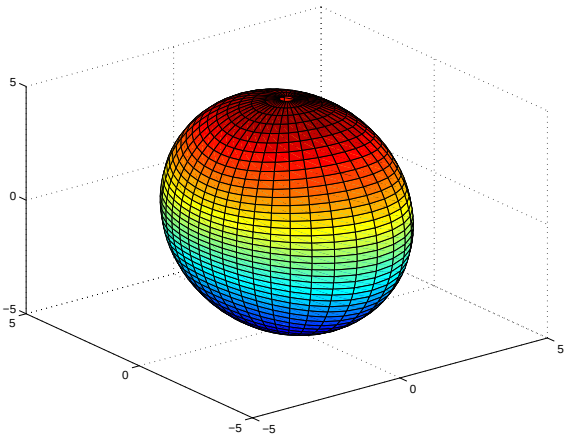

(a) Ellipsoid, $\frac{x}{3}^2 + \frac{y}{4}^2 + \frac{z}{5}^2 = 1$

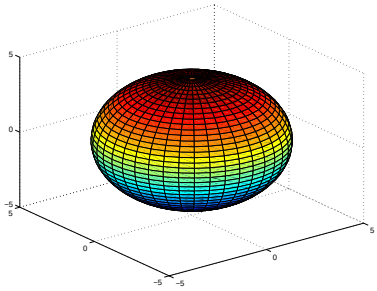

(b) DFS,$L = 0$

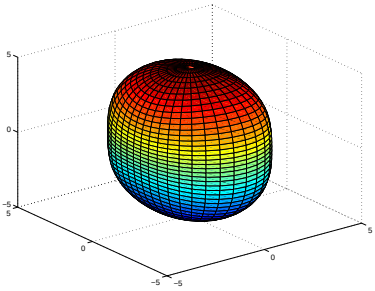

(c) DFS,$L = 2$

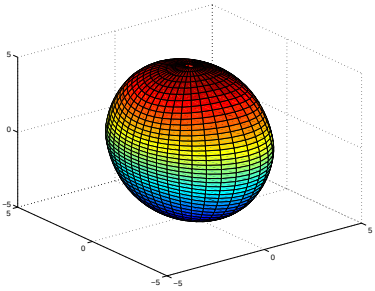

(d) DFS,$L = 4$

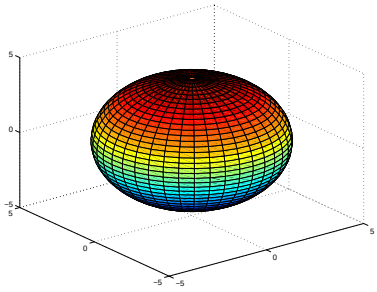

(e) SH,$L = 0$

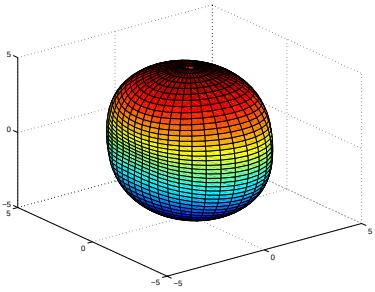

(f) SH,$L = 2$

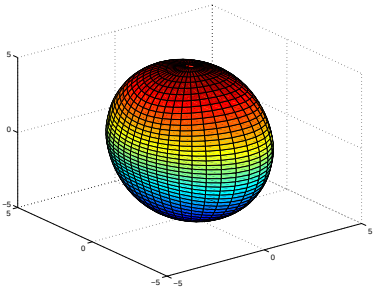

(g) SH,$L = 4$

Figure 2.8: Multi-resolution representation of an ellipsoid via the same order double Fourier series and spherical harmonics.

of spherical harmonics.

Finally, we compare the computation time of double Fourier series and spherical har-

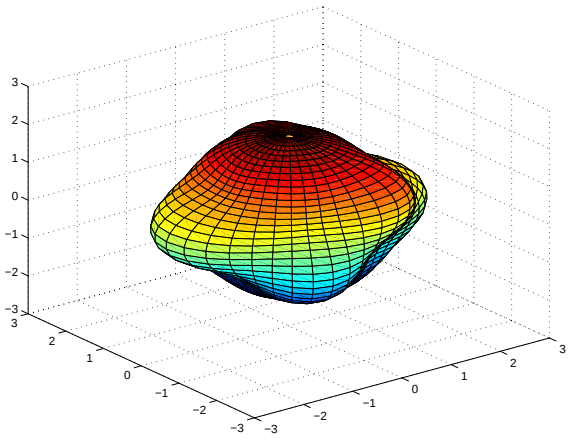

(a) Metasphere,$a_x = 2$, $a_y = 2$, $a_z = 2$;$b_x = 0.5$, $b_y = 0.5$, $b_z = 0$; $m_x = 4$, $m_y = 3$, $m_z = 2$;$n_x = 2$, $n_y = 3$, $n_z = 4$

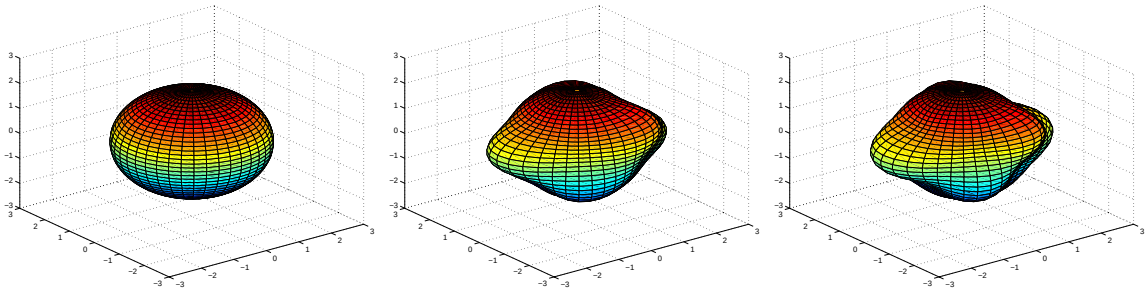

(b) DFS,$L = 0$ (c) DFS,$L = 4$ (d) DFS,$L = 8$

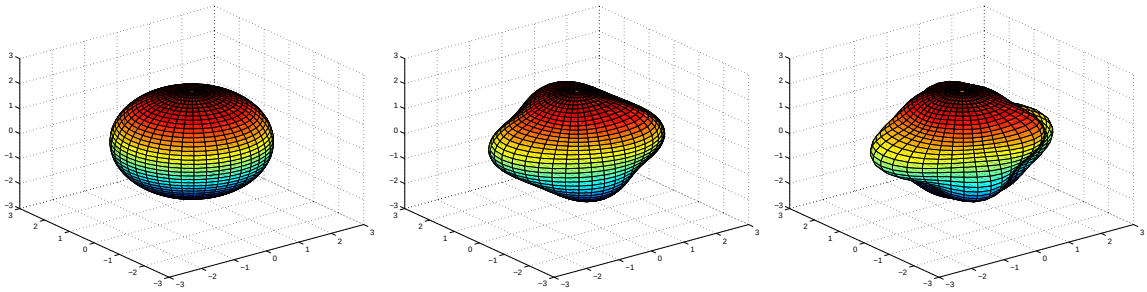

(e) SH,$L = 0$ (f) SH,$L = 4$ (g) SH,$L = 8$

Figure 2.9: Multi-resolution representation of a metasphere via the same order double Fourier series and spherical harmonics.

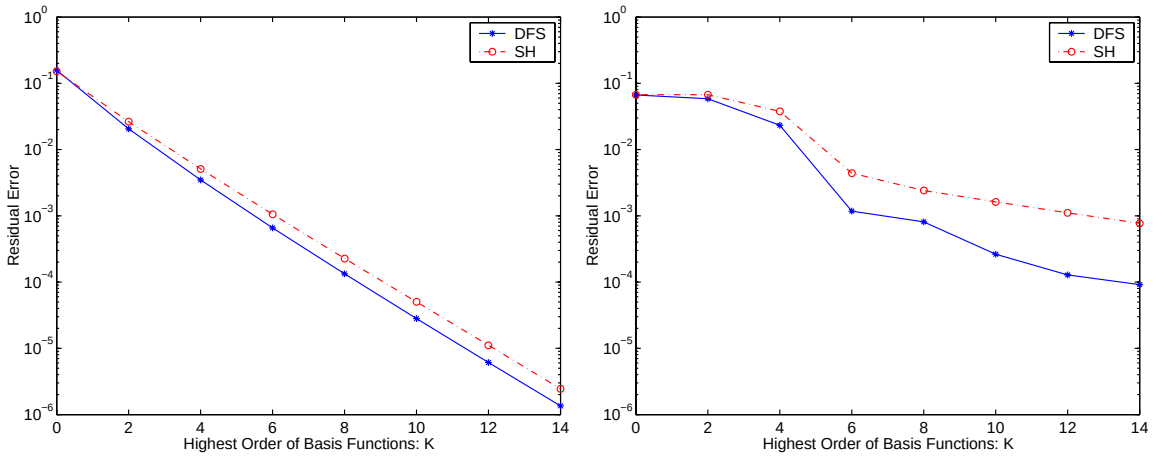

(a) Ellipsoid (b) Metasphere

Figure 2.10: Shape modeling error vs. highest order of modeling basis.

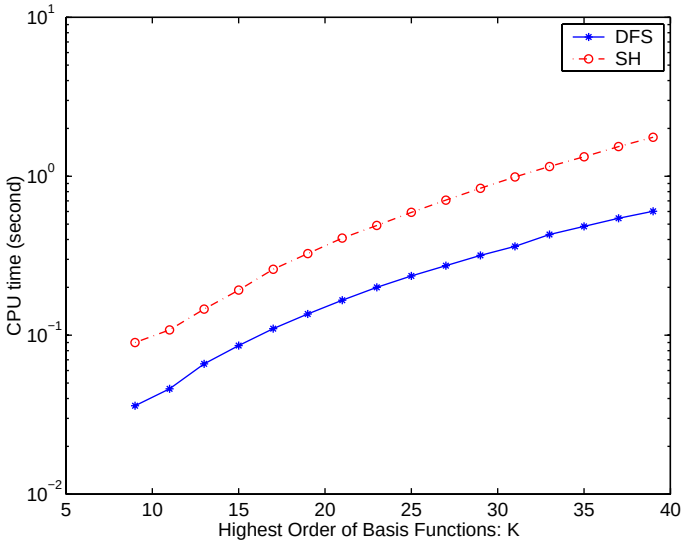

Figure 2.11: CPU time comparison for the computation of double Fourier series and spherical harmonics coefficients.

monics coefficients. Figure 2.11 plots the CPU time consumed by computing double Fourier series and spherical harmonics coefficients. It shows that when the basis functions used by these methods have the same highest order of K, the CPU time of computing spherical harmonics coefficients is about 2.5 times greater than that of by computing double Fourier series. In this experiment, the FFT algorithm was used to compute the

spherical harmonic coefficients.

2.3 Statistical Shape Modeling

We discuss random field models for statistical shape modeling in this section. The rest of this section is organized as follows: First, a few important definitions of random fields are given in Section 2.3.1. In Section 2.3.2, we show that radial functions of randomly oriented polar objects are isotropic random fields over the unit sphere and propose a procedure to test the hypothesis that a sampled data set over the unit sphere is isotropic. In Section 2.3.3, the spectral theorem that spherical harmonics comprise the orthogonal representation of isotropic random field over the unit sphere is proved. Yadrenko gave an outline of this theorem's proof in [110]. However, he did not provide the proof of Funk-Hecke theorem which is a key to proving the spectral theorem. Funk-Hecke theorem was originally proved and published in 1916 [46] and 1918 [56] by Funk and Hecke in German. The proof of Funk-Hecke theorem is not widely available. Thus for completeness, we provide a detailed proof of the spectral theorem and Funk-Hecke theorem. A brief discussion of how to corporate the random field model with statistical shape modeling will end this section. It will be shown in Chapter IV that the statistical uncorrelation of the shape parameters can be applied to optimal shape filtering and object registration.

2.3.1 Random Field on Unit Sphere

Random fields are stochastic processes whose arguments vary continuously over some subset of $\mathbb{R}^n$, n-dimensional Euclidean space. They can be strictly defined on a measure space $(\Omega, \mathcal{F}, P)$, where Ω is a set with generic element ω, $\mathcal{F}$ is a σ-algebra of subsets of Ω, and P is a probability measure on $\mathcal{F}$ satisfying the following axioms [1]:

(1) $0 \leq P(A) \leq 1$ and $P(\Omega) = 1$;

(2) $P(A \cup B) = P(A) + P(B)$, if $A \cap B = \emptyset$, $A, B \in \mathcal{F}$ and $\emptyset$ is the empty set.

The radial functions of 3-D polar objects are examples of random fields in $S^2 \subset \mathbb{R}^3$.

Definition 1 ([57]) *A second order random field over $S^2 \subset \mathbb{R}^3$ is a function $Z : S^2 \to L_2(\Omega, \mathcal{F}, P)$.*

A second order random field has been specified over S^2 if a random variable $Z(x)$ has been specified for each $x \in S^2$, with $E\{|Z(x)|^2\} < \infty$. We can say that a second order random field over S is a family $\{Z(x), x \in S^2\}$ of square integrable random variables.

A random field $Z(x)$ is *wide-sense stationary* (or wide-sense homogeneous) if it satisfies the following conditions:

(1) $E\{Z(x)\} = m$, where m is constant;

(2) $E\{(Z(s) - m)(Z(t) - m)^*\}$ is a function of $(s - t)$ only.

A wide-sense stationary random field is called *isotropic* if

$$R(||s - t||) = E\{(Z(s) - m)(Z(t) - m)^*\}.$$

The correlation function of an isotropic random field depends only on the distance between s and t. The correlation function of such a random field can be thought as invariant to any rotation around the origin. Let $SO(3)$ denote the group of rotations in $\mathbb{R}^3$ around the origin. An isotropic random field can also be defined as satisfying

$$E\{(Z(s) - m)(Z(t) - m)^*\} = E\{(gZ(s) - m)(gZ(t) - m)^*\}$$

where $g \in SO(3)$.

Let $x_1, x_2, \ldots$ be a sequence of points and x^* be a fixed point in $\mathbb{R}^3$ for which $||x_k - x^*|| \to 0$ as $k \to \infty$. Then if

$$||Z(x_k) - Z(x^*)|| \to 0 \qquad \text{as } k \to \infty$$

we say Z is *continuous in mean square* at x^*.

Theorem 2 ([1]) *A random field $Z(x)$ is continuous in mean square at the point $x^* \in \mathbb{R}^3$ iff its correlation function $R(s,t)$ is continuous at the point $s = t = x^*$.*

Theorem 3 (Mercer Theorem [114]) *Let $R(s,t)$ be a continuous and non-negative definite function on the compact interval $T \times T \subset \mathbb{R}^{2n}$, with eigenvalues λ_j and eigenfunctions ϕ_j satisfying*

$$\int_T R(s,t)\phi(t)dt = \lambda\phi(s) \qquad \text{for } s \in T \tag{2.24}$$

and

$$\int_T \phi_i(t)\phi_j(t)dt = \delta_{ij}. \tag{2.25}$$

Then

$$R(s,t) = \sum_{j=1}^{\infty} \lambda_j \phi_j(s)\phi_j^*(t) \tag{2.26}$$

where the series converges absolutely and uniformly on $T \times T$.

2.3.2 Isotropic Random Field on S^2

Let (θ_1, ϕ_1) and (θ_2, ϕ_2) denote two directions separated by the angle γ in the spherical coordinate system, as shown in Figure 2.12. These angles satisfy the following trigonometric identity [3],

$$\cos\gamma = \cos\theta_1 \cos\theta_2 + \sin\theta_1 \sin\theta_2 \cos(\phi_1 - \phi_2). \tag{2.27}$$

The value $\cos\gamma$ is called the *angular distance* between the two directions (θ_1, ϕ_1) and (θ_2, ϕ_2).

Definition 2 ([110]) *A random field $X(\theta, \phi)$ on the unit sphere S^2 is called isotropic in the wide sense if its mean is constant*

$$E\{X(\theta,\phi)\} = constant \tag{2.28}$$

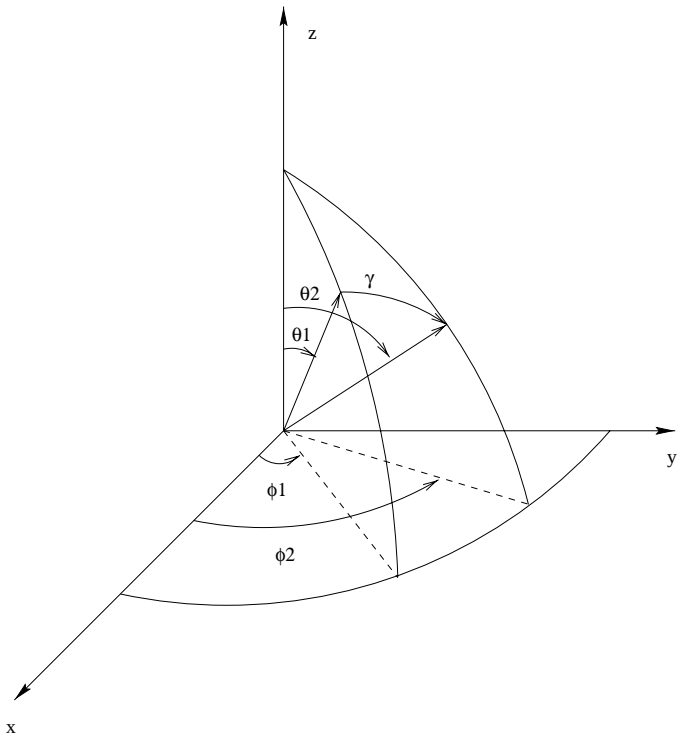

Figure 2.12: Two directions, (θ_1, ϕ_1) and (θ_2, ϕ_2), and the angle γ between them.

and its correlation depends only on the angular distance $\cos\gamma$ *between the two directions*

$$E\{X(\theta_1, \phi_1)X^*(\theta_2, \phi_2)\} \triangleq R(\gamma) = \psi(\cos\gamma) \tag{2.29}$$

where γ *is the angle between the two directions* (θ_1, ϕ_1) *and* (θ_2, ϕ_2).

Without loss of generality, hereafter we assume $E\{X(\theta, \phi)\} = 0$.

Isotropic random field models have been widely studied in many research areas, such as earth science, astrophysics and electrical field theory. In computer vision community, random field models have been applied to texture synthesis [116], texture classification [40] and image segmentation [115]. However, to the best of our knowledge, no study of statistical isotropic property has been reported for 3D shape modeling. In fact, this property is satisfied by a large class of 3D shapes. For example, in biological shape analysis, the orientation of virus particles in the electron microscope can be completely disordered [38] and the radial function segmented from such a case forms an isotropic random field.

Theorem 4 *Let $f(\theta,\phi) : S^2 \to \mathbb{R}$ be the radial function of a polar shaped object which center has been aligned with the origin O of the coordinate system. If the object center is fixed at O and the orientation of the object is uniformly distributed, i.e., there is no preferred orientation, then the observed radial function $F(\theta,\phi)$ is an isotropic random field over the unit sphere. Its mean $\bar{F}(\theta,\phi)$ and covariance function $R_F((\theta_1,\phi_1),(\theta_2,\phi_2))$ are determined by*

$$\begin{aligned} \bar{F}(\theta,\phi) &= \text{constant} \\ &= \frac{1}{4\pi}\int_{\phi'=0}^{2\pi}\int_{\theta'=0}^{\pi} f(\theta',\phi')\sin\theta' d\theta' d\phi' \end{aligned} \tag{2.30}$$

and

$$\begin{aligned} R_F((\theta_1,\phi_1),(\theta_2,\phi_2)) &= R_F(\gamma) \\ &= \frac{\int_{\phi'=0}^{2\pi}\int_{\theta'=0}^{\pi}[\int_{\mathcal{S}} f(\theta',\phi')f(\theta'',\phi'')d\mathcal{S}]\sin\theta' d\theta' d\phi'}{4\pi\cdot(2\pi\sin\gamma)}, \end{aligned} \tag{2.31}$$

where γ is the angle between (θ_1,ϕ_1) and (θ_2,ϕ_2) (see Figure 2.12), and $\mathcal{S} := \{(\theta'',\phi'') : \measuredangle[(\theta',\phi'),(\theta'',\phi'')] = \gamma\}$ is the curve containing the points that have same angular distance $\cos\gamma$ to the point (θ',ϕ') (see Figure 2.13).

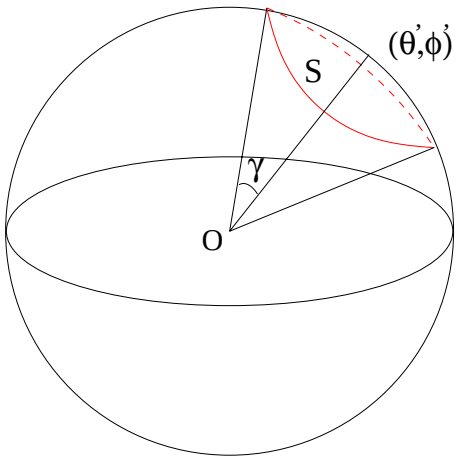

Figure 2.13: An arbitrary point (θ',ϕ') on S^2 and the curve $\mathcal{S}$ containing points that have same angular distance to (θ',ϕ')

Proof:

Let g be a random rotation operator in $SO(3)$ which has uniform distribution over $SO(3)$. The observed radial function F can be expressed as

$$F(\theta,\phi) = gf(\theta,\phi) = f(\theta',\phi'). \tag{2.32}$$

Since g is uniformly distributed in $SO(3)$, (θ',ϕ') is uniformly distributed over S^2. Therefore,

$$E[F(\theta,\phi)] = E[f(\theta',\phi')] = \frac{1}{4\pi}\int_{\phi'=0}^{2\pi}\int_{\theta'=0}^{\pi} f(\theta',\phi')\sin\theta' d\theta' d\phi' \tag{2.33}$$

This yields equation (2.30). For the correlation function R_F,

$$\begin{aligned} R_F((\theta_1,\phi_1),(\theta_2,\phi_2)) &= E[F(\theta_1,\phi_1)F(\theta_2,\phi_2)] \\ &= E[gf(\theta_1,\phi_1)gf(\theta_2,\phi_2)] \\ &= E[f(\theta',\phi')f(\theta'',\phi'')]. \end{aligned} \tag{2.34}$$

The uniform distribution of g again, makes (θ',ϕ') have a uniform distribution over S^2. Due to the rigidity of the object, (θ'',ϕ'') must be in a fixed angular distance to (θ',ϕ'). This relation causes (θ'',ϕ'') to be uniformly distributed over a curve $\mathcal{S}$ that has an angular distance $\cos\gamma$ to the point (θ',ϕ'). The length of $\mathcal{S}$ is $2\pi\sin\gamma$. Therefore equation (2.31) gives the proper correlation function of F.

End of proof.

To design an optimal test for the isotropic hypothesis, we need to compute the likelihood function of the random field under isotropic and non-isotropic assumption. Let $F(x)$ be a real-value random field over S^2 that is a combination of signal $s(x)$ and a white Gaussian noise field $n(x)$, i.e. $F(x) = s(x) + n(x)$, $x \in S^2$. The correlation function of F is defined as $R_F(x,y) = E[F(x)F(y)]$. Let $\mathbf{F} = [F_1 F_2 \cdots F_N]^T$ be the random vector obtained through sampling F at $\mathbf{x} = [x_1 x_2 \cdots x_N]^T$, $x_i \in S^2$, i.e., $F_i \triangleq F(x_i)$, the correlation function R can be estimated from the covariance matrix $\mathbf{R}_F = E[\mathbf{F}\mathbf{F}^T]$.

If we assume the random field $s(x)$ is isotropic, the correlation function of F will be in the form of $R_F(x,y) = R_F(\|x-y\|) = R_s(\|x-y\|) + \delta(x-y)\cdot\sigma_n^2$, where σ_n^2 is the variance of the noise field. We propose a sub-optimal isotropic test of how close the estimated correlation function is to the form of $R_F(\|x-y\|)$ and classify the random field into isotropic or non-isotropic categories accordingly:

1. Compute covariance matrix $\mathbf{R}_F$
2. Estimate $R_s(d)$ ($d \in [0,\pi]$), the correlation function of $s(x)$. It is determined by $\hat{R}_s = \arg\min \sum_{i,j} \|\mathbf{R}_{Fij} - R_s(\measuredangle(x_i,x_j))\|^2$.
3. Let $e = \sum_{i,j} \|\mathbf{R}_{Fij} - R_s(\measuredangle(x_i,x_j))\|^2$. If $e >$ threshold, F is non-isotropic, otherwise, F is isotropic. The threshold is determined by the variance of noise σ_n and the sampling statistics of the estimator $\hat{R}_s$.

2.3.3 Orthogonal Representation of Isotropic Random Field on S^2

Theorem 5 ([110]) *A mean-square continuous homogeneous isotropic random field $X(\theta,\phi)$ of zero mean in S^2 can be represented as:*

$$X(\theta,\phi) = \sum_{l=0}^{\infty}\sum_{m=-l}^{l} A(l,m)Y_l^m(\theta,\phi) \tag{2.35}$$

with $Y_l^m(\theta,\phi)$ denoting the spherical harmonics of degree l and order m, and

$$A(l,m) = \int_0^{2\pi}\int_0^{\pi} X(\theta,\phi)Y_l^{m*}(\theta,\phi)d\Omega_{\theta,\phi} \tag{2.36}$$

such that

$$E\{A(l,m)\} = 0 \tag{2.37}$$

and

$$E\{A(l,m)A^*(l^{'},m^{'})\} = \lambda_l\,\delta_{l,l'}\,\delta_{m,m'} \tag{2.38}$$

where

$$\lambda_l = 2\pi \int_{-1}^{1} \psi(t) P_l(t)\, dt \tag{2.39}$$

is the coefficient in the Legendre series of the correlation function, and $\psi(\cos\gamma) = R(\gamma)$ *is the correlation function of* $X(\theta, \phi)$.

Proof:

By Theorem 2 in Section 2.3.1, we know that the correlation function $R(\gamma)$ of the mean-square continuous homogeneous isotropic random field $X(\theta, \phi)$ on S^2 is continuous on $[-1, 1]$. By Funk-Hecke theorem, we have

$$\int_{S^2} \psi(\cos\gamma) Y_l^m(\theta_2, \phi_2)\, d\Omega_{\theta_2,\phi_2} = \lambda_l Y_l^m(\theta_1, \phi_1) \tag{2.40}$$

which means the set $\{\lambda_l, Y_l^m(\theta, \phi)\}$ is a complete set of eigenvalues and orthonormal eigenvectors for the correlation function $R(\gamma)$. By Mercer theorem [114], the following expansion holds for all (θ_1, ϕ_1) and (θ_2, ϕ_2):

$$\psi(\cos\gamma) = \sum_{l=0}^{\infty} \sum_{m=-l}^{l} \lambda_l\, Y_l^m(\theta_1, \phi_1) Y_l^{m*}(\theta_2, \phi_2). \tag{2.41}$$

This expansion converges absolutely and uniformly [114].

Notice

$$\begin{aligned}
& E\{X(\theta,\phi) A^*(l', m')\} \\
= \;& E\{X(\theta,\phi) \int_{S^2} X^*(\theta_2,\phi_2) Y_{l'}^{m'}(\theta_2,\phi_2) d\Omega_{\theta_2,\phi_2}\} \\
= \;& \int_{S^2} E\{X(\theta,\phi) X^*(\theta_2,\phi_2) Y_{l'}^{m'}(\theta_2,\phi_2) d\Omega_{\theta_2,\phi_2}\} \\
= \;& \int_{S^2} \psi(\cos\gamma) Y_{l'}^{m'}(\theta_2,\phi_2) d\Omega_{\theta_2,\phi_2} \\
= \;& \lambda_{l'} Y_{l'}^{m'}(\theta,\phi)
\end{aligned}$$

where the fact (2.40) is used to reach the last step. So, we have

$$\begin{aligned} E\{A(l,m)A^*(l^{'},m^{'})\} &= E\{\int_{S^2} X(\theta,\phi)Y_l^{m*}(\theta,\phi)d\Omega_{\theta,\phi}A^*(l^{'},m^{'})\} \\ &= \int_{S^2} E\{X(\theta,\phi)A^*(l^{'},m^{'})\}Y_l^{m*}(\theta,\phi)d\Omega_{\theta,\phi} \\ &= \int_{S^2} \lambda_{l'}Y_{l'}^{m^{'}}(\theta,\phi)Y_l^{m*}(\theta,\phi)d\Omega_{\theta,\phi} \\ &= \lambda_l\delta_{l,l'}\delta_{m,m'} \end{aligned}$$

which is (2.38).

Let $\hat{X}_L(\theta,\phi) = \sum_{l=0}^{L}\sum_{m=-l}^{l} A(l,m)Y_l^m(\theta,\phi)$. We need to show that

$$\lim_{L\to\infty} E\{|X(\theta,\phi) - \hat{X}_L(\theta,\phi)|^2\} = 0. \tag{2.42}$$

Note

$$\begin{aligned} & E\{|X(\theta,\phi) - \hat{X}_L(\theta,\phi)|^2\} \\ = \;& E\{X(\theta,\phi)(X^*(\theta,\phi)\} - E\{X(\theta,\phi)\hat{X}_L^*(\theta,\phi)\} \\ & -E\{\hat{X}_L(\theta,\phi)(X^*(\theta,\phi)\} + E\{\hat{X}_L(\theta,\phi)\hat{X}_L^*(\theta,\phi))\} \\ = \;& \psi(\cos\gamma)|_{\gamma=0} - \sum_{l=0}^{L}\sum_{m=-l}^{l} E\{X(\theta,\phi)A^*(l,m)\}Y_l^{m*}(\theta,\phi) - \\ & \sum_{l=0}^{L}\sum_{m=-l}^{l} E\{A(l,m)X^*(\theta,\phi)\}Y_l^m(\theta,\phi) + \\ & \sum_{l=0}^{L}\sum_{m=-l}^{l}\sum_{l'=0}^{L}\sum_{m'=-l'}^{l'} E\{A(l,m)A^*(l',m')\}Y_l^m(\theta,\phi)Y_{l'}^{m'*}(\theta,\phi) \\ = \;& \psi(\cos\gamma)|_{\gamma=0} - \sum_{l=0}^{L}\sum_{m=-l}^{l} \lambda_l\, Y_l^m(\theta,\phi)Y_l^{m*}(\theta,\phi) \end{aligned} \tag{2.43}$$

By (2.41), the limit of the above equation equals 0 when $L \to \infty$.

End of proof.

Theorem 6 (Funk-Hecke Theorem) *Let $\psi(v)$ be a continuous function on $[-1,1]$. Let $Y_l^m(\theta_2,\phi_2)$ be any surface spherical harmonic of degree l and order m. Then for any unit*

vector $(\theta_1, \phi_1) \in S^2$*, we have*

$$\int_{S^2} \psi(\cos\gamma) Y_l^m(\theta_2, \phi_2)\, d\Omega_{\theta_2,\phi_2} = \lambda_l Y_l^m(\theta_1, \phi_1) \tag{2.44}$$

where γ *is the angular distance (2.27) between* (θ_1, ϕ_1) *and* (θ_2, ϕ_2)*,* $d\Omega_{\theta_2,\phi_2} = \sin\theta_2\, d\theta_2\, d\phi_2$*, and*

$$\lambda_l = 2\pi \int_{-1}^{1} \psi(t) P_l(t) dt \tag{2.45}$$

with $P_l(x)$ *denoting the Legendre polynomial* [1] *of degree* l*.*

Proof [2]:

The Legendre polynomials are orthogonal and constitute a complete set of functions on the interval $[-1, 1]$. By the Sturm-Liouville Theory [3, 59], any function $\psi(x)$ continuous on $[-1, 1]$ can be written as its Legendre series, which converges uniformly. More precisely, we have

$$\psi(x) = \sum_{k=0}^{\infty} a_k P_k(x) \tag{2.46}$$

where $\sum_{k=0}^{\infty} a_k P_k(x)$ is *Legendre series* [3] of the function $\psi(x)$, and

$$a_k = \frac{2k+1}{2} \int_{-1}^{1} \psi(x) P_k(x) dx. \tag{2.47}$$

We also have

$$\lim_{n\to\infty} \int_{-1}^{1} \left[\psi(x) - \sum_{k=0}^{n} a_k P_k(x) \right]^2 dx = 0. \tag{2.48}$$

By the Holder's inequality, we have

$$\left| \int_{S^2} \left[\psi(\cos\gamma) - \sum_{k=0}^{n} a_k P_k(\cos\gamma) \right] Y_l^m(\theta_2, \phi_2)\, d\Omega_{\theta_2,\phi_2} \right|^2 \leq$$

$$\int_{S^2} \left[\psi(\cos\gamma) - \sum_{k=0}^{n} a_k P_k(\cos\gamma) \right]^2 d\Omega_{\theta_2,\phi_2} \int_{S^2} Y_l^m(\theta_2, \phi_2) Y_l^{m*}(\theta_2, \phi_2)\, d\Omega_{\theta_2,\phi_2}. \tag{2.49}$$

[1] The Legendre polynomial $P_l(x)$ is defined in Appendix A.2.

[2] This proof is included for completeness.

[3] In fact, the equation (2.46) holds if $\int_{-1}^{1} |\psi(x)|^2 dx < \infty$ [59].

Since

$$\int_{S^2} \left[\psi(\cos\gamma) - \sum_{k=0}^{n} a_k P_k(\cos\gamma) \right]^2 d\Omega_{\theta_2,\phi_2} = 2\pi \int_{-1}^{1} \left[\psi(x) - \sum_{k=0}^{n} a_k P_k(x) \right]^2 dx \tag{2.50}$$

and

$$\int_{S^2} Y_l^m(\theta_2,\phi_2) Y_l^{m*}(\theta_2,\phi_2)\, d\Omega_{\theta_2,\phi_2} = 1, \tag{2.51}$$

the inequality in (2.49) can be written as

$$\left| \int_{S^2} \left[\psi(\cos\gamma) - \sum_{k=0}^{n} a_k P_k(\cos\gamma) \right] Y_l^m(\theta_2,\phi_2)\, d\Omega_{\theta_2,\phi_2} \right|^2 \leq 4\pi^2 \int_{-1}^{1} \left[\psi(x) - \sum_{k=0}^{n} a_k P_k(x) \right]^2 dx. \tag{2.52}$$

Taking limit to both sides of this inequality and using (2.48), we have

$$\lim_{n\to\infty} \left| \int_{S^2} \left[\psi(\cos\gamma) - \sum_{k=0}^{n} a_k P_k(\cos\gamma) \right] Y_l^m(\theta_2,\phi_2)\, d\Omega_{\theta_2,\phi_2} \right|^2 = 0 \tag{2.53}$$

which means

$$\lim_{n\to\infty} \int_{S^2} \left[\psi(\cos\gamma) - \sum_{k=0}^{n} a_k P_k(\cos\gamma) \right] Y_l^m(\theta_2,\phi_2)\, d\Omega_{\theta_2,\phi_2} = 0. \tag{2.54}$$

i.e.,

$$\int_{S^2} \psi(\cos\gamma) Y_l^m(\theta_2,\phi_2)\, d\Omega_{\theta_2,\phi_2} = \lim_{n\to\infty} \sum_{k=0}^{n} a_k \int_{S^2} P_k(\cos\gamma) Y_l^m(\theta_2,\phi_2)\, d\Omega_{\theta_2,\phi_2}. \tag{2.55}$$

By Addition Theorem for spherical harmonics (Appendix A.1.3), $P_l(\cos\gamma)$ can be written as

$$P_l(\cos\gamma) = \frac{4\pi}{2l+1} \sum_{m=-l}^{l} Y_l^m(\theta_1,\phi_1) Y_l^{m*}(\theta_2,\phi_2). \tag{2.56}$$

Using the orthogonality of the spherical harmonics, we have

$$\int_{S^2} P_k(\cos\gamma) Y_l^m(\theta_2,\phi_2)\, d\Omega_{\theta_2,\phi_2} = \frac{4\pi}{2l+1} \delta_{k,l} Y_l^m(\theta_1,\phi_1). \tag{2.57}$$

Applying (2.57) and (2.47) to the RHS of (2.55), we have

$$\int_{S^2} \psi(\cos\gamma) Y_l^m(\theta_2, \phi_2)\, d\Omega_{\theta_2,\phi_2} = \lambda_l\, Y_l^m(\theta_1, \phi_1) \tag{2.58}$$

whereas

$$\lambda_l = 2\pi \int_{-1}^{1} \psi(x) P_l(x) dx. \tag{2.59}$$

End of proof.

2.3.4 Discussion

We have shown that an isotropic random field over the unit sphere can be orthogonally represented by spherical harmonics in the last section. It is also proved that the radial function of an arbitrary rotated 3-D object is an isotropic random field. To interweave these properties into a useful statistical shape modeling technology, we still have to deal with some details. One of them is the test of isotropism, which was discussed in Section 2.3.2. We have also simulated an arbitrarily rotated object to verify Theorem 4. The object used in the simulation is 3D star-shaped. The rotation angles are randomly generated in such a way that they have a uniform distribution in $SO(3)$. Figure 2.14 shows a triangle in different orientations in $\mathbb{R}^2$. The observed radial function is then decomposed to obtain spherical harmonics coefficients. The simulation result shows that the covariance matrix in the spatial domain can easily pass the isotropic test and the covariance matrix of the shape parameters has non-zero entries only in diagonal. When white Gaussian noise is added to the radial function in the simulation described above, more samples of the random field are needed to accurately estimate the correlation function $R(\|x, y\|)$ where x and y belong to S^2.

This simulation can be generalized to obtain a statistical model of shapes within the same class. For example, the shapes of a particular kind of virus could vary significantly with the change of time and space. After getting sufficient amount of shapes in this virus

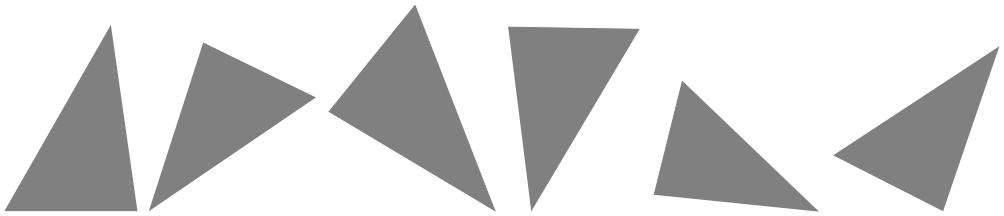

Figure 2.14: A triangle with random orientations in $\mathbb{R}^2$.

class, these shapes can be used as a training set to extract the covariance matrix of the random field shape model. If this covariance matrix passes the isotropic test, the isotropic random field model can then be regarded as a statistical shape model of this class of viruses.

Our random field model of 3D shapes is different from other statistical shape modeling technologies in the following two aspects: First, it integrates the global shape variations into a single correlation function of the isotropic random field. The isotropism is primarily caused by arbitrary rotations of the object. But other reasons, such as shape variations, are not banned. As we stated in the introduction, the published statistical shape modeling technologies usually only compute the covariance matrices of shape parameters and have contributed very little effort to generating correlation function in the spatial domain due to the complicated expression and high computational complexities; Second, in the frequency domain, the random shape parameters in our model are uncorrelated. This property is important in shape filtering. Other statistical shape models usually achieves this uncorrelation through principle component analysis. This PCA step is not necessary for our shape models.

CHAPTER III

CENTER ESTIMATION

3.1 Introduction

We depicted the statistic polar shape modeling techniques in Chapter II. These methods highly depend on the object position relative to the origin and coordinate axes. A proper choice of origin and coordinate axes is important to use shape modeling basis functions efficiently and to estimate the shape parameters accurately. For different assumptions and objectives, the optimum center for shape representation may be different. For example, Piramuthu pointed out that to maximize the average confidence in shape estimation, the optimum center may not coincide with the object centroid [87]. It was also conjectured that the optimum center may be the center for which the minimum radius of boundary is maximized [87]. However, to simplify the computation, the object centroid is a natural choice as the center for shape representation. This choice has been verified to be reliable in most practical cases [76, 92].

When an object has symmetry relative to a center, its centroid coincides with the object symmetric center. Aligning the origin with the object symmetric center is an optimum choice because the basis functions in many shape modelings are defined to be symmetric to the origin. For the shape modeling of a specific object, if the origin is not properly chosen, e.g., to be too close to the object boundary or even outside the object, the resulted

shape representation can be very inefficient, because it can not take advantage of any object symmetry and may have to contain high spatial frequencies that do not exist if the optimum center is in use. The following example illustrates how center estimation error can deteriorate the efficiency of shape modeling.

A solid sphere is contained in a three dimensional image and coarsely segmented to obtain the boundary of this sphere. We want to use spherical harmonics to model this shape. Since a sphere is the object with the most symmetry, aligning the origin with its symmetric center which is also its centroid is certainly the appropriate method. This can be verified by the property of the first degree spherical harmonics function which is a sphere of radius $\sqrt{4\pi}$. If the object center and the origin are perfectly aligned, one parameter will be sufficient to describe the entire object. However, the error in center estimation can make it very difficult to use the symmetry of the sphere. Table 3.1 and Figure 3.1 show how the efficiency and accuracy of shape representation decrease with the increasing center estimation error. The first column in Table 3.1 lists the amount of center shift, which can

Table 3.1: Shape modeling error vs. center shift for unit sphere

Center Shift	**Spherical Harmonics Degree**					
	$L=0$	$L=2$	$L=4$	$L=6$	$L=8$	$L=10$
$e=0$	0	0	0	0	0	0
$e=0.2r$	5.04e-2	9.19e-7	1.15e-9	1.81e-12	3.87e-15	2.19e-15
$e=0.4r$	1.03e-1	1.48e-5	7.57e-8	4.86e-10	3.51e-12	2.74e-14
$e=0.6r$	1.61e-1	7.75e-5	9.33e-7	1.41e-8	2.36e-10	4.23e-12
$e=0.8r$	2.26e-1	2.63e-4	6.01e-6	1.66e-7	5.05e-9	1.62e-10

be caused by inaccurate center estimation. The center shift is normalized with respect to the radius of the sphere. The parameter L is the highest order of spherical harmonics used in modeling. This table shows that when the center shift is increasing, we need more and more spherical harmonics basis functions to get an accurate shape representation of the unit sphere. When the estimated center is shifted by $0.8r$, we need to use $L = 10$

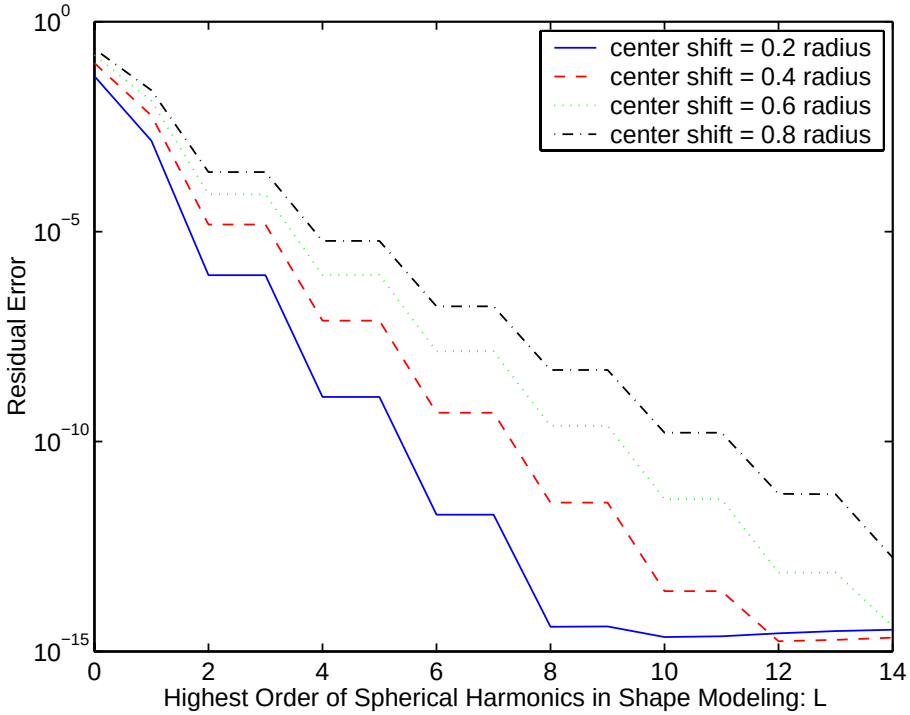

Figure 3.1: Shape modeling error vs. center shift for unit sphere

components in the spherical harmonic expansion in order to approximate a sphere with the error magnitude in the order of 10^{-10}. Furthermore, the computational complexity for $L = 10$ is much higher than that for $L = 0$, with which we can exactly represent a centered sphere.

The above example shows the importance of aligning the origin with the center of the object. However, unless the measurement system defines a natural geometry of the object, the true center of the object is not well defined. Furthermore, if the surface sample data is obtained through segmentation, the segmentation noise makes it impossible to find the true center of the object. Given a set of surface sample data, the following two methods are often used to estimate the center of the object [76]:

① Assuming that the sample data is evenly distributed over the surface of the object, the center of gravity of the sample data should provide a good estimate for the center.

② Spherical fitting. A least-square optimization method can be used to fit a sphere to the sample data (See Section 3.2 for details of the method). Then, the center of the sphere of best fit is used as the center.

In many cases of pattern recognition and image registration, it is also necessary to extract information of an object orientation. The most common method is based on principal axes [31, 73]. In [76], the following two methods are compared:

① Second Moments. The matrix of second moments of the sample is diagonalized to generate principal axes.

② Ellipsoid fitting. An ellipsoid can be fit to the scattered data. The symmetry axes of the ellipsoid are then used as principal axes.

Here the matrix of second moments has similar meaning as inertia tensor of a rigid object. Let $\{(x_i, y_i, z_i), i = 1 \cdots N\}$ be the set of surface sample data. The matrix $\mathbf{I}$ is in the form:

$$\mathbf{I} = \begin{bmatrix} I_{xx} & I_{xy} & I_{xz} \\ I_{yx} & I_{yy} & I_{yz} \\ I_{zx} & I_{zy} & I_{zz} \end{bmatrix} \tag{3.1}$$

where $I_{xx} \equiv \sum_i (y_i^2 + z_i^2)$, $I_{yy} \equiv \sum_i (x_i^2 + z_i^2)$, $I_{zz} \equiv \sum_i (y_i^2 + x_i^2)$, $I_{xy} = I_{yx} \equiv -\sum_i x_i y_i$, $I_{xz} = I_{zx} \equiv -\sum_i x_i z_i$ and $I_{yz} = I_{zy} \equiv -\sum_i y_i z_i$. After diagonalization of I, we will obtain principal moments of inertia and principal axes of the object, which are the corresponding eigenvalues and eigenvectors of $\mathbf{I}$. When a rigid body rotates around one of its principal axes, the angular momentum vector has the same direction as the angular velocity vector. It is known that the second moments method work well for evenly distributed samples, but will skew the axes if the surface is better sampled on only one side of the object. In the latter case, the ellipsoid fitting method has much better performance

[76]. However, it is also observed that some samples may yield other types of quadratic surface, instead of an ellipsoidal surface. For those rare cases, the more robust method of moments must be used.

In this study, we use the method of ellipsoid fitting because it can jointly estimate the centroid and principal axes of 3D objects. The rest of this chapter shows how this method works. A lower bound is derived for center estimation by ellipsoid fitting and compared with the simulation results.

3.2 Ellipsoid Fitting

This section studies the reconstruction of a three dimensional ellipsoid from scattered surface sample data. The ellipse and ellipsoid are often used in the fields of medical imaging and computer vision to model object shapes. In medical imaging, the coronary arteries may be represented and visualized efficiently by a generalized cylinder model with elliptical cross-sections [44, 64], and the shape or volume of anatomical organs such as heart and spine can be modeled as ellipsoids [7, 16]. In computer vision, simple patterns, such as ellipses, are important to recognize and position curved three-dimensional objects from image contours [58, 70, 106, 113].

As we discussed in the introduction, the ellipsoid fitting method is preferred when the sample data is not evenly distributed over the surface. We adopt this method because the object center and principal axes can be jointly estimated straightforwardly, so that the origin and axes of shape modeling coordinate system can be aligned with them.

The ellipsoid is a special case of quadratic surface which has a general expression as:

$$\{(x, y, z) : Ax^2 + By^2 + Cz^2 + Dxy + Exz + Fyz + Gx + Hy + Iz + J = 0\} \quad (3.2)$$

where (x, y, z) are the coordinates of the point on the ellipsoid surface, $(A, B, C, ..., J)$ are the parameters which describe the location, size and orientation of the ellipsoid. There are

nine degrees of freedom in the description of an ellipsoid, which include three coordinates of the centroid, the lengths of three symmetry axes and three orientation angles. Since the above expression has ten parameters, they must be constrained by some relations.

Several algorithms have been proposed independently by Paton [85], Albano [2], Cooper and Yalabik [29] and Gnanadesikan [48] to reconstruct quadratic curves. These algorithms fit conic sections to scattered data in the (x, y)-plane by minimizing the sum of squares of $Q(x_i, y_i) = ax_i^2 + bx_iy_i + cy_i^2 + dx_i + ey_i + f$, where $\{(x_i, y_i)\}$ are curve samples, and (a, b, c, d, e, f) are the parameters to be estimated (See Figure 3.3 for such a set of $\{(x_i, y_i)\}$). But the constraints used by these algorithms lead to solutions that are variant under equiform transformations in Euclidean space. In [11], Bookstein proposed to use the constraint of $a^2 + b^2/2 + c^2 = constant$, so that the fitting result is invariant under equiform transformations. This method also simplifies the estimation problem to the problem of solving eigenvectors of a generalized symmetric matrix. We extend Bookstein's method to 3D ellipsoid fitting and use $A^2 + B^2 + C^2 + \frac{1}{2}(D^2 + E^2 + F^2) = 1$ as constraint here.

Let $\{(x_i, y_i, z_i), i = 1 \cdots K\}$ be the set of scattered surface samples to be fitted. Define

$$Q(x_i, y_i, z_i) = Ax_i^2 + By_i^2 + Cz_i^2 + Dx_iy_i + Ex_iz_i + Fy_iz_i + Gx_i + Hy_i + Iz_i + J \quad (3.3)$$

as the error function, the ellipsoid fitting method searches for $(A, B, C, \cdots, J)$ that can minimize $\sum_i [Q(x_i, y_i, z_i)]^2$ with the constraint $A^2 + B^2 + C^2 + \frac{1}{2}(D^2 + E^2 + F^2) = 1$. Let $V = (A, B, C, D, E, F, G, H, I, J)$ be the parameter vector to be estimated and $L_i = (x_i^2, y_i^2, z_i^2, x_iy_i, x_iz_i, y_iz_i, x_i, y_i, z_i, 1)$. Define the matrix $S = \sum_i L_i^T L_i$, we have

$$\sum_i [Q(x_i, y_i, z_i)]^2 = VSV^T. \quad (3.4)$$

Let $V_1 = (A, B, C, D, E, F)$, $V_2 = (G, H, I, J)$, $L_{i1} = (x_i^2, y_i^2, z_i^2, x_iy_i, x_iz_i, y_iz_i)$ and

$L_{i2} = (x_i, y_i, z_i, 1)$. The matrix S can be written as

$$S = \begin{bmatrix} S_{11} & S_{12} \\ S_{21} & S_{22} \end{bmatrix} \tag{3.5}$$

where $S_{11} = \sum_i L_{i1}^T L_{i1}$, $S_{12} = \sum_i L_{i1}^T L_{i2}$, $S_{21} = \sum_i L_{i2}^T L_{i1}$, and $S_{22} = \sum_i L_{i2}^T L_{i2}$. Substitution of (3.5) into (3.4) yields

$$VSV^T = (V_{1,} V_2) \begin{bmatrix} S_{11} & S_{12} \\ S_{21} & S_{22} \end{bmatrix} \begin{bmatrix} V_1^T \\ V_2^T \end{bmatrix} = V_1 S_{11} V_1^T + 2V_1 S_{12} V_2^T + V_2 S_{22} V_2^T.$$

To minimize VSV^T, we let the derivative $\frac{d(VSV^T)}{d(V_2)}$ to be zero, i.e.,

$$\frac{d(VSV^T)}{d(V_2)} = 2V_1 S_{12} + 2V_2 S_{22} = 0.$$

This leads to

$$V_2 = -V_1 S_{12} S_{22}^{-1}. \tag{3.6}$$

Substituting $V_2 = -V_1 S_{12} S_{22}^{-1}$ into VSV^T, we have

$$VSV^T = V_1 (S_{11} - S_{12} S_{22}^{-1} S_{21}) V_1^T = V_1 (\widetilde{S}) V_1^T \tag{3.7}$$

where $\widetilde{S} = S_{11} - S_{12} S_{22}^{-1} S_{21}$.

Let us define $D_1 = diag(1, 1, 1, \frac{1}{2}, \frac{1}{2}, \frac{1}{2})$, the constraint $A^2 + B^2 + C^2 + \frac{1}{2}(D^2 + E^2 + F^2) = 0$ can be described in the form $V_1 D_1 V_1^T = 1$. Therefore, the constrained minimization of VSV' has been converted to minimization of $V_1 \widetilde{S} V_1^T - \lambda V_1 D_1 V_1^T$. Taking the derivative over V_1 and setting it to zero, we obtain

$$2\widetilde{S} V_1^T - 2\lambda D_1 V_1^T = 0. \tag{3.8}$$

This indicates that the vector V_1^T should be the eigenvector of $\widetilde{S}$. In the implementation, the eigenvector of best geometric fit is chosen to be the final solution of parameter estimation. The center and principal axes of an ellipsoid are completely determined by the parameter vector V.

3.3 Lower Bound for Center Estimation by Ellipsoid Fitting

To evaluate the performance of ellipsoid fitting, we develop a lower bound for the variance of unbiased center estimators under a Gaussian segmentation noise model. It is also shown that when the segmentation noise level is low and has a Gaussian distribution, the ellipsoid fitting method studied in section 3.2 is a maximum likelihood estimator of the ellipsoid parameter vector, and its performance can approach the developed lower bound. Our derivation of the lower bound follows similar steps as the derivation of a Cramér-Rao bound.

The effectiveness of an unbiased estimator can be characterized by its variance. Cramér-Rao bound, the inverse of Fisher information matrix, describes the minimum obtainable mean square error associated with a given estimate of a set of parameters. Let $\mathbf{z}$ represent observed data and $\theta = [\theta_1, \theta_2, \cdots, \theta_n]^T$ be the parameter vector to be estimated from $\mathbf{z}$. The Fisher information matrix $\mathbf{J}$ is defined as [91]:

$$\begin{aligned} J_{ij} &= E\left\{\frac{\partial \ln p(\mathbf{z}|\theta)}{\partial \theta_i}\frac{\partial \ln p(\mathbf{z}|\theta)}{\partial \theta_j}\right\} \\ &= -E\left\{\frac{\partial^2 \ln p(\mathbf{z}|\theta)}{\partial \theta_i \partial \theta_j}\right\} \end{aligned} \tag{3.9}$$

where J_{ij} is (i,j)-entry of the $n \times n$ matrix $\mathbf{J}$. Let $\mathbf{\Psi} = \mathbf{J}^{-1}$. The Cramér-Rao bound on the covariance of the estimation error is given by

$$E\left[\hat{\theta}_i(\mathbf{z})\hat{\theta}_j(\mathbf{z})\right] \geq \Psi_{ij} \tag{3.10}$$

where $\hat{\theta}_i(\mathbf{z})$ and $\hat{\theta}_j(\mathbf{z})$ are the unbiased estimators of θ_i and θ_j, and Ψ_{ij} is (i,j)-entry of $\mathbf{\Psi}$. The derivation of such a bound for the ellipsoid parameter vector V is described as follows.

First, let us set up the segmentation noise model. Write equation (3.2) in the spherical

coordinate system as:

$$\begin{aligned} & Ar^2(\sin\theta\cos\phi)^2 + Br^2(\sin\theta\sin\phi)^2 + Cr^2(\cos\theta)^2 \\ +\frac{1}{2}[& Dr^2(\sin^2\theta\sin 2\phi) + Er^2(\sin 2\theta\cos\phi) + Fr^2(\sin 2\theta\sin\phi)] \\ & +Gr\sin\theta\cos\phi + Hr\sin\theta\sin\phi + Ir\cos\theta + J = 0, \end{aligned} \tag{3.11}$$

where (r, θ, ϕ) are spherical coordinates of point (x, y, z) on the surface. To arrange equation (3.11) into a quadratic form of r, we define

$$\begin{aligned} A_1 &= A(\sin\theta\cos\phi)^2 + B(\sin\theta\sin\phi)^2 + C(\cos\theta)^2 + \\ &\quad \frac{1}{2}[D(\sin^2\theta\sin 2\phi) + E(\sin 2\theta\cos\phi) + F(\sin 2\theta\sin\phi)] \\ B_1 &= G\sin\theta\cos\phi + H\sin\theta\sin\phi + I\cos\theta \\ C_1 &= J. \end{aligned} \tag{3.12}$$

Substitute (3.12) into (3.11), we have

$$A_1 r^2 + B_1 r + C_1 = 0 \tag{3.13}$$

If we assume the origin of the spherical coordinate system is inside the ellipsoid, the true radial value in each direction (θ, ϕ) is:

$$r_0(\theta, \phi) = \frac{\sqrt{B_1^2 - 4A_1C_1} - B_1}{2A_1}. \tag{3.14}$$

In ellipsoid fitting, $\sum_i Q^2(x_i, y_i, z_i)$ is minimized to estimate the parameter vector. It is proved in [11] that $Q(x_i, y_i, z_i) = Q(r_i, \theta_i, \phi_i) \propto (\frac{r_i}{r_0(\theta_i,\phi_i)})^2 - 1$, where r_0 is determined by (3.14). Therefore the ellipsoid fitting method implements a maximum likelihood estimation of the parameter vector, when it is assumed that the noise in each direction (θ_i, ϕ_i) is uncorrelated and the segmentation data follows the probability density function

$$f(r_i) = \alpha_i \cdot \exp[-\frac{(\frac{r_i^2}{r_{0,i}^2(\theta_i,\phi_i)} - 1)^2}{\sigma^2}], \qquad r_i > 0 \tag{3.15}$$

where $r_{0,i}$ is the true radius in the sample direction (θ_i, ϕ_i) determined by (3.14) and α_i is the normalization factor. If $r_i - r_{0,i} \ll r_{0,i}$, we have $(\frac{r_i^2}{r_{0,i}^2} - 1)^2 \approx 4(\frac{r_i - r_{0,i}}{r_{0,i}})^2$, and $f(r_i)$ can be approximated by

$$f_1(r_i) = \alpha_i \cdot \exp[-4(\frac{r_i - r_{0,i}}{\sigma r_{0,i}})^2], \qquad r_i > 0 \tag{3.16}$$

Notice that $f_1(r_i)$ is not a probability density function with respect to $r \in (\infty, \infty)$. To force $f_1(r_i)$ to become a probability density function, the normalization factor α_i has to modified as

$$\alpha_{1,i} = 1/\int_{-\infty}^{\infty} \exp[-4(\frac{x}{\sigma r_{0,i}})^2]dx = \frac{2}{r_{0,i}\sigma\sqrt{\pi}}.$$

This approximation is illustrated in Figure 3.2.

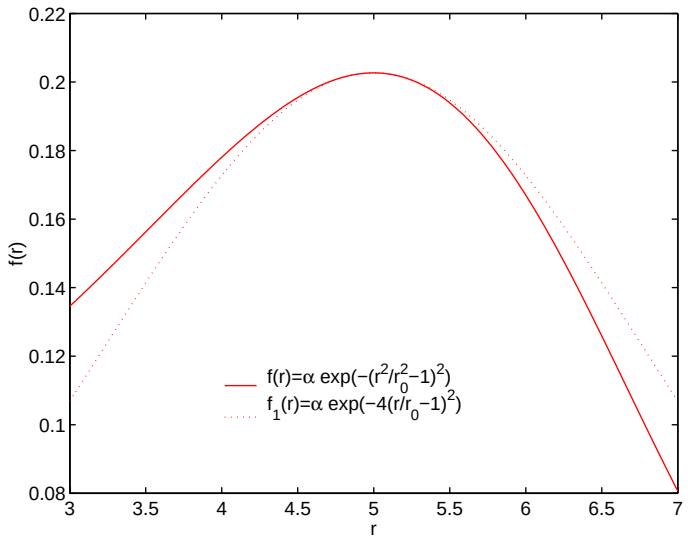

Figure 3.2: Approximation of $f(r)$ by $f_1(r)$ under the condition $r - r_0 \ll r_0$. Here $r_0 = 5$ and $\sigma = 1$.

During the derivation of lower bound and the simulation of the ellipsoid fitting performance, we adopt $f_1(r)$ as the probability density function of segmentation data. This is equivalent to a Gaussian noise model. In the following, we derive the Fisher information for parameter A with the above noise model.

Taking the logarithm in both side of (3.16), we have

$$\ln f_1(r) = -4(\frac{r-r_0}{\sigma r_0})^2 + \ln \alpha_1 = -4(\frac{r-r_0}{\sigma r_0})^2 - \ln r_0 - \ln(\sigma\sqrt{\pi}/2). \tag{3.17}$$

The partial derivative of $\ln f_1(r)$ with respect to A is

$$\frac{\partial \ln f_1(r)}{\partial A} = \frac{\partial \ln f_1(r)}{\partial r_0} \cdot \frac{\partial r_0}{\partial A_1} \cdot \frac{\partial A_1}{\partial A}. \tag{3.18}$$

where

$$\frac{\partial \ln f_1(r)}{\partial r_0} = 8\frac{r(r-r_0)}{\sigma^2 r_0^3} - \frac{1}{r_0}, \tag{3.19}$$

$$\frac{\partial r_0}{\partial A_1} = -(\frac{C_1}{A_1\sqrt{B_1^2 - 4A_1C_1}} + \frac{\sqrt{B_1^2 - 4A_1C_1} - B_1}{2A_1^2}), \tag{3.20}$$

$$\frac{\partial A_1}{\partial A} = (\sin\theta\cos\phi)^2. \tag{3.21}$$

The second order partial derivative of $\ln f_1(r)$ to A is

$$\begin{aligned} \frac{\partial^2 \ln f_1(r)}{\partial A^2} &= \frac{\partial A_1}{\partial A} \cdot [\frac{\partial \ln f_1(r)}{\partial r_0} \cdot \frac{\partial^2 r_0}{\partial A_1^2} \cdot \frac{\partial A_1}{\partial A} + \frac{\partial r_0}{\partial A_1} \cdot \frac{\partial^2 \ln f_1(r)}{\partial r_0^2} \cdot \frac{\partial r_0}{\partial A_1} \cdot \frac{\partial A_1}{\partial A}] \\ &= (\frac{\partial A_1}{\partial A})^2 \cdot [(\frac{\partial \ln f_1(r)}{\partial r_0}) \cdot (\frac{\partial^2 r_0}{\partial A_1^2}) + (\frac{\partial r_0}{\partial A_1})^2 \cdot \frac{\partial^2 \ln f_1(r)}{\partial r_0^2}] \end{aligned} \tag{3.22}$$

where

$$\frac{\partial^2 \ln f_1(r)}{\partial r_0^2} = -24\frac{r^2}{\sigma^2 r_0^4} + 16\frac{r}{\sigma^2 r_0^3} + \frac{1}{r_0^2}. \tag{3.23}$$

The mean of $\frac{\partial^2 \ln f_1(r)}{\partial A^2}$ is:

$$E[\frac{\partial^2 \ln f_1(r)}{\partial A^2}] = -(\frac{8}{\sigma^2 r_0^2} + \frac{2}{r_0^2})(\frac{\partial r_0}{\partial A_1})^2 \cdot (\frac{\partial A_1}{\partial A})^2. \tag{3.24}$$

Let the total number of points in the segmentation data set be denoted as K. With the assumption that noise are independent over different direction (θ_i, ϕ_i), the joint probability density function for the set of sample data is $\prod_{i=1}^{K} f_1(r_i)$, where $f_1(r_i)$ is the probability density function of the segmentation data in direction (θ_i, ϕ_i). Therefore, the Fisher information for the parameter A is:

$$I_A = \sum_{i=1}^{K} -E[\frac{\partial^2 \ln f_{1,i}(r_i)}{\partial A^2}]. \tag{3.25}$$

Similarly, we can compute the other entries in the Fisher information matrix of the ellipsoid parameter vector V. The computation was completed through symbolic computation in MAPLE.

For an arbitrary quadratic surface like (3.2), its center can equivalently be defined as the crossing point of the following three surfaces [98]:

$$\begin{aligned} 2Ax + Dy + Ez + G &= 0, \\ Dx + 2By + Fz + H &= 0, \\ Ex + Fy + 2Cz + I &= 0. \end{aligned} \tag{3.26}$$

Once we have estimated the parameter vector $V = (A, B, C, D, E, F, G, H, I)$ through ellipsoid fitting, the coordinates of the center $(\hat{x}, \hat{y}, \hat{z})$ can be determined by:

$$\begin{pmatrix} \hat{x} \\ \hat{y} \\ \hat{z} \end{pmatrix} = - \begin{pmatrix} 2\hat{A} & \hat{D} & \hat{E} \\ \hat{D} & 2\hat{B} & \hat{F} \\ \hat{E} & \hat{F} & 2\hat{C} \end{pmatrix}^{-1} \begin{pmatrix} \hat{G} \\ \hat{H} \\ \hat{I} \end{pmatrix} \tag{3.27}$$

where $(\hat{A}, \hat{B}, \hat{C}, \hat{D}, \hat{E}, \hat{F}, \hat{G}, \hat{H}, \hat{I})$ is the estimate of V. Based on the inverse of the Fisher information matrix of V, we can obtain a lower bound on the covariance of $(\hat{x}, \hat{y}, \hat{z})$. Define $\hat{\mathbf{x}} = (\hat{x}, \hat{y}, \hat{z})^T$, $\hat{\mathbf{K}} = \begin{pmatrix} 2\hat{A} & \hat{D} & \hat{E} \\ \hat{D} & 2\hat{B} & \hat{F} \\ \hat{E} & \hat{F} & 2\hat{C} \end{pmatrix}^{-1}$ and $\hat{\mathbf{b}} = (\hat{G}, \hat{H}, \hat{I})^T$. We rewrite equation (3.27) in the form of $\hat{\mathbf{x}} = -\hat{\mathbf{K}}\hat{\mathbf{b}} = -(\bar{\mathbf{K}} + \mathbf{K}_e)(\bar{\mathbf{b}} + \mathbf{b}_e)$, where $\bar{\mathbf{K}}$ and $\bar{\mathbf{b}}$ are the mean values of $\hat{\mathbf{K}}$ and $\hat{\mathbf{b}}$, and $\mathbf{K}_e$ and $\mathbf{b}_e$ represent errors in $\hat{\mathbf{K}}$ and $\hat{\mathbf{b}}$. The lower bound for

the covariance of the center estimator can be obtained from following computation:

$$\begin{aligned}
\text{cov}(\hat{\mathbf{x}}) &= E\left[(\hat{\mathbf{x}}-\bar{\mathbf{x}})(\hat{\mathbf{x}}-\bar{\mathbf{x}})^T\right] \\
&= E\left[(\hat{\mathbf{K}}\hat{\mathbf{b}}-\bar{\mathbf{K}}\bar{\mathbf{b}})(\hat{\mathbf{K}}\hat{\mathbf{b}}-\bar{\mathbf{K}}\bar{\mathbf{b}})^T\right] \\
&= \text{cov}(\bar{\mathbf{K}}\mathbf{b}_e)+\text{cov}(\mathbf{K}_e\bar{\mathbf{b}})+\text{cov}(\mathbf{K}_e\mathbf{b}_e) \\
&> \text{cov}(\bar{\mathbf{K}}\mathbf{b}_e)+\text{cov}(\mathbf{K}_e\bar{\mathbf{b}}) \\
&\geq \bar{\mathbf{K}}\mathbf{F}^{-1}(\mathbf{b})\bar{\mathbf{K}}^T+\text{cov}(\mathbf{K}_e\bar{\mathbf{b}}) \qquad (3.28)
\end{aligned}$$

where $\mathbf{F}^{-1}(\mathbf{b})$ denotes the inverse of Fisher information matrix of the parameter vector (G,H,I). In the above derivation, we have assumed that $\text{cov}(\mathbf{K}_e\mathbf{b}_e)$ is much smaller than $\text{cov}(\bar{\mathbf{K}}\mathbf{b}_e)$ and $\text{cov}(\mathbf{K}_e\bar{\mathbf{b}})$. $\bar{\mathbf{K}}\mathbf{F}^{-1}(\mathbf{b})\bar{\mathbf{K}}^T$ is an approximation of $\text{cov}(\bar{\mathbf{K}}\mathbf{b}_e)$. The accuracy of this approximation improves as $\text{var}(\hat{\mathbf{K}}_{ij})\rightarrow 0$. To further simplify the computation of lower bound, we let $\bar{\mathbf{b}}$ equal zero in our experiment so that the term $\text{cov}(\mathbf{K}_e\bar{\mathbf{b}})$ in (3.28) can be ignored.

3.4 Simulation Results

To evaluate the performance of center estimation by the proposed ellipsoid fitting method, we have simulated noisy segmentation data sets and applied ellipsoid fitting method to estimate the object center. In the simulation, segmentation data in each sample direction (θ_i,ϕ_i) was generated independently with Gaussian distribution $f_1(r_i)=\alpha_i\cdot\exp[-4(\frac{r_i-r_{0,i}}{\sigma r_{0,i}})^2]$, where $r_{0,i}$ is the true radial value. Sampling direction (θ,ϕ) is evenly distributed over a grid on $[0,\pi]\times[0,2\pi)$. The true surface used in the simulation is an ellipsoid $\frac{x^2}{7^2}+\frac{y^2}{6^2}+\frac{z^2}{5^2}=1$. One such simulated segmentation in a 2D cross section of the ellipsoid is shown in Figure 3.3. We think that these simulated errors are representative of errors incurred by coarse hand segmentation or automatic segmentation of a noisy boundary. It is shown in Appendix B that the segmentation error can be modeled by a

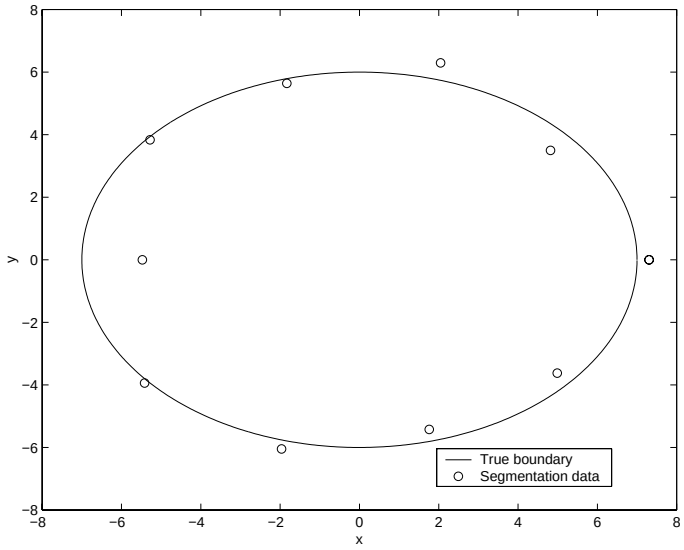

Figure 3.3: Segmentation data on a cross section of the ellipsoid, $\sigma = 0.2$.

Gaussian random variable in 1D edge detection. If we regard the 3D surface segmentation as implemented through 1D edge detection along each sampling direction and assume that surface curvature has no significant influence over the detection, our noise model will simulate the segmentation error very well. However, if the sampling density is relatively high as compared to the object size, the segmentation noise in neighborhood will be correlated [72].

For each noise level, 200 sets of simulated segmentation data were generated. Figure 3.4(a) shows the bias of the center coordinate estimator $\hat{x}$. Figure 3.4(b) compares the variance of $\hat{x}$ with the developed lower bound. When the noise level is low, the variance of $\hat{x}$ is very close to the lower bound. This proves that this center estimator is an efficient maximum likelihood estimator when the noise level is low. We have also simulated the segmentation data with σ larger than 0.5 with the same ellipsoid used above. The results show that the performances of the ellipsoid fitting center estimator is not stable because of the outliers in the segmentation data.

3.5 Conclusion

We established that the estimator of the ellipsoid parameter vector proposed by Bookstein is a maximum likelihood estimator when the segmentation noise level is low. A lower bound has been derived for the variance of center estimator with Gaussian noise model of the segmentation data. The simulated results show that the center estimator by ellipsoid fitting method is efficient when the noise level is low.

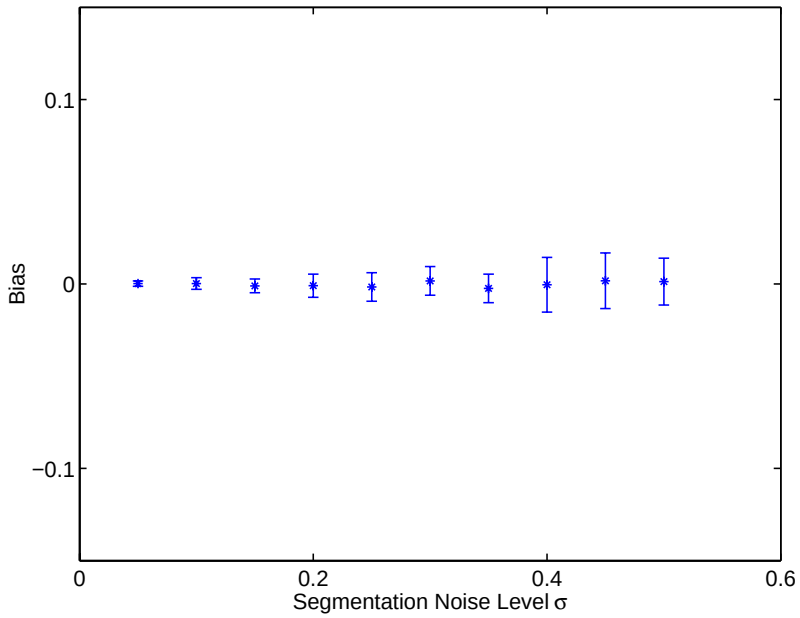

(a) Bias of $\hat{x}$

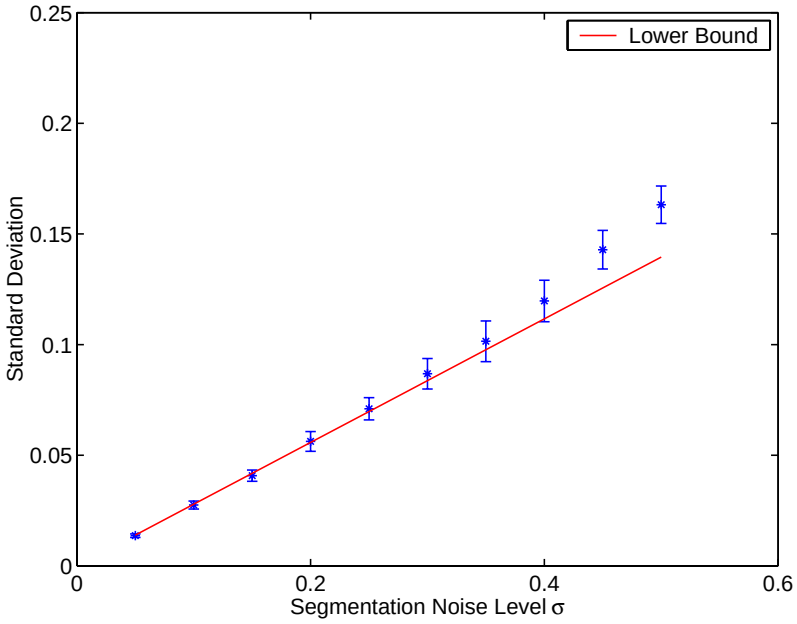

(b) Standard deviation of $\hat{x}$

Figure 3.4: Performance of the ellipsoid fitting center estimator

CHAPTER IV

APPLICATIONS OF STATISTICAL POLAR SHAPE MODELING

The statistical polar shape models have been introduced in Chapter II. We will look at two applications of statistical shape modeling in this chapter. The first application of Wiener filtering intends to show how the orthogonal representation of a random field can be applied to optimal shape filtering and estimation. The second application to 3D object registration demonstrates that linear transform method is still a very effective tool in pattern recognition. In particular, the independence of the random shape parameters can efficiently reduce the computational complexity of optimization procedure.

4.1 Wiener Filtering on Unit Sphere

Shape extraction is a noisy process that introduces boundary approximation errors. If we can model the extracted shape as an isotropic random field over S^2, as discussed in Section 2.3, Wiener filtering can yield an optimal shape estimator in terms of the least mean square error.

4.1.1 Wiener filtering by spherical harmonics

It has been shown that spherical harmonics are eigenfunctions in the Karhunen-Loéve expansion of an isotropic random field over the unit sphere S^2. It is well known that

Wiener filtering can be implemented in the original or K-L expansion domains. Based on the spectral theory of isotropic random field and the spherical geometry of polar objects, one can also in principle use this theory to decompose the radial function and estimate independent noisy shape parameters. The detailed procedure is described in the text following.

Let $F(x) : S^2 \rightarrow (0, +\infty)$ represent the radial function of a polar object acquired through some segmentation process. It is assumed that $\bar{F} = E[F]$ and that the zero mean random field $F - \bar{F}$ can be decomposed as:

$$F(x) - \bar{F}(x) = S(x) + W(x) \tag{4.1}$$

where S is an isotropic zero mean Gaussian random field and W represents a white Gaussian noise field. The correlation function of S can be represented by $R_S(x, y) = \psi_S(cos(\measuredangle(x, y)))$. Strictly speaking, for consistency S and W must be such that $S + W \geq -\bar{F}$ w.p.1. We will sidestep this issue by assuming that the standard deviations of S and W are much smaller than $\bar{F}$. By spectral theory of isotropic random field, the K-L expansion of S is a linear combination of spherical harmonics,

$$S(x) = \sum_{l=0}^{\infty} \sum_{m=-l}^{l} a_l^m Y_l^m(x) \tag{4.2}$$

where a_l^m is independent random variable (for all l, m) with zero mean and variance

$$E[a_l^m a_{l'}^{m'}] = \lambda_l \delta_{l,l'} \delta_{m,m'}. \tag{4.3}$$

Here λ_l is determined by $\lambda_l = 2\pi \int_{-1}^{1} \psi_S(x) P_l(x) dx$. Let σ_W^2 be the variance of the white Gaussian noise and $F_l^m = \int_{S^2} (F - \bar{F}) Y_l^m(x) d\Omega_{S^2}$ be the spherical harmonic coefficients of $F - \bar{F}$. By Wiener filtering theory, the optimal estimator of the parameter a_l^m is the conditional mean $E[a_l^m | F_l^m]$ which can be written as:

$$\hat{a}_l^m = \frac{\int_{S^2} (F - \bar{F}) Y_l^m(x) d\Omega_{S^2} \cdot \lambda_l}{\lambda_l + \sigma_W^2}. \tag{4.4}$$

The optimal estimation of S is a linear combination of spherical harmonics weighted by $\hat{a}_l^m$:

$$\hat{S}(x) = \sum_{l=0}^{\infty} \sum_{m=-l}^{l} \hat{a}_l^m Y_l^m(x) \tag{4.5}$$

For the theory of Wiener filtering, readers are referred to [94] for details.

4.1.2 Double Fourier Series Approximation

To reduce the computational complexity of spherical harmonics, double Fourier series can be introduced in place of spherical harmonics in the estimation procedure.

The Legendre polynomial $P_l(\cos\theta)$ can be written as

$$P_l(\cos\theta) = \sum_{k=0}^{l} (-1)^n \binom{-\frac{1}{2}}{k} \binom{-\frac{1}{2}}{l-k} \cos(l-2k)\theta. \tag{4.6}$$

And the associated Legendre function $P_l^m(x)$ has the following relationship with $P_l(x)$

$$P_l^m(x) = (-1)^m (1-x^2)^{m/2} \frac{d^m}{dx^m} P_l(x) \tag{4.7}$$

Therefore the spherical harmonics function $Y_l^m(\theta,\phi) = c_l^m P_l^m(\cos\theta) e^{im\phi}$ has an inherent relationship with double Fourier series and can be rewritten as a linear combination of double Fourier series. We relate double Fourier series to spherical harmonics by representing a finite number of discretized spherical harmonics and double Fourier series basis elements in two matrices Φ and Ψ, respectively. Let $\mathbf{K}$ represent the constant matrix which maps the DFS basis Ψ onto the SH basis Φ: $\Phi = \mathbf{K}\Psi$. The rank of $\mathbf{K}$ only depends on the highest order of SH used in the application. It can be shown that $\mathbf{K}$ is a very sparse matrix and therefore has a fast inverse algorithm [104]. Table 4.1.2 shows the total number of nonzero elements in $\mathbf{K}$ for different highest order of spherical harmonics. Here the double Fourier series are in the format as 2.21.

This motivates the following algorithm for Wiener filtering over the unit sphere. First, compute the double Fourier series of the radial function F. Second, the coefficients of

Table 4.1: The total number of nonzero entries in sparse mapping matrix K vs. the highest oder of spherical harmonics basis.

Highest order of basis	2	3	4	5	6
Size of K	9×36	16×64	25×100	36×144	49×196
# of nonzero entry	10	22	41	70	110

double Fourier series are converted to the coefficients of spherical harmonics through the transformation $\mathbf{K}$. After the optimal estimation of spherical harmonics coefficients is obtained through Wiener filtering, they can be mapped back to double Fourier series via $\mathbf{K}$.

4.1.3 Experiment Results

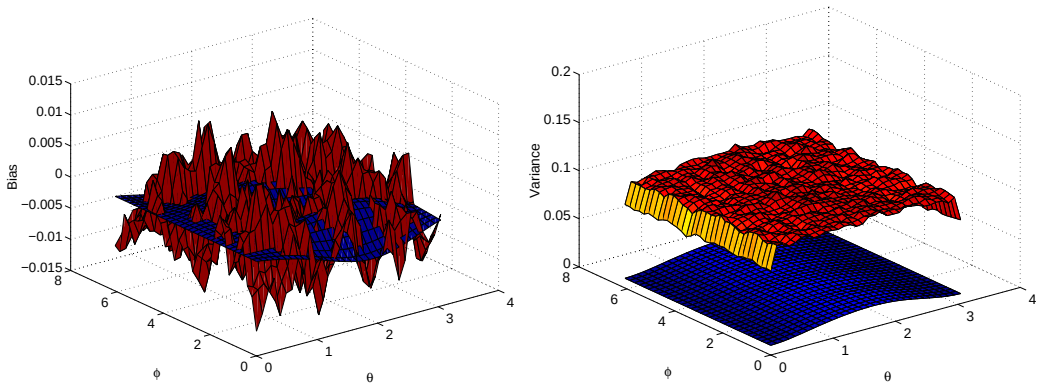

(a) Bias (b) Variance

Figure 4.1: Comparison of linear filtering and Wiener filtering results on S^2. Red surfaces represent the results of linear filtering and blue surfaces represent the results of Wiener filtering.

Applying the spectral theory of isotropic random field, we simulated an isotropic random field over the unit sphere through following steps: First, the covariance function of the random field $\psi(\cos\gamma)$ is decomposed to obtain the value of λ_l. Second, the set of independent random coefficients $\{A_l^m\}$ is simulated by multiplying λ_l with i.i.d Gaussian random variables. Finally, the isotropic random field $X(\theta,\phi)$ is obtained by combining finite number of spherical harmonic basis functions, i.e., $X(\theta,\phi) = \sum_{l=0}^{L}\sum_{m=-l}^{l} A_l^m Y_l^m(\theta,\phi)$.

White Gaussian noise is added to X.

To evaluate the performance of Wiener filtering, we compared it with the linear filtering result. The linear filtering is implemented through a convolution with an average filter. 5000 samples of the random field were generated in the experiment. Figure 4.1(a) shows the bias of Wiener filtering and linear filtering results of the same random field. The red rough surface represents the bias of the linear filtering result, while the relatively flat blue surface represents the bias of Wiener filtering result. It can be seen that the result of Wiener filtering is biased since the blue surface is a little bit below the zero-plane. This is because Wiener filtering tends to shrink the object to a sphere. Alternatives would require a "non-isotropic" filter. In Figure 4.1(b), the variances of the two filtering results are plotted. It can be seen that the Wiener filtering result (blue surface) has a much smaller variance than the linear filtering result(red surface).

4.2 Estimation of 3D Rotation in Image Registration

4.2.1 Review

Finding the rotation of a 3D object is a common problem. A 3D rigid motion maps a 3D image data set to another set. This registration procedure is to align 3D images in a common coordinate system. By computing the centroid of each set, one can translate them in space so that their centroids come to a common coordinate origin. A remaining problem is to determine the 3D rotation between the sets of data. Most techniques for fitting 3D rotation to 3D data estimate the 3D rotation in the spatial domain [62], and usually are of very high computational complexity. Considering the registration of a single 3-D object, Burel [19] proposed to use spherical harmonics as orthogonal basis to decompose the 3D shapes and get the invariants for object recognition. We here develop a maximum likelihood (ML) method to jointly estimate the spherical harmonics coefficients and the

Euler angles of 3D rotation based on Burel's method. The novelty of our method lies on its use of the assumption that the noise field is isotropic Gaussian and thus the decomposed noise coefficients are statistically independent. Since the 3D objects are registered in the frequency domain via low order spherical harmonic coefficients, the registration automatically filters out high frequency noise and has low computational complexity.

4.2.2 Representation of $SO(3)$ by Spherical Harmonics

The degree of freedom of any rotation g in $SO(3)$ is three and g can be defined in terms of Euler angles α, β, γ. In other words, a rotation g which carries the axis x, y, z to new positions x', y', z', can be accomplished by three successive rotations around the coordinate axes, namely a rotation around the z axis through an angle α, a rotation around the new direction of the y axis through an angle β and a rotation around the new direction of z axis through an angle γ. Thus, g has the matrix product representation:

$$\mathcal{R}_g = R_z(\alpha)\, R_y(\beta)\, R_z(\gamma). \tag{4.8}$$

In terms of group theory, the spherical harmonics expand an irreducible representation space of the rotation g [105]. This means the representation space of the rotation $g \in SO(3)$ can be decomposed into a direct sum of orthogonal subspaces which are globally invariant by rotation, i.e.,

$$Ł = D^{(0)} \oplus D^{(1)} \oplus D^{(2)} \oplus D^{(3)} \oplus \cdots \oplus D^{(l)} \oplus \cdots \tag{4.9}$$

where Ł is the linear representation space of the group g and $D^{(l)}$ denotes a $(2l+1)$-dimensional invariant subspace of Ł. The basis for $D^{(l)}$ is $Y_l^m(\theta, \phi), m = -l \ldots l$.

Let the global shape function of a 3D object have a spherical harmonic representation:

$$R(\theta, \phi) = \sum_{l=0}^{K} \sum_{m=-l}^{l} c_l^m Y_l^m(\theta, \phi). \tag{4.10}$$

Applying the 3D rotation operator g to the object $R(\theta,\phi)$ gives a new radial function $\tilde{R}(\theta,\phi) = g(R(\theta,\phi))$, which can also be decomposed by spherical harmonics:

$$\tilde{R}(\theta,\phi) = \sum_{l=0}^{K} \sum_{m=-l}^{l} \tilde{c}_l^m Y_l^m(\theta,\phi). \tag{4.11}$$

The spherical harmonic coefficients $\tilde{c}_l^m$ in (4.11) and c_l^m in (4.10) have the following relationship [105]:

$$\begin{pmatrix} \tilde{c}_0^0 \\ \tilde{c}_1^{-1} \\ \tilde{c}_1^0 \\ \tilde{c}_1^1 \\ \tilde{c}_2^{-2} \\ \tilde{c}_2^{-1} \\ \tilde{c}_2^0 \\ \tilde{c}_2^1 \\ \tilde{c}_2^2 \\ \vdots \end{pmatrix} = \begin{pmatrix} D^{(0)} & & & \\ & \begin{pmatrix} \\ D^{(1)} \\ \\ \end{pmatrix} & & \\ & & \begin{pmatrix} \\ \\ D^{(2)} \\ \\ \\ \end{pmatrix} & \\ & & & \ddots \end{pmatrix} \begin{pmatrix} c_0^0 \\ c_1^{-1} \\ c_1^0 \\ c_1^1 \\ c_2^{-2} \\ c_2^{-1} \\ c_2^0 \\ c_2^1 \\ c_2^2 \\ \vdots \end{pmatrix}$$

which can also be written as

$$\tilde{c}_l^m = \sum_{m'=-l}^{l} D_{mm'}^l(\alpha,\beta,\gamma) c_l^{m'} \tag{4.12}$$

where,

$$D_{mm'}^l(\alpha,\beta,\gamma) \;=\; \exp(-im\alpha) \cdot d_{mm'}^l(\beta) \cdot \exp(-im'\gamma) \tag{4.13}$$

and

$$\begin{aligned} d_{mm'}^l(\beta) \;&=\; (-1)^{l-m'} \sqrt{(l+m)!(l-m)!(l+m')!(l-m')!} \\ &\quad \times \sum_k (-1)^k \frac{(\cos\frac{\beta}{2})^{m+m'+2k} (\sin\frac{\beta}{2})^{2l-m-m'-2k}}{k!(l-m-k)!(l-m'-k)!(m+m'+k)!}. \end{aligned} \tag{4.14}$$

In (4.14), the summation is carried out over all values of k producing positive integers under the factorial symbol.

Example: The matrix $d^l_{mm'}(\beta)$ for $0 \leq l \leq 2$. Let $c = \cos\beta$ and $s = \sin\beta$. Then,

$$d^0(\beta) = 1$$

$$d^1(\beta) = \begin{pmatrix} \frac{1+c}{2} & -\frac{s}{\sqrt{2}} & \frac{1-c}{2} \\ \frac{s}{\sqrt{2}} & c & -\frac{s}{\sqrt{2}} \\ \frac{1-c}{2} & \frac{s}{\sqrt{2}} & \frac{1+c}{2} \end{pmatrix}$$

$$d^2(\beta) = \begin{pmatrix} \left(\frac{1+c}{2}\right)^2 & -\frac{(1+c)}{2}s & \frac{\sqrt{6}}{4}s^2 & -\frac{(1-c)}{2}s & \left(\frac{1-c}{2}\right)^2 \\ \frac{(1+c)}{2}s & \frac{(1+c)}{2}(2c-1) & -\sqrt{\frac{3}{2}}sc & \frac{(1-c)}{2}(2c+1) & -\frac{(1-c)}{2}s \\ \frac{\sqrt{6}}{4}s^2 & \sqrt{\frac{3}{2}}sc & \frac{1}{2}(3c^2-1) & -\sqrt{\frac{3}{2}}sc & \frac{\sqrt{6}}{4}s^2 \\ \frac{(1-c)}{2}s & \frac{(1-c)}{2}(2c+1) & \sqrt{\frac{3}{2}}sc & \frac{(1+c)}{2}(2c-1) & -\frac{(1+c)}{2}s \\ \left(\frac{1-c}{2}\right)^2 & \frac{(1-c)}{2}s & \frac{\sqrt{6}}{4}s^2 & \frac{(1+c)}{2}s & \left(\frac{1+c}{2}\right)^2 \end{pmatrix}.$$

4.2.3 Estimation of 3D Rotation

In section 4.2.2, it is shown that the relationship between two sets of spherical harmonics coefficients describing the surface functions of a 3D object in different orientations can be uniquely determined by a rotation $g \in SO(3)$. In fact, the rotation $g \in SO(3)$ maps the vector space of the spherical harmonic coefficients to the same space, and the mapping is one-to-one and onto. However, different sets of Euler angles may lead to the same rotation g, which means the solution to the inverse problem of Euler angle estimation is not unique. We can either arbitrarily pick one solution or obtain a unique solution by adding some constraints. The rest of this section discusses the rotation estimation using spherical harmonics for objects whose noise fields are isotropic Gaussian random fields (See Appendix B).

The spherical harmonic coefficients before and after rotation can be written as

$$c_l^m \;=\; a_l^m + \eta_l^m \tag{4.15}$$

and

$$\tilde{c}_l^m \;=\; \sum_{n=-l}^{l} D_{mn}^l(\alpha,\beta,\gamma) a_l^n + \tilde{\eta}_l^m \tag{4.16}$$

where $\{a_l^m, l = 1 \ldots K, m = -l \ldots l\}$ is the set of true coefficients of spherical harmonics describing the 3D shape before rotation, η_l^m and $\tilde{\eta}_l^m$ are the zero mean Gaussian noise with variance σ_l^2 and $\tilde{\sigma}_l^2$. By Theorem 5 in Section 2.3.1, η_l^m and $\tilde{\eta}_l^m$ are independent Gaussian random variables for different l and m, and the variance σ_l^2 and $\tilde{\sigma}_l^2$ are determined by:

$$\sigma_l^2 = 2\pi \int_{-1}^{1} \psi(t) P_l(t) dt \tag{4.17}$$

$$\tilde{\sigma}_l^2 = 2\pi \int_{-1}^{1} \tilde{\psi}(t) P_l(t) dt \tag{4.18}$$

where $\psi(t)$ and $\tilde{\psi}(t)$ are the covariance functions of the respective isotropic noise fields, and $P_l(t)$ is a Legendre polynomial.

Therefore, the likelihood functions for c_l^m and $\tilde{c}_l^m$ are:

$$L_{c_l^m} = \exp\left(-\frac{(c_l^m - a_l^m)^2}{2\sigma_l^2}\right), \tag{4.19}$$

and

$$L_{\tilde{c}_l^m} = \exp\left(-\frac{(\tilde{c}_l^m - \sum_{n=-l}^{l} D_{mn}^l(\alpha,\beta,\gamma) a_l^n)^2}{2\tilde{\sigma}_l^2}\right). \tag{4.20}$$

Using the fact $\{\eta_l^m\}$ and $\tilde{\eta}_l^m$ are independent for different l and m, we propose to jointly estimate α, β, γ, and $\{a_l^m\}$ via maximum likelihood:

$$\begin{aligned}
&\{\hat{\alpha}, \hat{\beta}, \hat{\gamma}, \{\hat{a}_l^m\}\} \\
&= \arg \max_{\alpha,\beta,\gamma,\{a_l^m\}} \prod_{l=1}^{K} \prod_{m=-l}^{l} L_{c_l^m} L_{\tilde{c}_l^m} \\
&= \arg \min_{\alpha,\beta,\gamma,\{a_l^m\}} \sum_{l=1}^{K} \sum_{m=-l}^{l} \left(\frac{(c_l^m - a_l^m)^2}{2\sigma_l^2} + \frac{(\tilde{c}_l^m - \sum_{n=-l}^{l} D_{mn}^l(\alpha,\beta,\gamma) a_l^n)^2}{2\tilde{\sigma}_l^2}\right).
\end{aligned} \tag{4.21}$$

Note that the maximum likelihood estimate is equivalent to a weighted least squares fitting problem, which is a nonlinear optimization here. As is the case with many such implicitly defined estimators, the minimum can not be found analytically and iterative minimization of the objective should be employed.

4.2.4 Cramér-Rao Bound for Joint Estimation

To evaluate the performance of joint estimation of spherical harmonics coefficients and rotation angle, we derive the Cramér-Rao lower bound for the variance of the estimator.

Let $L = -\ln \prod_{m=-l}^{l} p(c_l^m|a_l^m)p(\tilde{c}_l^m|\{\{a_l^m\},\alpha,\beta,\gamma\})$. Take derivative of L over a_l^k, we get

$$\frac{\partial L}{\partial a_l^k} = -\frac{(c_l^k - a_l^k)}{\sigma_l^2} - \frac{\sum_{m=-l}^{l}(\tilde{c}_l^m - \sum_{n=-l}^{l} D_{mn}^l a_l^n)\cdot D_{mk}^l}{\tilde{\sigma}_l^2}. \tag{4.22}$$

And the second order derivative of L over a_l^k is

$$\frac{\partial^2 L}{\partial (a_l^k)^2} = \frac{1}{\sigma_l^2} + \frac{\sum_{m=-l}^{l}(D_{mk}^l)^2}{\tilde{\sigma}_l^2}. \tag{4.23}$$

The Fisher information of the coefficients is:

$$E[\frac{\partial^2 L}{\partial {a_l^k}^2}] = \frac{1}{\sigma_l^2} + \frac{\sum_{m=-l}^{l} E[(D_{mk}^l)^2]}{\tilde{\sigma}_l^2}. \tag{4.24}$$

The second term in the above equation demonstrates the profit of joint estimation. The Cramér-Rao bound which is just the inverse of the Fisher information matrix is thus obtained. Similarly, we can derive the lower bound for the rotation angle estimator. We will compare the variance of the estimators with these lower bounds in the next section.

4.2.5 Experimental Results

The proposed estimation method has been implemented to jointly estimate the 3D rotation and spherical harmonic coefficients of the noise contaminated objects. The inputs to the joint estimator are two sets of noisy spherical harmonic coefficients which can be

modeled by (4.15) and (4.16). For each given noise level, 500 independent realizations of the Gaussian noise field were generated for each set of the spherical harmonic coefficients. The mean values of the second set of spherical harmonic coefficients are determined by the product of the mean values of the spherical harmonic coefficients in the first set and the 3-D rotation matrix. For computation convenience, we set $\sigma_l^2 = \tilde{\sigma}_l^2$. Only the first order of spherical harmonics coefficients (c_1^{-1}, c_1^0, c_1^1) and $(\tilde{c}_1^{-1}, \tilde{c}_1^0, \tilde{c}_1^1)$ have been used in the optimization procedure. Higher order coefficients can, of course, be used for the fine tuning, but it will correspondingly increase the computation burden of optimization. The Levenberg-Marquardt algorithm with a mixed quadratic and cubic line search procedure was used via MATLAB function lsqnonlin( ) to find the estimates of Euler angles and shape parameters.

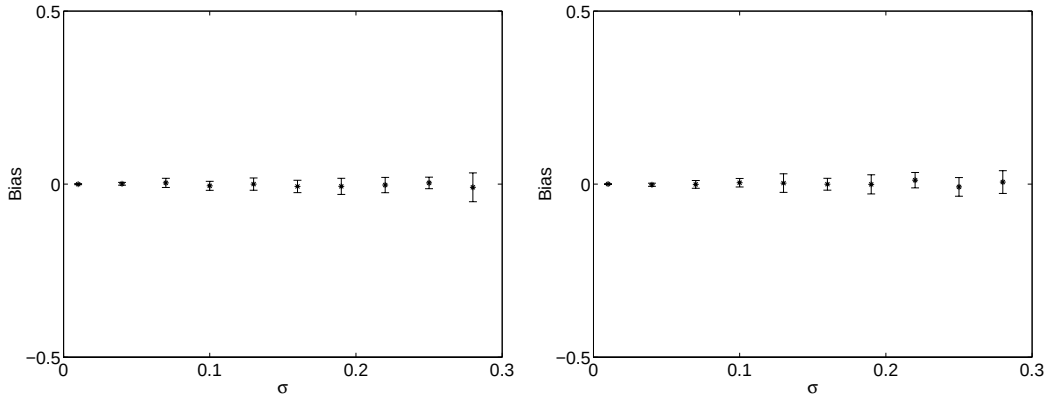

(a) Coefficient $\hat{a}_1^0$ (b) Rotation Angle $\hat{\beta}$

Figure 4.2: Biases of a shape parameter estimator and a rotation angle estimator.

The measured biases of the estimators $\hat{a}_1^0$ and $\hat{\beta}$ are plotted versus the standard deviation of the Gaussian noise in Figure 4.2. From the observed data, we can say that the estimator is basically unbiased. The fact that measured bias deviates from zero, is due to insufficient number of Gaussian noise processes generated in the simulation.

In Figure 4.3, the standard deviations of $\hat{a}_1^0$ and $\hat{\beta}$ are compared to the corresponding

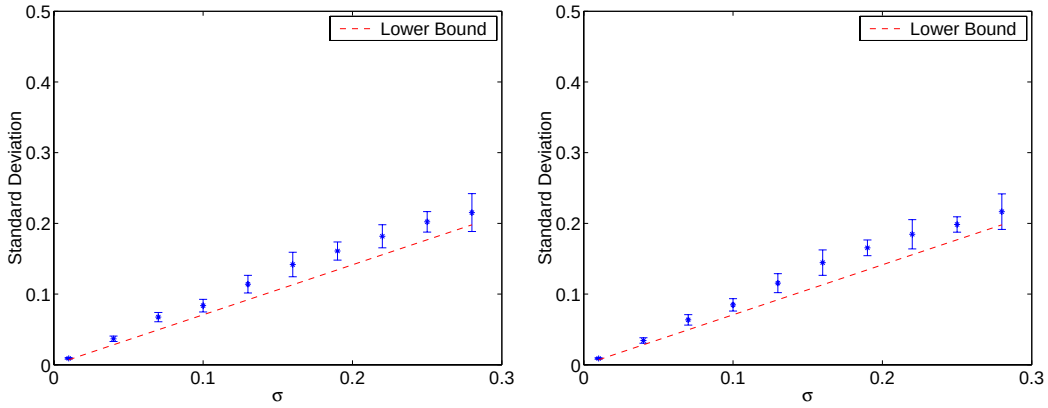

(a) Coefficient $\hat{a}_1^0$ (b) Rotation Angle $\hat{\beta}$

Figure 4.3: Comparison between the estimators' standard deviations and the Cramér-Rao bounds.

Cramér-Rao lower bounds. It can be seen that the standard deviation of the estimators is less than the standard deviation of the noise process. Therefore, the joint estimation has improved the performance of the shape parameter estimator. Since the boundary information in the two sets of images is correlated, this is an expected result. The performances of the two estimators are close to the lower bounds, which shows they are near efficient estimators.

CHAPTER V

SPECTRAL METHOD TO SOLVE ELLIPTIC EQUATIONS IN SURFACE RECONSTRUCTION AND 3D ACTIVE CONTOURS

5.1 Introduction

Automatic recovery of 3D object shapes from various image modalities is an important research area in computer vision and image processing. This task can be accomplished in two steps. First, the object is segmented from the 3D image. Segmentation data is usually stored in the form of coordinates of sampled surface points. Second, a surface reconstruction algorithm is applied to filter the noise in segmentation data and achieve a shape representation of the object. In the last two decades, active contour methods (deformable models) have been developed to solve the segmentation and reconstruction problems simultaneously. Active contours can evolve towards the object boundary under some regularizations. The evolution is controlled by a partial differential equation, where segmentation and reconstruction functions are represented by two different terms in the equation. The existing active contour approaches can be classified into two categories: parametric active contours and geometric active contours.

The class of parametric active contour originates from the "snake" introduced by Kass [63] which uses energy-minimizing curve to locate boundaries in 2D imagery. The dif-

ferent approaches in this class usually intend to deal with some limitations, such as its sensitivities to initialization and noise. The major differences between them lie in the adopted internal and external energy functions. A detailed discussion about the differences can be found in Section 5.3. The geometric active contour methods were proposed independently by Caselles in [21] and by Malladi in [75]. These methods are based on the theory of curve evolution and implemented via level set techniques. Unlike parametric active contours which represent the contour explicitly as parameterized curves or surfaces, the geometric active contours represent the evolving contour implicitly by a special level set function of zero value. This kind of evolving contour can split and merge freely without previous knowledge of the number of objects in the scene. In other words, they can handle the topology change automatically. The disadvantage of geometric active contours is that their computational complexity is much higher than that of parametric active contours. The level set function used by geometric active contour is defined over a 2D or 3D grid in the image domain. In every evolution iteration, the level set method has to update the function at every grid point or at least at the grid points in a narrow band near the propagating front, which causes a heavy burden of computation.

Although these two kinds of active contours have yielded satisfactory results for 2D imagery, their extension to 3D imagery presents major difficulties due to the significant growth of computation. A common step in active contour methods is to solve an associated partial differential equations (PDE). If the grid size is $N \times N$, the computation time of finite difference method (FDM) or finite element method (FEM) is usually in the order of $O(N^4)$, or at least $O(N^3)$, which is intolerable for many practical applications. It is well known that spectral methods have faster rate of convergence than FDM and FEM in solving PDE [50]. This motivates us to explore applying spectral method to solve PDE's in 3D active contours to reduce the computation time. Based on the spherical

geometry of star-shaped object, we propose a new parametric active contour method which uses double Fourier series as the orthogonal basis to solve the PDE defined on the unit sphere. The method is applied to segment both synthesized 3D images and X-ray CT images. It is shown that the new method preserves the merits of other parametric active contour methods while significantly reducing the computation time. Due to the generality of our mathematical formulation, the method can be easily applied to solve the surface reconstruction problem.

Throughout this chapter, the following notations are used:

$I(x, y, z)$, 3D grey-level image;

$\mathbf{x}(u, v)$, surface function in Cartesian coordinates;

$f(\theta, \phi)$, admissible surface function in spherical coordinates;

$g(\theta, \phi)$, noisy radial function obtained from segmentation;

$g := x_g, y_g, z_g$, a set of coordinates of detected edge points;

$g_f(\theta, \phi)$, segmentation data detected by propagating contour f;

$d()$, Euclidean distance function;

μ and α, parameters controlling tradeoff.

5.2 Surface Reconstruction of Star-Shaped Object

Let $g(\theta, \phi)$ be a noisy radial function obtained from the segmentation of a star-shaped object. The surface reconstruction problem is to use some form of regularization to approximate the noisy function $g(\theta, \phi)$ by a smooth reconstruction function $f(\theta, \phi)$. Usually [27], the solution f is a critical point which minimizes the energy functional defined in the form:

$$E(f, g) = \mu \int_{S^2} Y(f, g) d\Omega + \int_{S^2} Z(f) d\Omega_{S^2} \tag{5.1}$$

where Y measures the distance between the function f and the coarse segmentation data g, Z is a measure of reconstruction smoothness, and μ controls the tradeoff between the faithfulness to the segmentation data and the smoothness. The two terms in E represent the faithfulness to the segmentation data and the regularization penalty, respectively. If we define the data fidelity metric $Y(f,g) = (f(\theta,\phi) - g(\theta,\phi))^2$, the approach becomes least squares fitting which is a classic reconstruction method. The regularization term frequently contains the derivative of the function f to enforce smoothness. For instance, Z can be defined to be $Z(f) = ||\nabla f||^2$, where ∇ is the gradient operator. With these choices, the energy functional is completely defined,

$$E(f,g) = \int_{S^2} \mu(f(\theta,\phi) - g(\theta,\phi))^2 d\Omega_{S^2} + \int_{S^2} ||\nabla f(\theta,\phi)||^2 d\Omega_{S^2}. \tag{5.2}$$

The reconstruction objective is to minimize $E(f,g)$ over f. Using the calculus of variations [32], the critical point of the above energy functional can be found by solving the associated Euler-Lagrange equation (See Appendix C):

$$\nabla^2 f - \mu(f - g) = 0. \tag{5.3}$$

This is an elliptic equation of Helmholtz type on the sphere [6]. Although finite difference methods (FDM) and finite element methods (FEM) can be employed to solve this equation, their computational complexities are higher than the spectral method that will be introduced in Section 5.4. For this surface reconstruction problem, elliptic PDE can be solved by spectral method in only one iteration. In the next section, we will show that a PDE similar to (5.3) has to be solved to control the evolution of parametric active contour. It can be solved by the fast spectral method sequentially.

5.3 Parametric Active Contours

As mentioned in the introduction of this chapter, parametric active contour methods can solve the segmentation problem and the reconstruction problem simultaneously. A surface $\mathbf{x}$ in $\mathbb{R}^3$ is a mapping: $\mathbf{x}(u,v) = (x_1(u,v), x_2(u,v), x_3(u,v))$, i.e. $\mathbf{x} : \Omega \rightarrow \mathbb{R}^3$, where Ω is a subset of $\mathbb{R}^2$ [51]. If $\mathbf{x}$ represents a propagating surface in a parametric active contour approach, an energy functional E associated with $\mathbf{x}$ can be defined:

$$E(\mathbf{x}) = \int_{\Omega} \left([\alpha \|\nabla \mathbf{x}\|^2 + \beta \|\nabla^2 \mathbf{x}\|^2] + P_{ext}(\mathbf{x}) \right) d\Omega \tag{5.4}$$

where α and β are the parameters controlling the smoothness of $\mathbf{x}$ and P_{ext} represents a potential function. It is clear that two kinds of energy constitute the energy functional. The term $\int_{\Omega} \alpha \|\nabla \mathbf{x}\|^2 + \beta \|\nabla^2 \mathbf{x}\|^2 d\Omega$, which is computed from the contour $\mathbf{x}$ itself, is called internal energy. The term $\int_{\Omega} P_{ext}(\mathbf{x}) d\Omega$, which is computed from the image and current location of $\mathbf{x}$, is called external energy. The force generated by the internal energy discourages the stretching and bending of the contour, in other words, has regularization effect on the contour, while the force generated by the external energy attracts the contour towards the object boundary. Therefore, the external energy represents the segmentation function of the active contour, and the internal energy represents the reconstruction function of the active contour. The contour $\mathbf{x}$ deforms under these two kinds of forces to find a minimizer of the energy functional E.

5.3.1 External Force Field

The external force field plays an important role in active contour methods. Typically, active contours are drawn towards the desired boundary by the external force which could include one or more of the following components: a traditional potential force, obtained by computing the negative gradient of an attraction potential defined over the image domain

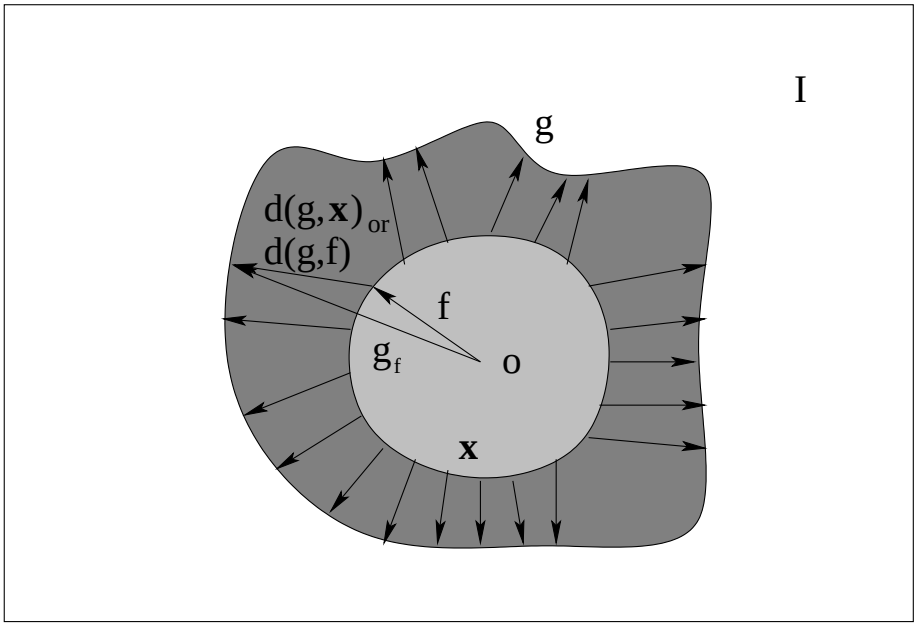

Figure 5.1: An grey level image I, the set of edge points g detected in I, a propagating contour f, and $d(g, \mathbf{x})$ or $d(g, f)$, the distance between the propagating contour and its nearest edge point.

[27, 63]; a pressure force, used by Cohen in his balloon model [27], which could be either expanding or contracting depends on whether the contour is initialized from inside or outside; or a gradient vector flow, used by Xu [108] and obtained by diffusion of edge-map's gradient. The role of the external force is such that it must contain the information of boundary and must have sufficient capture range.

Let $I(x, y, z)$ represent the image to be segmented, $g := x_g, y_g, z_g$ be the set of all edge points detected in I, and $d(g, (x, y, z))$ be the distance from a point (x, y, z) in the evolving surface $\mathbf{x}$ to its nearest edge point, i.e. $d_g(x, y, z) \stackrel{\Delta}{=} \min_{(x_g, y_g, z_g) \in g} \|(x, y, z) - (x_g, y_g, z_g)\|$. Figure 5.1 illustrates the relation between these denotations. Potential functions designed to deform the active contour usually have a global minimum at the object boundary. Two common types of potential functions are:

$$P_{(1)}(\mathbf{x}) = h_1(\nabla I(\mathbf{x})) \tag{5.5}$$

$$P_{(2)}(\mathbf{x}) = h_2(d(g, \mathbf{x})) \tag{5.6}$$

where h_1 and h_2 are functions making $P_{(1)}$ and $P_{(2)}$ convex in at the location of object boundary. For instance, $P(x,y,z) = -|\nabla I(x,y,z)|^2$, $P(x,y,z) = -|\nabla G_\sigma(x,y,z) * I(x,y,z)|^2$ and $P(x,y,z) = \frac{1}{1+|\nabla I|^p}$ belong to the type of $P_{(1)}$. In fact, $|\nabla I|$ serves as an edge detector which locates sharp intensity changes in image I. Although the use of Gaussian filter G_σ can blur boundaries, it is often necessary to use it to increase the capture range of the external force or to deal with the disconnected edges. Figure 5.2 illustrates the attraction force generated by a potential function in 1D case. Potential functions of type

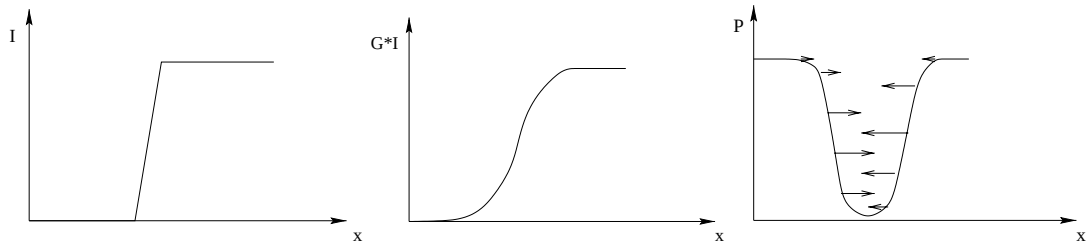

(a) The image I (b) Smoothed image $I * G_\sigma$ (c) $P = -\|\nabla I * G\|^2$ and external force $F = -\nabla P$

Figure 5.2: Interpretation of attraction potential P

$P_{(1)}$ have the disadvantage that the resulting external force has very small capture range because $P_{(1)} \approx 0$ in intensity homogeneous areas. Potential functions of type $P_{(2)}$ solve this problem by incorporating the use of edge points extracted by local edge detectors. The common choices of $P_{(2)}$ are $P(x,y,z) = d^2(g,(x,y,z))$, $P(x,y,z) = \frac{-1}{d(g,(x,y,z))}$ and $P(x,y,z) = -e^{-d^2(g,(x,y,z))}$. The boundary location has been broadcasted to many of their neighbors through the value of d. In our experiment, we chose $d^2(g,\mathbf{x})$, a $P_{(2)}$ type potential function, to generate the external force for the active contour. This external force will evolve the active contour towards the boundary along a path of minimal distance.

5.3.2 Regularization of Active Contour

In (5.4), $\alpha||\nabla \mathbf{x}||^2$ and $\beta||\nabla^2 \mathbf{x}||^2$ control the active contour's elasticity and rigidity separately. The regularization effect coming from $\alpha||\nabla \mathbf{x}||^2$ can be interpreted as a curvature based flow which has very satisfactory geometric smoothing properties [66, 84]. Figure 5.3 shows the motion of a curve under curvature. The curve moves perpendicular to the

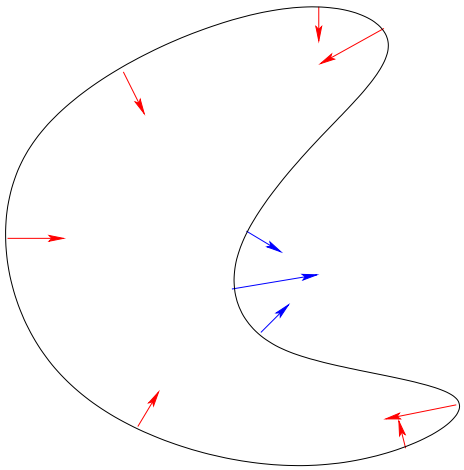

Figure 5.3: Motion of curve under curvature. The blue arrows represent negative curvatures, while the red arrows represent the positive curvatures.

curve with speed proportional to the curvature. The curve motion is outward (inward) where the curvature is negative (positive). A theorem in differential geometry states that any simple closed curve moving under its curvature collapses to a circle and then disappears. Therefore, a bigger α implies a bigger stretching force, so that the active contour resists more the stretching, tends to shrink and have an intrinsic bias toward solutions that reduce the active contour curve length or surface area. On the other hand, a bigger β implies a larger resistance to tensile stress and bending. Therefore, β is often set to zero to allow the active contour to become second-order discontinuous. The equation (5.4) is then reduced to

$$E(\mathbf{x}) = \int_{\Omega} \alpha||\nabla \mathbf{x}||^2 + d^2(g, \mathbf{x}) d\Omega \tag{5.7}$$

For polar shape contours, it will be convenient to convert the surface $\mathbf{x}$ expressed in $\mathbb{R}^3$, into a radial function $f(\theta, \phi)$ which expresses the surface in the object-centered spherical coordinate system. This conversion not only simplifies the contour expression, but also speeds up the contour evolution by allowing spectral method to solve PDE over S^2. The distance function then takes the form of

$$d(g, \mathbf{x}) = d(g, f) \approx \|f(\theta, \phi) - g_f(\theta, \phi)\| \tag{5.8}$$

where g_f is defined as

$$g_f(\theta, \phi) \triangleq \left\| \arg\min_{(x_g, y_g, z_g) \in g} \|(x_g, y_g, z_g) - (f \sin\theta \cos\phi, f \sin\theta \sin\phi, f \cos\theta)\| - (x_o, y_o, z_o) \right\| \tag{5.9}$$

and (x_o, y_o, z_o) represents the coordinates of object center (see Figure 5.1). The equation (5.7) can then be rewritten as:

$$E(f) = \int_{S^2} \alpha \|\nabla f\|^2 + (f - g_f)^2 d\Omega_{S^2}. \tag{5.10}$$

Although equation (5.10) is analogous to equation (5.2), its associated Euler-Lagrange equation is a little different as compared to equation (5.3). Since g_f is a non-linear function of f, the calculus of variations leads to a more complicated Euler-Lagrange equation:

$$\alpha \nabla^2 f - (f - g_f)(1 - \frac{\partial g_f}{\partial f}) = 0 \tag{5.11}$$

There is no analytical expression for $\frac{\partial g_f}{\partial f}$, so we approximated this by difference method in our experiment. To apply the fast spectral method to solve this elliptic PDE, it has to be manipulated so that it becomes a Helmholtz type PDE. We will describe such a manipulation in Section 5.3.4 after we introduce another penalization term into this PDE to deal with a "boundary leakage" problem.

5.3.3 Volumetric Penalization

Traditional parametric and geometric active contours solely rely on the local edge detector to stop the curve propagation. These methods do not use any region-based or volume-based information in the image. Such active contours can only segment and reconstruct objects which boundaries are well defined by gradient $|\nabla I|$ of the image. For objects with very smooth or even broken boundaries, traditional active contour may pass through the boundary. In [23], Chan proposed to use Mumford-Shah energy functional [81] to deal with this "boundary leakage" problem. Similar approaches to include region-based information can also be found in [61] and [97]. We use the same method as in [23] to incorporate the volume information into the energy functional of 3D active contour. The volume information is introduced as an additional penalty function

$$\begin{aligned} E_{\text{vol}}(f) &= \gamma\left(\int_{\text{inside}(f)}(I-u_{in})^2dV+\int_{\text{outside}(f)}(I-u_{out})^2dV\right) \\ &= \gamma\left(\int_{S^2}\left(\int_{r=0}^{f(\theta,\phi)}(I-u_{in})^2r^2dr+\int_{f(\theta,\phi)}^{B(I)}(I-u_{out})^2r^2dr\right)d\Omega_{S^2}\right) \end{aligned} \tag{5.12}$$

where $I = I(r,\theta,\phi)$ is the gray level intensity of the 3D image, $B(I)$ represents the boundary of the image I, and u_{in} and u_{out} are the mean intensities in the interior of the evolving surface f and respectively outside f

$$u_{in}=\frac{\int_{\text{inside}(f)}IdV}{\text{vol}(\text{inside}(f))},\qquad u_{out}=\frac{\int_{\text{outside}(f)}IdV}{\text{vol}(\text{outside}(f))}. \tag{5.13}$$

Here the denominators are the volume inside and outside the evolving surface. The energy function (5.13) can be adjoined to the Lagrangian (5.10) by aggregating the integrals over S^2:

$$\begin{aligned} E(f) = \int_{S^2}\Big\{&\alpha\|\nabla f\|^2+(f-g_f)^2+ \\ &\gamma\Big[\int_0^f(I-u_{in})^2r^2dr+\int_f^{B(I)}(I-u_{out})^2r^2dr\Big]\Big\}d\Omega_{S^2} \end{aligned} \tag{5.14}$$

Now calculus of variations can be applied to obtain the necessary condition for minimization of this volumetrically penalized Lagrangian

$$\alpha\nabla^2 f - (f - g_f)(1 - \frac{\partial g_f}{\partial f}) - \gamma z(f, I) = 0 \tag{5.15}$$

where

$$\begin{aligned} z(f,I) &= f^2 \cdot [(I(f) - u_{in})^2 - (I(f) - u_{out})^2] + 2(\frac{\delta u_{in}}{\delta f}) \int_0^f r^2 (I - u_{in}) dr \\ &\quad + 2(\frac{\delta u_{out}}{\delta f}) \int_f^{B(I)} r^2 (I - u_{out}) dr \end{aligned} \tag{5.16}$$

and

$$\frac{\delta u_{in}}{\delta f} = \frac{\int_{S^2} f^2 I(f) d\Omega_{S^2} - u_{in}\ \text{surf}(f)}{\text{vol}(\text{inside}(f))} \tag{5.17}$$

$$\frac{\delta u_{out}}{\delta f} = -\frac{\int_{S^2} f^2 I(f) d\Omega_{S^2} - u_{out}\ \text{surf}(f)}{\text{vol}(\text{outside}(f))} \tag{5.18}$$

where $\text{surf}(f) = \int_{S^2} f^2 d\Omega_{S^2}$ is the surface area of the evolving contour.

5.3.4 Evolution Algorithm

Comparing equation (5.15) with (5.3), it is clear the Euler-Lagrange equation (5.15) is no longer a Helmholtz PDE. First, the functional dependence of g_f on f makes the equation non-linear in f. Second, the additive volumetric penalization term z is not linear in f and is not "instantaneous" in (θ, ϕ). The same issue was encountered in [61] and the authors got around it by linearization of z with $f_{n+1} = f_n$ and update propagation over (θ, ϕ). "Update propagation" means that for iteration $n + 1$, we update f_n in terms of past iterate $f_n(\theta', \phi')$ if f_{n+1} for (θ', ϕ') has not yet been computed, and partial update $f_{n+1}(\theta', \phi')$ if f_{n+1} for (θ', ϕ') has been computed. This idea can be similarly applied to linearize equation (5.15) so that it has a Helmholtz format which can be solved by the fast spectral method. Combining all the non-linear terms into a single bundle and move it to

the right side of the equation, (5.15) is rewritten as:

$$\alpha\nabla^2 f - f = \gamma z(f, I) - (f - g_f)\frac{\partial g_f}{\partial f} - g_f. \tag{5.19}$$

Due to the non-linearity of equation (5.19), it has to solved iteratively. In the $n+1$ iteration, the right hand side of (5.19) will be updated with the value of f_n so that the equation becomes a new Helmholtz PDE, i.e.

$$\alpha\nabla^2 f_{n+1} - f_{n+1} = \gamma z(f_n, I) - (f_n - g_{f_n})\frac{\partial g_{f_n}}{\partial f_n} - g_{f_n} \tag{5.20}$$

The details of the evolution algorithm is as following:

1. Initialize the evolution with $f_0 = c$, c is determined by the object size;
2. Compute $g_{f_n}(\theta, \phi)$ and update the RHS of (5.20) with f_n and g_{f_n};
3. Solve PDE $\alpha\nabla^2 f_{n+1} - f_{n+1} = \gamma z(f_n, I) - (f_n - g_{f_n})\frac{\partial g_{f_n}}{\partial f_n} - g_{f_n}$ with spectral method to get the new contour f_{n+1};
4. Compute the error, $e_{n+1} = \sqrt{\frac{\sum_{i=0}^{M-1}\sum_{j=0}^{N-1}(f_n(\theta_i,\phi_j) - f_{n+1}(\theta_i,\phi_j)^2}{MN}}$
5. if $e_n >$ threshold, go back to 2,
   else end.

In the above algorithm, α and γ are chosen in advance to control the tradeoff.

5.4 Spectral Methods for Solving PDE

As we have discussed in the last section, the implementation of active contours involves solving partial differential equations. Finite difference [108] and finite element [27] methods have been used to solve the associated Euler-Lagrange equations. However, all of these methods have difficulties in 3D images due to the large grid size used in 3D

images. Spectral and pseudo-spectral methods have emerged as a viable alternative to finite difference and finite element methods for the numerical solutions of partial differential equations. They are now widely used in the numerical simulation of turbulence and phase transition, numerical weather prediction and the study of ocean dynamics where high accuracy is desired for complicated solutions [8, 50, 101, 14, 111]. Since our problem is in spherical geometry, basis functions such as spherical harmonics, double Fourier series and Chebyshev polynomials, all have attractive features. A good comparison of these functions is given by Boyd in [13]. The spherical harmonics are best with regard to the pole problems (recall discussion in Chapter II) because of the property of the associated Legendre functions, but the Legendre functions also make spherical harmonics the most complicated to program and use among the three basis sets. On the other hand, double Fourier series can give comparable accuracy and are significantly easier to program. Most of all, the existing FFT makes double Fourier series the most efficient transform method.

Yee first applied truncated double Fourier series to solve Poisson-type equations on a sphere [112]. Recently, Cheong proposed a new method which is similar to Yee's method, but removes the constraint that is imposed on the spectral coefficients and lead to increased accuracy and stability in a time-stepping procedure [25]. We adopt this new method to solve the associated Euler-Lagrange equation in the active contour evolution.

5.4.1 The Spectral Method

We describe the spectral method proposed by Cheong in this section. The elliptic equation (5.3) $\nabla^2 f - \mu(f - g) = 0$ is a Helmholtz equation. The Laplacian operator ∇^2 on the unit sphere is of form:

$$\nabla^2 = \frac{1}{\sin\theta}\frac{\partial}{\partial\theta}(\sin\theta\frac{\partial}{\partial\theta}) + \frac{1}{\sin^2\theta}\frac{\partial^2}{\partial^2\phi}. \tag{5.21}$$

We assume the value of function f and g are given on the grid (θ_j, ϕ_k), $\theta_j = \pi(j+0.5)/J$ and $\phi_k = 2\pi k/K$, where J and K are the number of data points along the latitude and longitude, separately. We can expand the function g, and similarly for f, with a Fourier series in longitude with a truncation M, e.g.,

$$g(\theta, \phi) = \sum_{m=-M}^{M} g_m(\theta) e^{im\phi_k} \tag{5.22}$$

where $g_m(\theta)$ is the complex Fourier coefficient given by $g_m(\theta) = \frac{1}{K}\sum_{k=0}^{K-1} g(\theta, \phi_k)e^{-im\phi_k}$, $\phi_k = 2\pi k/K$ and $K = 2M$. The equation (5.3) can then be written as an ordinary differential equation:

$$\frac{1}{\sin\theta}\frac{d}{d\theta}\left(\sin\theta\frac{d}{d\theta}f_m(\theta)\right) - \frac{m^2}{\sin^2\theta}f_m(\theta) = \mu[f_m(\theta) - g_m(\theta)] \tag{5.23}$$

The latitude function $f_m(\theta)$ and $g_m(\theta)$ can be further approximated by the truncated sine or cosine functions,

$$\begin{aligned} g_m(\theta_j) = &\quad \textstyle\sum_{n=0}^{J-1} g_{n,0}\cos n\theta_j, && m = 0 \\ g_m(\theta_j) = &\quad \textstyle\sum_{n=1}^{J} g_{n,m}\sin n\theta_j, && \text{odd } m \\ g_m(\theta_j) = &\quad \textstyle\sum_{n=1}^{J} g_{n,m}\sin\theta_j \sin n\theta_j, && \text{even } m \neq 0 \end{aligned} \tag{5.24}$$

The procedure of calculating spectral coefficients $g_{n,m}$ was shown in Chapter II. After the substitution of (5.25) into (5.23), we get an algebraic system of equations in Fourier space:

$$\begin{aligned} \frac{(n-1)(n-2)+\mu}{4}f_{n-2,m} - \frac{n^2+2m^2+\mu}{2}f_{n,m} + \frac{(n+1)(n+2)+\mu}{4}f_{n+2,m} \\ = \mu[\frac{1}{4}g_{n-2,m} - \frac{1}{2}g_{n,m} + \frac{1}{4}g_{n+2,m}], m = 0, \text{or odd} \end{aligned} \tag{5.25}$$

and

$$\begin{aligned} \frac{n(n-1)+\mu}{4}f_{n-2,m} - \frac{n^2+2m^2+\mu}{2}f_{n,m} + \frac{n(n+1)+\mu}{4}f_{n+2,m} \\ = \mu[\frac{1}{4}g_{n-2,m} - \frac{1}{2}g_{n,m} + \frac{1}{4}g_{n+2,m}], m \text{ even} \neq 0 \end{aligned} \tag{5.26}$$

where $n = 1, 3, \cdots, J-1$ for odd n, $n = 2, 4, \cdots, J$ for even n if $m \neq 0$ and $n = 0, 2, \cdots, J-2$ for even n, $n = 1, 3, \cdots, J-1$ for odd n if $m = 0$. This says the components of even and odd n are uncoupled for a given m. The equations (5.25) and (5.26) can be rewritten in matrix format,

$$B\mathbf{f} = A\mathbf{g} \tag{5.27}$$

where B and A are matrices of size $J/2 \times J/2$ with tridiagonal components only, $\mathbf{f}$ and $\mathbf{g}$ are column vectors whose components are the expansion coefficients of $f_m(\theta)$ and $g_m(\theta)$. For example, the subsystem for odd n looks like this:

$$\begin{pmatrix} b_{1,m} & c_1 & & & & \\ a_3 & b_{3,m} & c_3 & & & \\ & \ddots & \ddots & \ddots & & \\ & & a_{J-3} & b_{J-3,m} & c_{J-3} & \\ & & & a_{J-1} & b_{J-1,m} \end{pmatrix} \begin{pmatrix} f_{1,m} \\ f_{3,m} \\ \vdots \\ f_{J-3,m} \\ f_{J-1,m} \end{pmatrix} =$$

$$\begin{pmatrix} 2 & -1 & & & \\ -1 & 2 & -1 & & \\ & \ddots & \ddots & \ddots & \\ & & -1 & 2 & -1 \\ & & & -1 & 2 \end{pmatrix} \begin{pmatrix} g_{1,m} \\ g_{3,m} \\ \vdots \\ g_{J-3,m} \\ g_{J-1,m} \end{pmatrix}$$

The procedure to solve the equation (5.3) is as follows: First, we get $g_{n,m}$, the spectral components of $g(\theta, \phi)$ by double Fourier series expansion. Then the right hand side of (5.27) is calculated to obtain the column vector $\mathbf{g}_1 = A\mathbf{g}$. Finally, the tridiagonal matrix equation $B\mathbf{f} = \mathbf{g}_1$ is solved and $f(\theta, \phi)$ is obtained by inverse transform of $f_{n,m}$. Notice that the Poisson equation $\nabla^2 f = g$ is just a special case of Helmholtz equation, a slight modification in the above algorithm will give the solution to Poisson equation. Other

simple elliptic equations, such as biharmonic equations can also be solved by this spectral method.

5.4.2 Complexity Analysis

Let us consider an elliptic equation with a grid size of $N \times N$ on unit sphere. If FEM were used, there would be a total of N^2 variables with matrix size $N^2 \times N^2$. A crude Gauss elimination method will require $O(N^6)$ operations and the Gauss-Siedel relaxation will require $O(N^4)$ operations to converge. If the algorithms can use the fact that the matrix is sparse, it may reduce the number of operations to $O(N^3)$. However the computational complexity of the spectral method described above is only $O(N^2 \log N)$ (see [25]). The complexity of the spectral method on the unit sphere is in the same order as that of FEM method applied on a grid over a rectangle.

5.5 Experimental Results

We now present the results of applying the spectral method to solve the elliptic equations involved in the problems of surface reconstruction and 3D active contours.

5.5.1 Surface Reconstruction

For the surface reconstruction problem, we apply the algorithm to some synthesized segmentation data to show how to choose the regularization parameter μ for different noise levels and for different shapes. The object center is assumed to be known or to have been estimated in advance.

In the first experiment, we investigate the optimum value of μ for different shapes. The reconstructions of a sphere and an ellipsoid are compared to illustrate the role of μ. The Gaussian segmentation noise has been introduced and the standard deviation of the noise in each sample direction is the same. In Figure 5.4, the reconstruction error is plotted

versus the value of μ for two shapes. The straight line represents the standard deviation of the segmentation noise. The figure shows that for a simple shape which only contains low spatial frequency, such as the sphere, the value of μ should be as small as possible in order to filter out segmentation noise, while for a shape containing higher spatial frequencies, such as the ellipsoid, μ should be optimized to control the tradeoff between denoising and matching high spatial frequencies. The optimum value of μ is between 10^1 and 10^2 for the ellipsoid shape. If μ is too small, we will lose the high frequencies contained in ellipsoid shape. If μ is too high, the segmentation noise can not be get rid of efficiently. This is due to the fact that unweighted Laplace operator is adopted for roughness penalty. Therefore it acts as the prior shape is a sphere. Possible improvement is to induce other priors via weighted Laplacian.

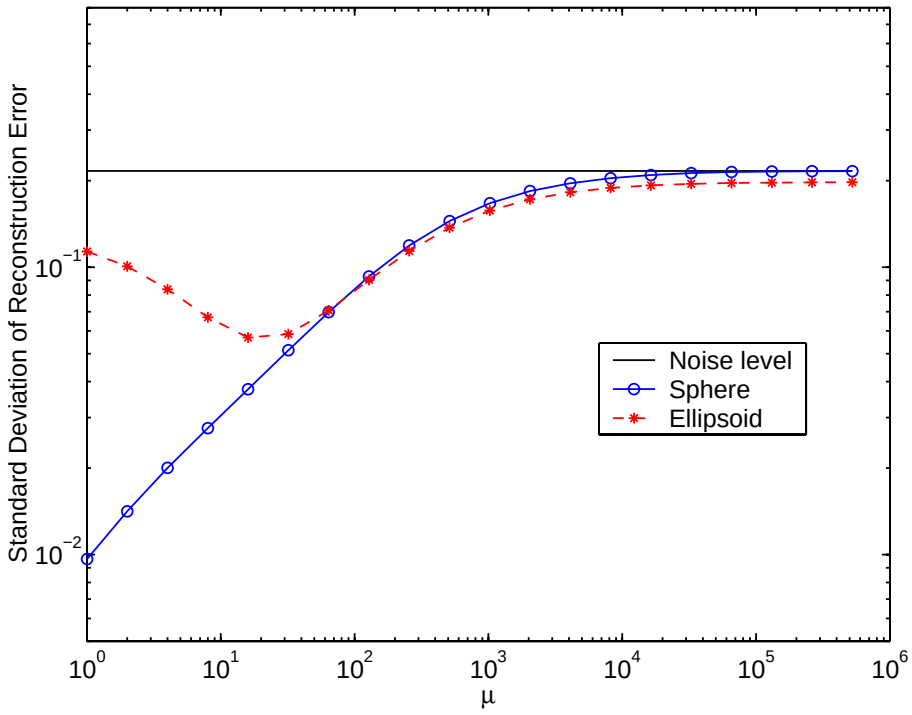

Figure 5.4: Standard deviation of reconstruction error vs. μ for different shapes

The optimum value of μ not only changes with different shapes, but also with different noise levels. In the second experiment, the choice of μ for different segmentation noise

levels is investigated. Different levels of Gaussian noise are added to the ellipsoidal shape. Figure 5.5 shows that μ should be smaller for low SNR segmentation data than for high SNR segmentation data, which is as expected. The knowledge of μ obtained in the reconstruction problem can guide us to choose the value of α in active contour method which has an inverse role as μ.

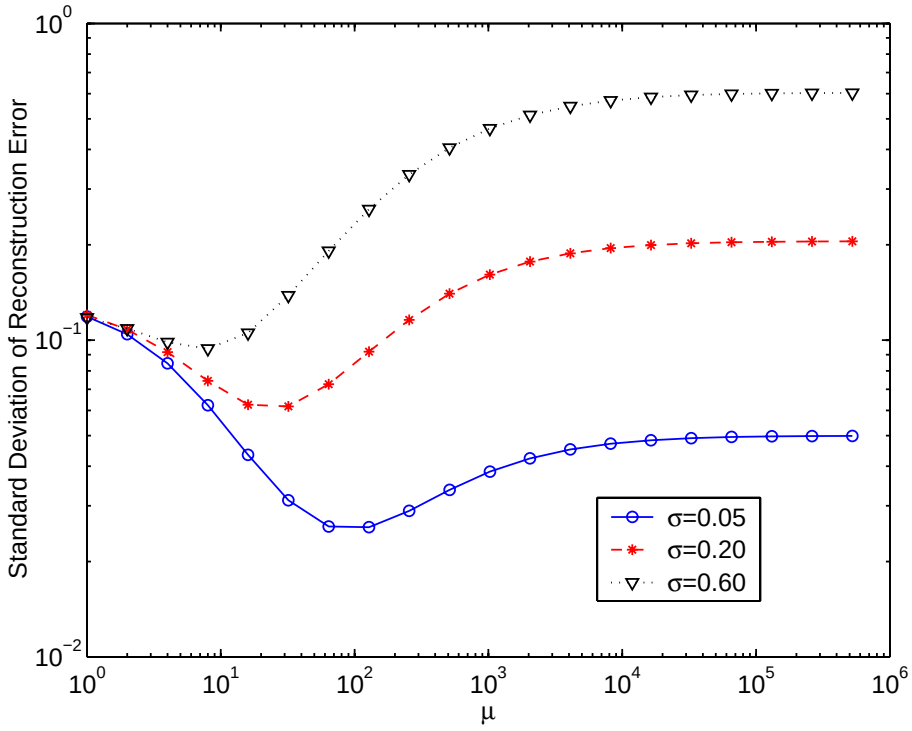

Figure 5.5: Standard deviation of reconstruction error vs. μ for different segmentation noise levels

Three reconstructions of the same segmented ellipsoid are presented in Figure 5.6. The smoothness of the reconstructed surfaces is determined by the value of μ.

Surface reconstruction can be accomplished in one iteration by the spectral method, while a single-grid relaxation algorithm may need more than 100 iterations to reach the converged result.

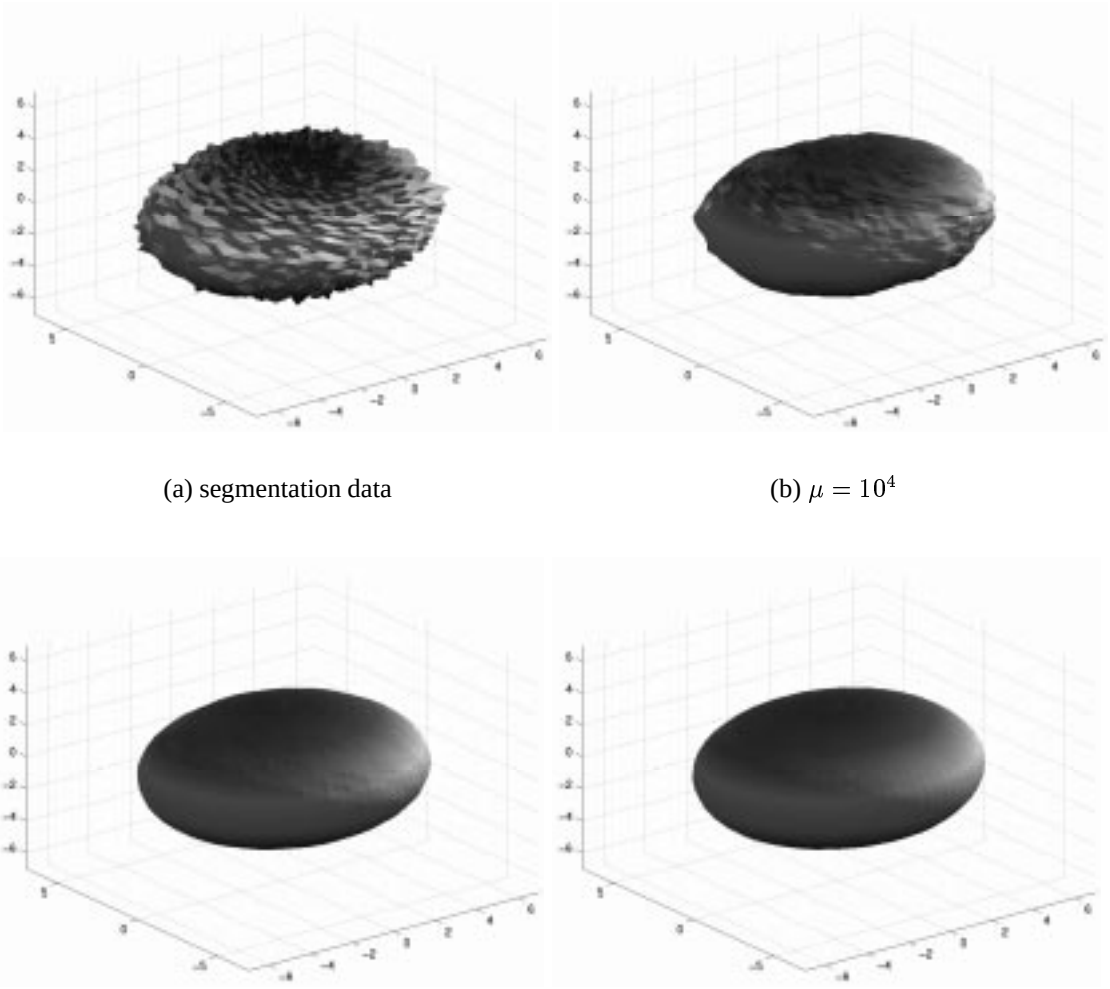

(a) segmentation data

(b) $\mu = 10^4$

(c) $\mu = 10^3$

(d) $\mu = 10^2$

Figure 5.6: Reconstruction of an ellipsoid.

5.5.2 3D Parametric Active Contours

5.5.2.1 Liver Shape Extraction

In this experiment, we want to extract the shape of liver from X-ray CT images. Double Fourier series were used to expand the radial function of the 3D contour. First, a set of edge maps was derived from the 256×256 CT slices by MATLAB function edge(). It is the input to our 3D active contour method. The CT slices and the corresponding edge maps are shown in Figure 5.7.

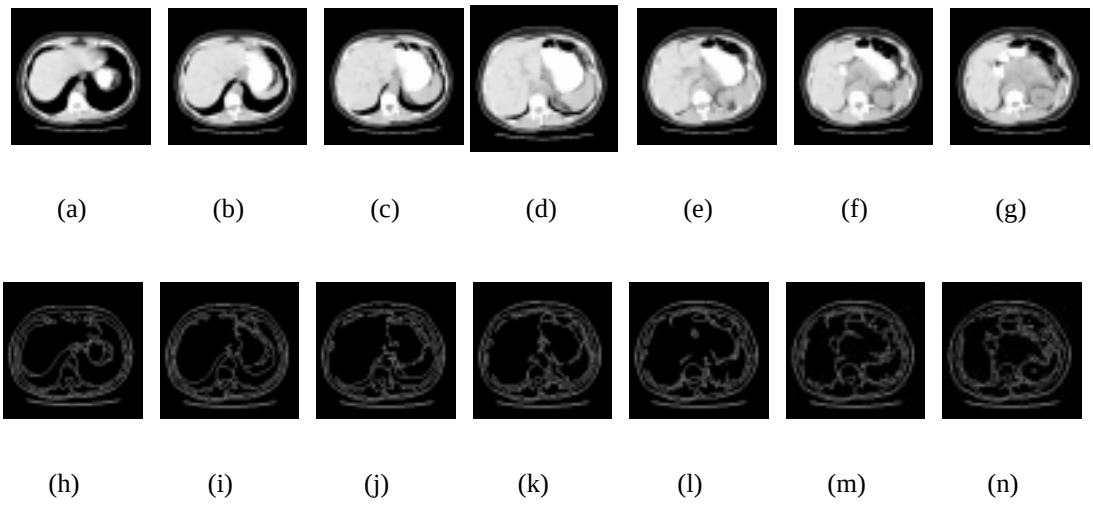

(a) (b) (c) (d) (e) (f) (g)

(h) (i) (j) (k) (l) (m) (n)

Figure 5.7: CT slices and the corresponding edge maps

As in the surface reconstruction problem, the center of liver was estimated in advance. Although it was not implemented in our experiment, iterative center estimation along the contour evolution could in principle be applied here. The contour was initialized as a sphere inside the liver. A 32×32 grid was used in the 3D active contour. Let g represents the set of edge points contained in the edge maps. In nth iteration, g_{f_n} is determined from f_n and g. The elliptic equation is then solved to propagate the active contour to the new position f_{n+1}. Because the boundary information extracted by local edge detector has been integrated in the PDE, the average distance from the evolving contour to its convergent limit is within one pixel after only 5 iterations.

Figure 5.8 shows in that particular CT slice, contours solved with different value of α converge at different positions. When $\alpha = 10^{-3}$, the contour is over regularized and trapped by wrong edge points. When $\alpha = 10^{-6}$, the regularization effect is so weak that the converged contour is the almost the same as that without any regularization. When $\alpha = 10^{-4}$, we observe a pretty satisfying segmentation result. This further explains the importance of optimizing α.

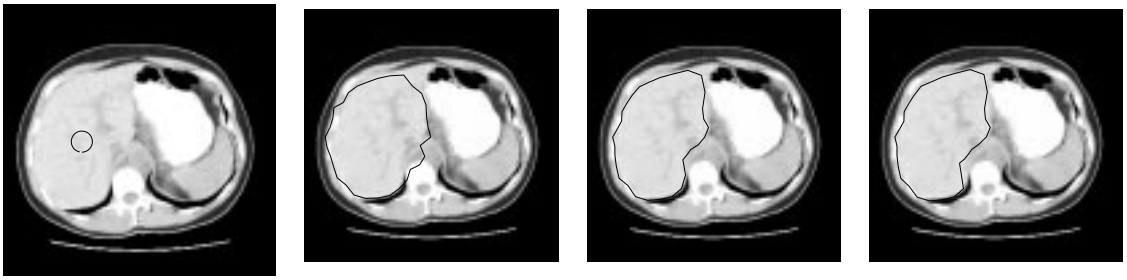

(a) Initialization (b) $\alpha = 10^{-3}$ (c) $\alpha = 10^{-4}$ (d) $\alpha = 10^{-6}$

Figure 5.8: Contours solved with different α converge at different positions.

Figure 5.9(a) shows a coarse liver surface which was segmented by local edge detector without any regularization. The liver surface segmented by the active contour with $\alpha = 10^{-4}$ is shown in 5.9(b). The second surface is smoother than the first one.

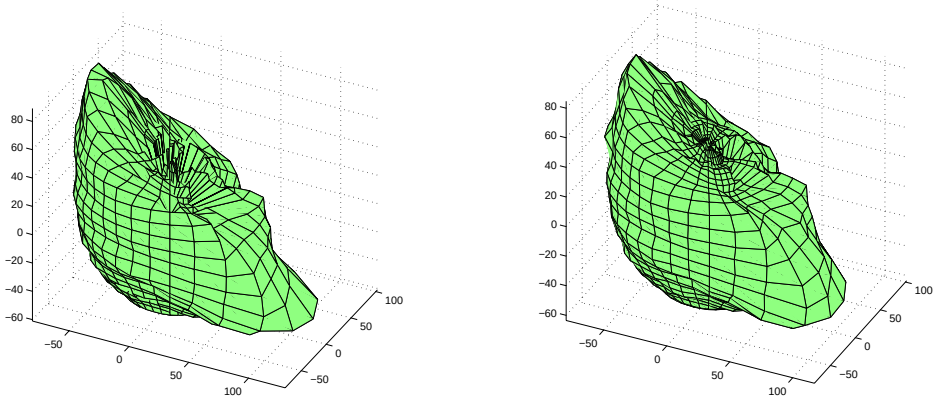

(a) Local edge detector (b) $\alpha = 10^{-4}$

Figure 5.9: Comparison of shape extraction results. (a) Local edge detector; (b) Active contour.

5.5.2.2 Active Contour with Volumetric Penalization

The active contour with volumetric penalization is applied to synthesized image to show the effect of leakage prevention. An ellipsoid is contained in a $128 \times 128 \times 64$ image. One side of the ellipsoid boundary has been blurred with a linear filter, which

is shown in Figure 5.10(a). This blurred image and its edgemap are the inputs to the new algorithm. Figure 5.10(b) shows that the traditional algorithm can not prevent the contour from leaking at the blurred boundary. Figure 5.10(c) illustrates that the contour with volumetric penalization can stop at the right place. The small fluctuation of the converged active contour boundary is caused by the constant value of γ. In this experiment, we chose $\alpha = 10^6$ and $\gamma = 5\alpha$. The penalization in each direction is proportional to f^2 and generates the bias in the converged contour. How to automatically choose the parameters α and γ is a topic worth of additional study.

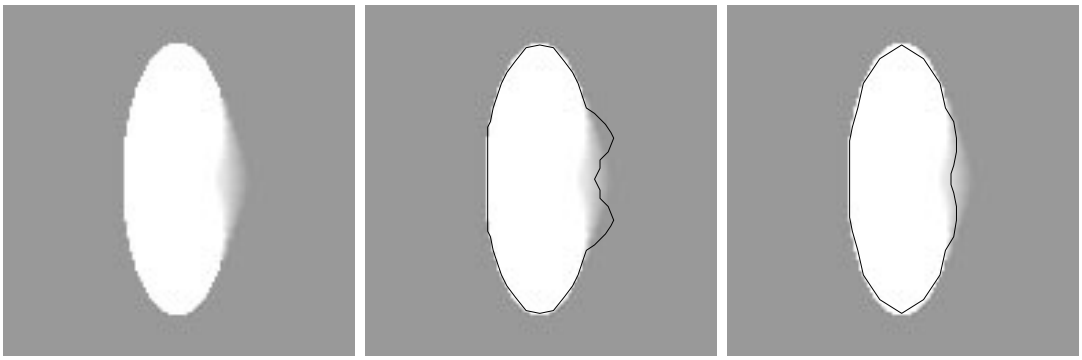

(a) Edge-blurred Ellipsoid

(b) No Volumetric Penalization

(c) With Volumetric Penalization

Figure 5.10: Segmentation results comparison between the active contours with and without volumetric penalization for edge blurred image

5.6 Conclusions

In this Chapter, we have discussed the formulation of surface reconstruction and 3D active contours in the context of variational principles. It is shown that these problems lead to solve elliptic equations on the unit sphere. A spectral method using double Fourier series as orthogonal basis functions has been applied to solve the elliptic equations. Compared to the complexity of $O(N^3)$ for iterative methods, the complexity of $O(N^2 \log N)$ for spectral method is much lower. Some experimental results for surface reconstruction

and 3D active contours were presented to illustrate the algorithms. To improve the segmentation result, we incorporate the volume information obtained from image I into the segmentation procedure via volumetric penalization term in the energy function of the active contour. The new algorithm can prevent the contour from leaking at blurred boundaries. The optimization of the regularization parameters requires further study.

CHAPTER VI

ADJUSTMENT OF RIGID CT-SPECT REGISTRATION THROUGH MAXIMIZING COUNTS IN TUMOR VOI

6.1 Introduction

Accurate estimation of tumor activity is of great importance in therapy planning and response monitoring in nuclear medicine. Single photon emission computed tomography (SPECT) is widely used as the functional image. The goal of SPECT is to determine the regional concentration of radionuclide within a specific organ as a function of time [60]. The radioisotope, such as Tc-99 or I-131, emits single gamma ray photons that are easily detected by a gamma camera. After gamma rays pass through the collimator, they interact with NaI crystal. The light signals generated in the interaction are collected and analyzed to yield projection images. Producing a SPECT image from a set of projections is a rather complicated procedure. The issues that must be considered include [90]: compensation for attenuation and scatter, spatial resolution, energy resolution, image slice thickness, reconstruction matrix size and filter, statistical variations in detected counts, changes in camera field of view with distance from the source, and system deadtime.

To better quantify tumor activity, CT and SPECT can be fused to enhance the information provided by either single modality through precise anatomical-functional correlation. Historically, Kramer *et al* [69] used CT-SPECT fusion to identify anatomic sites in

the SPECT image set. The fusion process depends on an accurate registration of the CT and SPECT images, which matches CT and SPECT coordinates. After two image sets are properly registered, comparative slices can be created and overlayed for any arbitrary point and orientation through re-sampling and interpolation. This step is called fusion. Image analysis techniques discussed in previous chapters, such as image segmentation and shape modeling, are also involved in the activity quantification procedure. They identify VOI's in CT images.

Our activity quantification procedure for lymphoma patients has been characterized in print [67, 68]. First, filtered backprojection produced an initial SPECT reconstruction without attenuation correction. A patient CT image set was then registered with this SPECT image set. Let T represent the transformation matrix which maps CT to the coordinate system of SPECT. The matrix T usually was obtained from a mutual information based registration [100] of the two image sets (6 of the 7 patients discussed here). In rare cases, we also used control points matching method [17] which minimizes mean square error between pairs of markers. The "MIAMI fuse" software developed by Meyer *et al* was used to accomplish both types of registration and fusion [80]. Although warping can be helpful in dealing with non-rigid transformation between two image sets, the results of warping are not as reliable as rigid registration results. So the registration in our study was restricted to a rigid rotate-translate transformation. However, the radius for the multi-dimensional vector which defined the limits for a new set of control points for a new iteration, as well as the stopping criterion, was varied by the author in a search for the "best overall" fusion.

The final reconstruction of SPECT that included deadtime, attenuation and scatter correction was implemented by the iterative space-alternating generalized expectation-maximization algorithm (SAGE) [43]. Here, the attenuation map was obtained through

down-sampling CT after it was registered with SPECT. Finally, the inverse of the transformation T obtained in the previous registration was used to map SPECT into the CT space where the tumor volumes of interest (VOI's) were segmented. However, the ultimate accuracy of the estimate of tumor activity based on this procedure was difficult to establish. Inaccuracy can be caused by "registration error" which in turn comes from several factors. Depending on the type of registration, these factors include: 1) a non-rigid change in the body habitus between CT and SPECT; 2) a change in the tumor location relative to the large organs or relative to the skin markers; 3) poor choice of the control points that initialize a mutual information (MI) based registration; 4) non-optimum choice of other parameters in MI registration; 5) failure of maximum MI to yield a good registration even with the optimal choice of input parameters.

In this chapter, we explore the possibility of optimizing the estimate of tumor location in SPECT for the purpose of activity quantification. Rigid registrations driven by global measures, such as mutual information between two image sets, may have to sacrifice local fitting accuracy to achieve optimal global volume registration, and so may not yield an optimal estimate of a small tumor's location. Total counts in tumor VOI is a local measure of goodness-of-fit as opposed to a global measure. This criterion is proposed because we assume the soft tissue, organs or any other objects adjacent to the tumors have a lower activity concentration than that in the tumors (however, see the results section 6.3). A local variation on the inverse of T, with the criterion of maximizing counts in the VOIs of known tumors, is applied to the second registration of CT and SPECT in our activity quantification procedure. The tumor activity estimated from the new location of the tumor VOIs in the SPECT image set is then compared to the activity found from the fusion based on global registration. The latter method has up to this time been adopted for activity quantification of patient data in our research group at the University of Michigan.

6.2 Methods

6.2.1 Initial CT-SPECT Registration, Final SPECT Reconstruction

We describe an initial rigid 3D registration by a transformation matrix T. Let $\mathbf{x}_0 = (x_0, y_0, z_0)$ and $\mathbf{x}_1 = (x_1, y_1, z_1)$ be the coordinates of the CT image before and after the registration, respectively. The transformation equation is: $\mathbf{x}_1 = T \cdot \mathbf{x}_0$. After the initial rigid registration and calculation of the attenuation map, the next step was to input the attenuation map, the raw projection data corrected for deadtime, and projection images that estimated scatter into the iterative SAGE algorithm [43]. This algorithm reconstructed the final SPECT image set while compensating for attenuation and scatter. Let I_{SPECT} represent the final SAGE-reconstructed SPECT image. The last step in the old procedure involved using the inverse of the transformation T to transform I_{SPECT} into the CT space. The new step introduced here involves extracting tumor position information from both the registered CT image and the reconstructed SPECT image as opposed to a simple inverse of the transformation T. This is equivalent to changing the basis for the registration objective function from mutual information to mean uptake intensity over the tumor volume.

6.2.2 Local Optimization by Maximizing Counts in Tumor VOI

First, we generate a 3D binary image I_{VOI}, which is an indicator function, i.e.

$$I_{VOI}(x, y, z) = \begin{cases} 0 & (x, y, z) \notin \text{VOIs}, \\ 1 & (x, y, z) \in \text{VOIs}. \end{cases} \tag{6.1}$$

The new iterative registration is then carried out: the image I_{VOI} is registered with I_{SPECT} so that the net counts inside the VOIs for tumors are maximized. The objective function L can be written as:

$$L_{obj} = \sum_{(x,y,z)\in\Omega} I_{SPECT}(\mathcal{T}(x, y, z)) \cdot I_{VOI}(x, y, z). \tag{6.2}$$

where Ω is the image domain of CT, and $\mathcal{T}$ is the new transformation matrix sought by the optimization algorithm. We use the Nelder-Mead simplex algorithm [88] to find $\mathcal{T}$ which can maximize the above objective function, i.e. $\hat{\mathcal{T}} = \arg\max_{\mathcal{T}} L_{obj}$. There are six degrees of freedom in the matrix $\mathcal{T}$. Three of them are rotation angles and the other three are translation distances. The initial guess for the new iterative registration is always the inverse of T, i.e. $\mathcal{T}_0 = T^{-1}$, where T was obtained in the first registration by MIAMI fuse or other global volume registration method. The search of optimum $\mathcal{T}$ was also limited to a neighborhood of T^{-1}.

6.2.3 Patient Image Sets Involved

We have implemented the algorithm described above and tested it on three groups of patients with lymphoma [68]. These patients had known tumors that were located either in the abdomen or the pelvis or in both.

The patient with ID#7 had two abdominal tumors and two pelvic tumors that were captured in a single camera field of view. We investigate a number of registration variations for him in order to obtain a satisfactory result. Included among the variations is maximizing the counts in the abdominal tumors separately from those in the pelvic tumors and vice versa, as well as maximizing the counts in single tumors.

The starting point for the new count-maximization registration method was the previously accepted total volume registration. Some characteristics of the previously accepted registrations were as follows. For abdominal scans, 1) the locations of the liver and spleen, which both had considerable uptake, were taken into account in judging the fusion quality, and 2) the location of the kidneys, which usually had some reduced uptake, was taken into account as well. The approximate location of abdominal tumors was not considered at the beginning of the research, in order to not bias the result, but it was used more as the pro-

cessing of patients continued and the difficulty of judging what constituted a good fusion became more apparent. For the pelvis, the scanning of which came after considerable experience with scanning the abdomen, usually only the location of the tumors could provide guidance as to the quality of the fusion. For both regions of the body, the tumor outlines were applied to the final result as a check on the fusion quality. If results were felt to be poor, another cycle of seeking a registration was initiated. At most, two final results with tumor outlines placed on the images were generated, and a selection was made between them based on the visual check of the fusion result.

6.3 Results

Figure 6.1(a) shows one transverse slice from the x-ray CT image set for a patient with ID#62. A contour which was manually drawn by a radiologist outlines the right pelvic tumor, called "rpel," in white. To the left of Figure 6.1(b), the contour is shown on the final reconstructed SPECT which has been registered with the CT image by the inverse of the initial mutual-information-based registration. The location of the contour shows a mismatch between the VOI and what would appear to be the tumor location (that is, the location having high activity shown in red). To the right of Figure 6.1(b), the location of tumor VOI has been locally optimized based on the net max-counts criterion. The new registration of the VOI appears to be better than the initial result. Notice that although the figure only shows the result for a single 2-D slice, the optimization is performed in 3-D. The new count total for the entire tumor is shown in Table 6.1. The activity estimate for this tumor is proportional to this count total. The table also gives the tumor volume, the count total from the original fusion based on the inverse of the transformation T, and the percent difference. The table shows that for patient #62 there is a substantial count increase for one of her two tumors. For the other patient, there is only a moderate increase

in his one tumor.

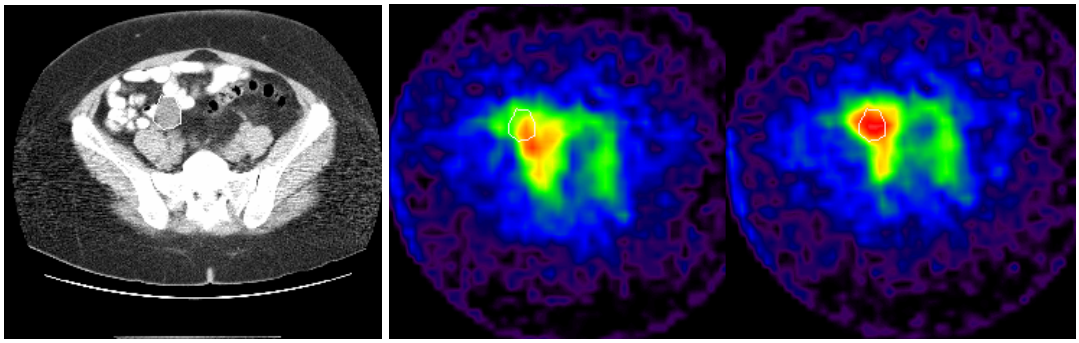

(a) CT image (b) old and new fusion results

Figure 6.1: CT-SPECT fusion results comparison for patients 62

Table 6.1: Results from net-counts maximization for patients with pelvic tumors

Patient ID#	Tumors	Volume cm^3	Original Counts $\times 10^{12}$	New Counts $\times 10^{12}$	Change %
62	"rpel"	330	1.07	1.28	+19.6
	"lpel"	316	1.11	1.15	+3.87
53	"big"	281	1.38	1.43	+3.62

The results from the patients with abdominal scans are given in Table 6.2. The net count for their tumors is maximized in each case. For two patients with ID#14 and #47, the percent increases are small. For one patient with ID#2, the percent increases for his two tumors are more substantial (18.1% and 7.5%). For the last patient #66, the increase in his large tumor is moderate (3%) and there is actually a large decrease in his small tumor (30%). But the overall counts in the two tumors of patient 66 still increase. Visually, the new result for the patient with ID#2 appears to be an improvement, although the images are not shown here.

Figure 6.2 shows one 2-D slice from the fusion that maximizes the net count for the two abdominal and the two pelvic tumors in the patient with ID#7. One sees that the "big"

Table 6.2: Results from net-counts maximization for patients with abdominal tumors

Patient ID#	Tumors	Volume cm^3	Original Counts $\times 10^{12}$	New Counts $\times 10^{12}$	Change %
2	"inf"	68.9	0.210	0.248	+18.1
	"sup"	33.8	0.160	0.172	+7.50
14	"kid"	53.6	0.804	0.804	+0.00
	"ant"	40.2	0.546	0.547	+0.183
47	"laor"	13.2	0.0439	0.0440	+0.228
66	"big"	299	3.00	3.09	+3.00
	"post"	17.2	0.128	0.0902	-30.0

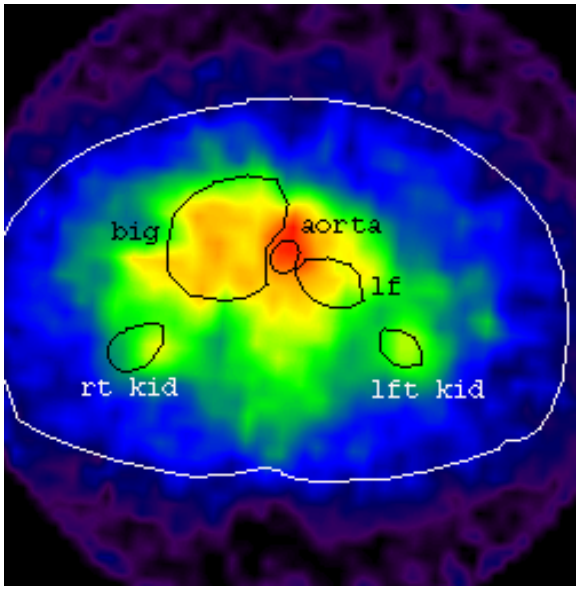

Figure 6.2: The net-count-maximization result for the patient with ID#7. Reconstructed SPECT slice corresponds to CT IM 41.

tumor and the "lf" tumor, which are the two abdominal tumors, both seem correctly positioned next to the aorta which separates them and which probably has considerable activity remaining in the blood it contains. The kidney VOIs appear positioned in approximately the correct place, although they give the impression that the horizontal scale, which is set by a camera calibration and not adjusted by the fusion, may have changed from when it was measured and is slightly incorrect. The tumors do not appear to have a completely uniform activity distribution (some regions are red or orange, but others are green denoting

lesser activity), but that is not surprising. The count totals for all 4 tumors from this fusion are shown in Table 6.3. The count changes for the abdominal tumors are encouraging. For "big", the increase in counts is 25.1% and for "lf" it is 8.94%.

Table 6.3: Results for patient (ID#7) with tumors in both the abdomen and pelvis from net-count maximization of all 4 of his tumors.

Tumors	Volume cm^3	Original Counts $\times 10^{12}$	New Counts $\times 10^{12}$	Change %
"big"	455	2.19	2.74	+25.1
"lf"	135	0.770	0.839	+8.94
"lfpel"	111	0.449	0.663	+47.3
"rtpel"	6.8	0.0419	0.0327	-22.1

However, the count changes for the pelvic tumors are not as encouraging as those for the abdominal tumors. That is, the "lfpel" tumor count goes up by 47.3% but the "rtpel" tumor count goes down by 22.1%. Since the pelvic tumors have less counts by about an order of magnitude than the abdominal tumors, it is likely their count is not influencing the fusion very much and so their result is less reliable. Also, due to the good possibility of a body flexion at the boundary between the abdomen and pelvis that was different for the SPECT scan compared to the CT scan, it makes sense to consider a fusion that maximizes the counts in the lower part of the abdomen independently of those in the upper part of the pelvis, and vice versa. Such count-maximization fusions were carried out for this patient.

Table 6.4: Results for counts in abdominal tumors for patient (ID#7) using different tumors, or different tumor combinations, for the count maximization.

Tumors used in maximizing counts	"big" % change	"lf" % change
"big"	+31.7	-11.6
"lf"	-5.08	+14.9
"big" and "lf"	+23.5	+4.79
all 4 tumors	+25.1	+8.94

When a maximization of only the counts for the two abdominal tumors is performed, a

slightly different fusion is obtained, but the count increases are almost as great as with the fusion based on maximizing the counts in all four tumors (23.5 compared to 25.1 for "big" and 4.79 compared to 8.94 for "lf" as shown in Table 6.4). For our summary statistics given in a paragraph below, we use the higher values.

Table 6.5: Results for counts in pelvic tumors for patient (ID#7) using different tumor combinations for the count maximization.

Tumors used in maximizing counts	"rtpel" % change	"lfpel" % change
"rtpel" and "lfpel"	+6.24	+26.7
all 4 tumors	-22.1	+47.3

A separate fusion for the pelvis appears to provide a better result than the 4-tumor-count-maximization fusion. The count results for the pelvic tumors with this technique are shown in Table 6.5. This time, there is an increase for both pelvic tumors.

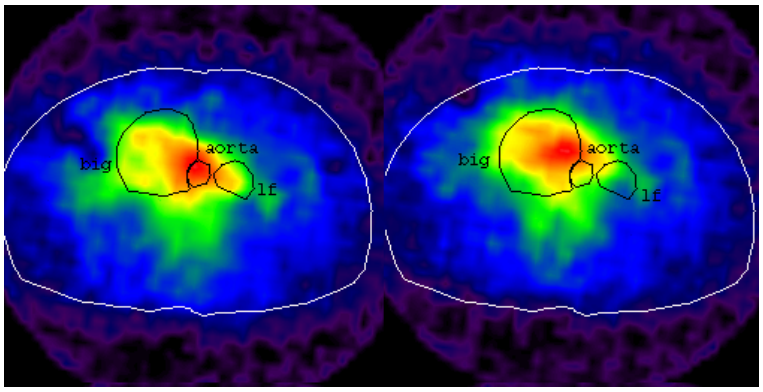

Figure 6.3: The net-count-maximization result for the patient with ID#7. Reconstructed SPECT slice corresponds to CT IM 43. left) Result for fusion that maximized counts in 2 abdominal tumors. right) Result for fusion that maximized counts in "big" which is unacceptable.

Figure 6.3 and Table 6.4 show the danger of accepting a fusion that maximizes the counts in a single tumor. The patient is the same as in Figure 6.2, but the SPECT slice is 2cm more towards the feet. The left of Figure 6.3 shows the result from the fusion that maximized the counts in the two abdominal tumors that was discussed above. The right

of Figure 6.3 shows the result from a fusion that maximized the counts in an individual tumor, namely “big”. In the left part of the figure, the outlines for “big,” “lf” and “aorta” appear reasonable. In the right part of the figure, the SPECT image seems to be shifted up and to the left compared to the VOI. The VOI for “big” gets more counts incorrectly by being placed partly over the aorta. So, the potential increase in counts of 31.7% listed in Table 6.4 probably represents an increase that isn’t consistent with reality and is a result that should not be accepted. The fact that the counts in the nearby tumor go down is added proof. Such a mixed result also occurred when the counts in the “lf” tumor was used as the basis of the maximization. This suggests that such a procedure should be used with care even when the search range from iteration to iteration is fairly small, since there are many failure modes by which the single tumor intensity can be over-estimated when its max counts is the sole criterion for the fusion.

When the “best” values as described above are used for all 14 tumors in all seven patients, the positive % change ranges from 0.0 to 26.7. There is one negative % change equal to -30%. The average value over the 13 tumors with positive changes is 9.47% and over all 14 tumors is 6.65%.

6.4 Discussion

We have chosen to maximize net counts in one or more tumors to carry out the inverse registration (from SPECT space into CT space) in the tests above. Another possibility would be to maximize net counts in one or more tumors combined with one or more organs, such as liver and kidney. Alternatively, one could choose to maximize the net percent increase in counts in the tumors involved. When there are at least two tumors with different count levels, this procedure would tend to prevent the high uptake tumor from dominating the registration. Another approach would be to use mutual information

as the criterion for the inverse transformation instead of the criteria we have investigated. If the tumor VOIs were present in the color-wash display (which is basically possible) it would be easier to choose a good inverse fusion. Still another approach would be to combine the max-counts criterion with the max-mutual-information criterion to produce a joint objective function. With such a joint objective function, a weighting factor relating the two parts of the objective function would have to be chosen. This variation might be more stable, but it is less straightforward because it is not clear what weight might be appropriate. In all cases, evaluating the results will probably require some subjective judgments.

The count-maximization approach has a problem when a single tumor lies immediately next to a highly active object, like the bladder. However, the algorithm can be used in the pelvis when there are tumors on opposite sides of bladder. Then, for example, a simple translation to the left increases counts in the tumor to the right of bladder, but at the same time decreases counts in the tumor to the left of the bladder, precluding such a translation.

CHAPTER VII

CONCLUSIONS AND FUTURE WORK

7.1 Conclusions

In this thesis, an isotropic random field model was developed for statistical shape modeling. This model regards radial functions of segmented polar objects as random fields over the unit sphere S^2 and characterizes the shape information by the mean and covariance functions of the random fields. It was proved that radial functions of 3D polar objects with uniformly distributed orientation are isotropic random fields over S^2. The covariance functions of isotropic random fields over the unit sphere can be orthogonally decomposed by spherical harmonics. Thus a Karhunen-Loéve expansion of the random field model was obtained. A test of the isotropic hypothesis was also proposed for randomly oriented 3D shapes. Segmentation data sets can be categorized as isotropic and non-isotropic according to the outcome of the test.

To link the accuracy of center estimation with the accuracy of shape modeling, we investigated the statistical properties of different center estimators. We established that the ellipsoid fitting method proposed by Bookstein is a maximum likelihood estimator of ellipsoid parameters when the segmentation noise level is low. A lower bound has been derived for the variance of ellipsoid fitting center estimator with Gaussian segmentation noise model. The simulated results show that the variance of the ellipsoid fitting center

estimator is much lower than that of linear average method.

Based on the spectral theory of random field, the proposed statistical shape model was applied to address two problems in this thesis. The first one was shape denoising: given noisy samples of surface boundary points, e.g. coarsely segmented from an object, find an optimal estimate of the true surface boundary. Using Wiener filter theory, an orthogonal representation of random fields was applied to solve this problem. The simulation results show that our optimal shape estimator has a much lower variance than the linear filtering result. To reduce the computational complexity of spherical harmonics, double Fourier series was introduced in place of spherical harmonics in the estimation procedure. The second problem was the 3-D object registration problem. In terms of group theory, spherical harmonics comprise an irreducible representation of $SO(3)$ rotation, which makes it possible to decompose the radial surface function into a direct sum of orthogonal subspaces which are globally invariant to rotation. With a Gaussian segmentation noise model, a maximum likelihood estimator was designed to register 3D objects in the frequency domain through joint estimation of spherical harmonic coefficients and Euler angles of 3D rotation. The novelty of this method lies on its use of the assumption that the noise field is isotropic and thus the decomposed noise coefficients are statistically independent. Since the 3D objects are registered in the frequency domain via low order spherical harmonic coefficients, the registration automatically filters out high frequency noise and has low computational complexity. This method may be very useful not only in medical image registration but also in shape-based retrieval of similar objects in image databases.

In Chapter V, a novel active contour was proposed to segment 3D objects. A spectral method using double Fourier series as orthogonal basis functions was applied to solve elliptic partial differential equations in the contour evolution. The computational complexity of the spectral method is $O(N^2 \log N)$ for a grid size of $N \times N$, which is lower than the

complexity of iterative methods, such as finite element method or finite difference method. A volumetric penalization term was introduced in the energy function of the active contour to prevent the contour from leaking at blurred boundaries. We applied the active contour to segment both medical images and synthesized images. Our results show that the new method preserves the merits of other parametric active contours and has a faster convergence rate. Due to the generality of our mathematical formulation, the spectral method can be easily applied to solve the surface reconstruction problem too.

In Chapter VI, we investigated how much the tumor activity estimate increases if a local optimization is performed to adjust the rigid CT-SPECT registration to maximize mean SPECT intensity within tumor VOI segmented from CT. The results show that the proposed algorithm can be effective in registering tumors in CT and SPECT locally. In particular, based on a study of 14 tumors in 7 patients, the increases in tumor counts average 6.65%. The max increases is 26.7%.

7.2 Future Work

7.2.1 Statistical Shape Modeling and Its Applications

In this thesis, we used scalar radial functions to represent star-shaped 3D surfaces. However, 3D biomedical shapes are not likely limited to this kind of topology. To overcome our shape model's limitation to star-shaped surface topology, a key step is to find a one-to-one map of any simply connected (no hole) surface $\mathbf{x}$ to the unit sphere S^2, i.e., $f : \mathbf{x} \rightarrow S^2$. The mapping must be continuous, i.e. neighboring points in one space must map to neighbors in the other space. It is desirable and possible to construct a map that preserves areas. However, it is not possible in general to map the whole surface without distortions. A good map should minimize the distortions. Therefore, the embedding of an arbitrary simply connected surface into the unit sphere S^2 is a constrained optimization

problem. We would like to modify the method proposed by Brechbühler to get the map [15]. The objective is to minimize the distortion of the surface net in the mapping. This will force the shape of all the mapped faces to be as similar to their original form as possible. For example, a square facet should map to a 'spherical square'. This can in general not be reached for all patches, and we will need to achieve a trade off between the distortions made at different vertices. The measure of distortion can be designed according to the requirements of applications.

We have applied our statistical shape model to shape denoising and orientation estimation. We want to further investigate whether the random field model could be applied to more general problems in pattern recognition. An example of a pattern recognition system relevant to medical imaging is the storage and retrieval of different biomedical organs in medical databases. We have discussed the Fourier descriptors to represent 3D biomedical organs in this thesis. Their coefficients comprise a pattern vector which represents the distinctive features of an organ's shape. If the number of feature is large, the computational requirements for correct classification (retrieval of organs) of given shape or morphology become significant. If mean square error measure is a good measure of segmentation error, the Karhunen-Loéve expansion of random field can be applied to achieve compression of the pattern vector. Let $X(\theta, \phi)$ represent the random field model of the 3D organ. Its K-L expansion can be represented by:

$$X(\theta, \phi) = \sum_{i=0}^{\infty} c_i b_i(\theta, \phi)$$

where $b_i(\theta, \phi)$ are orthonormal basis functions defined over S^2 and the coefficients c_i are random variables given by $c_i = \int_{S^2} X(\theta, \phi) b_i(\theta, \phi) d\Omega_{S^2}$. We want to seek a representation $\hat{X}(\theta, \phi)$ expanded by finite number of basis functions n which can minimize the mean-square error $E\{|\hat{X}(\theta, \phi) - X(\theta, \phi)|^2\}$. Since the mean square error of the repre-

sentation equals the sum of the coefficients corresponding to the basis functions not used in the representation, the optimum off-line technique is to order c_i in descending order of magnitude and retain only the first n coefficients.

To build databases of medical organs, we can obtain random field models for each VOI, such as liver, kidney, spleen, etc., through segmentation of a large training set of images. After computing the Karhunen-Loéve expansions of these shapes in the training set, we can apply feature selection procedure discussed above. To compare a segmented organ to others in the database, its noisy pattern vector can be correlated with the pattern vectors stored in the database. The decision boundaries that separate the organ patterns can be determined in advance.

7.2.2 Image Segmentation by Parametric Active Contours

7.2.2.1 Non-Smooth Evolution via Semi-Quadratic Programming

In the 3D active contours method, the parameter α in the Lagrangian (5.10) $E(f) = \int_{S^2} \alpha \|\nabla f\|^2 + (f - g_f)^2 d\Omega_{S^2}$ controls the tradeoff between denoising and matching high spatial frequencies. In the current implementation of the active contour, α is a constant chosen in advance and the value of α is fixed during the contour evolution. However, it is desirable that α is a function of the contour and can be modified in the evolution so that non-smooth solutions are allowed to accommodate singularities.

The idea of using semi-quadratic programming for image segmentation was proposed by Charbonnier in [24]. Following this idea for our 3D active contour, we would replace the term $\|\nabla f\|^2$ in the Lagrangian with a smooth total variation type of norm which behaves like the $\|\nabla f\| = |\frac{1}{\sin\theta}\frac{df}{d\phi}| + |\frac{df}{d\theta}|$. It is well known that such weaker smoothness "constraints" allow non-smoothness solutions. The Lagrangian (5.10) would then take the

modified form:

$$E(f) = \int_{S^2} Q(\|\nabla f\|) + (f - g_f)^2 d\Omega_{S^2} \tag{7.1}$$

where $Q(y)$ is a sublinear function. Since $Q(y)$ is non-linear in f, the idea of semi-quadratic programming is to use the "conditionally quadratic" representation

$$Q(y) = \min_b \{by^2 + \Psi(b)\} \tag{7.2}$$

where the minimizer $b(y)$ is analytical: $b(y) = \frac{dQ(y)/dy}{2y}$. This representation suggests minimizing the quadratic Lagrangian

$$E(f) = \int_{S^2} b(\|\nabla f\|)\|\nabla f\|^2 + (f - g_f)^2 d\Omega_{S^2}. \tag{7.3}$$

where $b(\|\nabla f\|)$ is the minimizer of $Q(\|\nabla f\|)$. For example, if we select $Q(y) = \frac{y^2}{1-y^2}$, this yields $b(\|\nabla f\|) = \frac{1}{(1+\|\nabla f\|)^2}$. Notice that the Lagrangian (7.3) no longer generates a Helmholtz type Euler-Lagrange condition. It might therefore be better to use FEM/FDM methods to solve the new partial differential equation.

7.2.2.2 Hybrid Spline-Fourier Descriptors

As mentioned above and in Chapter V, Fourier descriptors have difficulties in fitting sharp corners due to the high spatial frequency components there. Here we describe a hybrid spline-Fourier descriptor approach that is under development.

Multivariate spline models are well known for their capability of efficiently handling local deformations. Using a spline representation, a contour can be split into segments. Each segment is defined by a few control points (node points or knots). Altering the position of control points only locally modifies the curve or surface without affecting other portions. Local control makes it possible to track local shape deformation using a small number of parameters, unlike Fourier descriptors which require many parameters and can have spurious oscillations.

We want to combine the local deformational capability of splines with Fourier descriptors to cover diverse shapes. The following hybrid spline-Fourier descriptors is proposed. First, a Fourier descriptor is applied to estimate the global low frequency parameters of the shape. Then, splines are used to refine the contour at necessary local places. Similar ideas can be implemented to evolve active contours, i.e., after the Fourier descriptor active contour roughly converges to the object boundary, a few spline active contours can be added to the existing contour to fit some singular points on the boundary. This new deformable model is expected to be able to deform both globally like the Fourier contours and locally like spline approximations.

7.2.2.3 Relation With Geometric Active Contours

Since both the parametric and geometric active contour methods have been widely studied in the last few years, the relation between them has recently become a research focus [4, 109]. Both parametric active contour methods and geometric active contour methods involve optimization problems. The parametric active contours are driven by minimizing its associated energy functional, while the geometric active contours are driven by finding the path of minimal length or areas. It is shown in [4] that the two minimization problems are equivalent if the direction which locally most decreases one of the criterion is also a decreasing direction for the other criterion and vice versa.

We are motivated by the preliminary results of the relation between these two active contours. Further exploration in this direction, especially in the fast algorithm to solve PDE's derived from these two problems, is of great interest to us.

APPENDICES

APPENDIX A

Spherical Harmonics

A.1 Spherical Harmonics

A.1.1 Definition of Spherical Harmonics

The *spherical harmonics* $Y_l^m(\theta, \phi)$ are the angular portion of the solution to the Laplace equation in spherical coordinates where azimuthal symmetry is not present.

The Laplace equation in the Cartesian coordinates system is

$$\nabla^2 \varphi = 0. \tag{A.1}$$

In the spherical coordinates system, Laplace equation is written as

$$\frac{\partial}{\partial r}(r^2 \frac{\partial \varphi}{\partial r}) + \frac{1}{\sin\theta}\frac{\partial}{\partial \theta}(\sin\theta \frac{\partial \varphi}{\partial \theta}) + \frac{1}{\sin^2\theta}\frac{\partial^2 \varphi}{\partial^2 \phi} = 0. \tag{A.2}$$

The angular portion of its solution, which is called the *spherical harmonics*, can be written as

$$Y_l^m(\theta, \phi) = (-1)^m \sqrt{\frac{2l+1}{4\pi}\frac{(l-m)!}{(l+m)!}} P_l^m(\cos\theta) e^{im\phi} \tag{A.3}$$

where θ is the polar angle, ϕ is the azimuthal angle, $P_l^m(x)$ is the associated Legendre function (see A.2), $l \geq 0$, $-l \leq m \leq l$, and the normalization is chosen such that

$$\int_0^{2\pi} \int_0^{\pi} Y_l^m(\theta, \phi) Y_{l'}^{m'*}(\theta, \phi) \sin\theta d\theta d\phi = \delta_{m,m'}\delta_{l,l'} \tag{A.4}$$

where Y^* is the complex conjugate of Y and $\delta_{m,m'}$ is the Kronecker delta function. By the property of the associated Legendre function, it is easy to derive the relation that

$$Y_l^{m*}(\theta,\phi) = (-1)^m Y_l^{-m}. \tag{A.5}$$

Figure A.1 [1] plots some of the spherical harmonics.

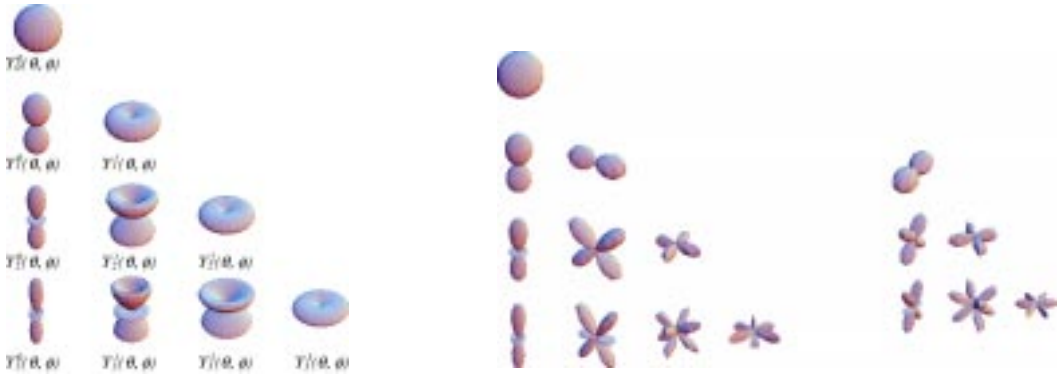

(a) (b)

Figure A.1: Spherical harmonics. (a) $|Y_l^m(\theta,\phi)|$, (b) $\Re[Y_l^m(\theta,\phi)]$ and $\Im[Y_l^m(\theta,\phi)]$.

A.1.2 Completeness of Spherical Harmonics

Spherical harmonics are orthonormal as can be seen from (A.4). The function set $\{Y_l^m(\theta,\phi)\}$, $l \geq 0$, $|m| \leq l$, is complete. It is well known that the function set $\{e^{im\phi}\}$, where m is an integer, is complete. Its elements satisfies

$$\int_0^{2\pi} e^{-im\phi}\, e^{im'\phi}\, d\phi = 2\pi\delta_{m,m'}. \tag{A.6}$$

The function set $\{P_l^m(\cos\theta)\}$, m fixed and $l \geq |m|$, is also complete [Appendix B]. The completeness of the set $Y_l^m(\theta,\phi)$, $l \geq 0$, $|m| \leq l$, can be proved using the following theorem.

[1] These figures were copied from the website http://mathworld.wolfram.com.

Theorem 7 *Let* $\{\varphi_n(s)\}$ $(n = 1, 2, \cdots)$ *be a complete set of orthonormal functions on* $[a, b]$. *If for any* n, *there exists a complete set* $\psi_{mn}(t)\}$ $(m = 1, 2, \cdots)$ *of orthonormal functions on* $t \in [c, d]$. *Then*

$$\omega_{mn}(s,t) = \varphi_n(s)\psi_{mn}(t) \qquad (m, n = 1, 2, \cdots) \tag{A.7}$$

is complete set of orthonormal functions on $\{(s,t)|a \leq s \leq b, c \leq t \leq d\}$, *such that for any continuous function* $f(s,t)$ *on* $\{(s,t)|a \leq s \leq b, c \leq t \leq d\}$, *the following is true*

$$\int\int |f(s,t)|^2 ds\, dt = \sum_{m,n=1}^{\infty} |\int\int \omega^*_{mn}(s,t) f(s,t) ds\, dt|^2. \tag{A.8}$$

A.1.3 Addition Theorem

Theorem 8 (Spherical Harmonic Addition Theorem) *Let* (θ_1, ϕ_1) *and* (θ_2, ϕ_2) *denote two different directions separated by the angle* γ *in the spherical coordinate system, as shown in Figure 2.12. These angles satisfy the trigonometric identity, i.e.,*

$$\cos\gamma = \cos\theta_1 \cos\theta_2 + \sin\theta_1 \sin\theta_2 \cos(\phi_1 - \phi_2). \tag{A.9}$$

The addition theorem asserts that

$$P_l(\cos\gamma) = \frac{4\pi}{2l+1} \sum_{m=-l}^{l} Y_l^m(\theta_1, \phi_1) Y_l^{m*}(\theta_2, \phi_2). \tag{A.10}$$

A.2 Legendre Polynomial and Associated Legendre Function

A.2.1 Legendre Polynomial

The Legendre polynomial of the degree l is defined as [59]

$$P_l(x) = 2^{-l} \sum_{r=0}^{[\frac{l}{2}]} (-1)^r \frac{(2l-2r)!}{r!(l-r)!(l-2r)!} x^{l-2r} \tag{A.11}$$

where $[\frac{l}{2}] = \frac{l}{2}$ if l even, or $[\frac{l}{2}] = \frac{l-1}{2}$ when l odd. The Legendre polynomial is the solution to the Legendre equation, which is

$$(1-x^2)\frac{d^2y}{dx^2} - 2x\frac{dy}{dx} + l(l+1)y = 0 \tag{A.12}$$

where l is an integer, $l \in [0, \infty)$.

The Legendre polynomials are orthogonal, i.e.,

$$\int_{-1}^{1} P_m(x) P_n(x) dx = \frac{2}{2n+1} \delta_{mn} \tag{A.13}$$

where δ_{mn} is the Kronecker delta function.

The set $\{P_l(x)\}$ of Legendre polynomials is complete [59]. Any function $f(x)$ satisfying

$$\int_{-1}^{1} |f(x)|^2 dx < \infty \tag{A.14}$$

can be expanded by its *Legendre series*, i.e.,

$$f(x) = \sum_{l=0}^{\infty} a_l P_l(x) \tag{A.15}$$

where

$$a_l = \frac{2l+1}{2} \int_{-1}^{1} f(x) P_l(x) dx. \tag{A.16}$$

The right hand side of (A.15) is called the *Legendre series* of the function $f(x)$ and converges uniformly on $[-1, 1]$ [59].

A.2.2 Associated Legendre Function

The associated Legendre function $P_l^m(x)$ is defined as [59]

$$P_l^m(x) = (-1)^m \frac{(1-x^2)^{\frac{m}{2}}}{2^l l!} \frac{d^{l+m}}{dx^{l+m}} (x^2-1)^l \tag{A.17}$$

where l is an integer, $l \in [0, \infty)$, m is also an integer, $|m| \leq l$, and x is a real number in $[-1, 1]$.

The associated Legendre function $P_l^m(x)$ can also be written as

$$P_l^m(x) = (-1)^m (1-x^2)^{\frac{m}{2}} \frac{d^m}{dx^m} P_l(x) \tag{A.18}$$

for $l \geq m \geq 0$, where $P_l(x)$ is the Legendre polynomial of the degree l. For $-l \leq m < 0$, the functions can be obtained from

$$P_l^{-m}(x) = (-1)^m \frac{(l-m)!}{(l+m)!} P_l^m(x). \tag{A.19}$$

The associated Legendre functions have the following orthogonal relationship:

$$\int_{-1}^{1} P_l^m(x) P_{l'}^m(x) dx = \frac{2}{2l+1} \frac{(l+m)!}{(l-m)!} \delta_{ll'} \tag{A.20}$$

and

$$\int_{-1}^{1} P_l^m(x) P_l^{m'}(x) \frac{dx}{1-x^2} = \frac{1}{m} \frac{(l+m)!}{(l-m)!} \delta_{mm'}. \tag{A.21}$$

where $m, m' \geq 0$.

It can be shown that

$$\int_{-1}^{1} P_l^m(x) P_{l'}^{-m}(x) dx = (-1)^m \frac{2}{2l+1} \delta_{ll'} \tag{A.22}$$

and

$$\int_{-1}^{1} P_l^m(x) P_l^{-m'}(x) \frac{dx}{1-x^2} = \frac{(-1)^m}{m} \delta_{mm'}. \tag{A.23}$$

For fixed m,$\{P_l^m(x)\}$ $(l \geq m)$ is a complete set of orthogonal functions on $[-1, 1]$. Any function $f(x)$, which is continuous on $[-1, 1]$ and has $f(-1) = f(1) = 0$, can be

expanded by the associated Legendre functions of any order m in the sense of uniform convergence as the following

$$f(x) = \sum_{l \geq m} a_l P_l^m(x) \tag{A.24}$$

where

$$a_l = \frac{2l+1}{2} \frac{(l-m)!}{(l+m)!} \int_{-1}^{1} f(x) P_l^m(x) dx. \tag{A.25}$$

APPENDIX B

Statistics of Surface Function Extracted By Edge Filtering

This section shows that a 3D surface function extracted by edge filtering can be regarded as an isotropic random field on unit sphere.

Let the edge model to be step edges. In one dimension, it is the following [42]:

$$e(x) \;=\; AY(x) \;+\; n(x) \tag{B.1}$$

where A is the contrast given by $C_{ROI} - C_{BG}$, $Y(x)$ is the step function defined as

$$Y(x) = \begin{cases} 1 & x > 0, \\ 0 & x \leq 0, \end{cases}$$

and $n(x)$ is a stationary white noise process with zero mean and variance σ_0^2.

Let $h(x)$ to be the unknown edge filter to convolve with $e(x)$, and $o(x)$ the output signal. Since we want to detect edges as extrema in the output, $h(x)$ must be "derivation" operator and therefore odd. Also we assume $h(x)$ is nonzero only in an interval $[-W, W]$. Then

$$o(x) = \int_{-\infty}^{\infty} e(x-y)h(y)d\,y \;=\; A \cdot \int_{-\infty}^{x} h(y)d\,y + \int_{-\infty}^{\infty} n(x-y)h(y)d\,y \tag{B.2}$$

Let x_0 denotes the random variables which is defined as the amount of displacement of the position of the maximum in the output $o(x)$ with respect to the true position $x = 0$ of the

edge. The random variable x_0 depends on both the edge and the noise. A maximum in the output $o(x)$ corresponds to $o'(x_0) = 0$. We can compute $o'(x)$ as following:

$$\begin{aligned} o'(x) &= \frac{d}{dx}\int_{-\infty}^{\infty} e(x-y)h(y)d\,y \\ &= A\cdot\int_{-\infty}^{\infty} Y(x-y)h'(y)d\,y + \int_{-\infty}^{\infty} n(x-y)h'(y)d\,y \\ &= A\cdot h(x) + \int_{-\infty}^{\infty} n(x-y)h'(y)d\,y \\ &= S(x) + N(x) \end{aligned} \tag{B.3}$$

where $S(x)$ denotes $A\cdot h(x)$ as the signal part and $N(x)$ denotes $\int_{-\infty}^{\infty} n(x-y)h'(y)d\,y$ as the noise part. From the assumption of our noise model, we know that $N(x)$ is a Gaussian random variable such that $E[N(x)] = 0$ and

$$E[N(x)^2] \;=\; \sigma_0^2\int_{-\infty}^{\infty} h'^2(y)d\,y$$

Assuming that x_0 is close to 0, $S(x_0)$ can be approximated up to the second order, as

$$S(x_0) \;\simeq\; A\cdot h(0) \;+\; x_0\cdot Ah'(0) \;=\; x_0\cdot Ah'(0) \tag{B.4}$$

Note that $h(x)$ is odd so that $h(0) = 0$. Since x_0 satisfies $o'(x_0) = 0$, we can write

$$o'(x_0) \;=\; S(x_0) + N(x_0) \;\simeq\; x_0\cdot Ah'(0) + N(x_0) = \;0 \tag{B.5}$$

Therefore

$$x_0 \;\simeq\; -\frac{N(x_0)}{Ah'(0)} \tag{B.6}$$

So x_0 can be regarded as a Gaussian random variable with zero mean and it's variance is given by

$$E(x_0^2) \;=\; \frac{\sigma_0^2}{A^2}\cdot\frac{\int_{-\infty}^{\infty} h'^2(y)d\,y}{h'^2(0)} \tag{B.7}$$

From the above derivation, we can see that the displacement of the edge position is a Gaussian random variable in the one dimension edge detection. If we regard the 3D

surface function $R(\theta, \phi)$ is obtained by one dimension edge detection along each sampling direction (θ, ϕ) and assume the surface curvature does not influent the detection, we can say that $R(\theta, \phi)$ is a Gaussian random field on the unit sphere. In the continuous case, noise in different directions are uncorrelated, the covariance of $R(\theta, \phi)$ can be written as

$$\psi(\cos\gamma) \;=\; E(x_0^2)\delta(\gamma) \tag{B.8}$$

where $\delta(\gamma)$ is the delta function.

In the discrete case, $\psi(\cos\gamma)$ is not equal to zero at small value of γ. This is because many common voxels intensity values could be used for the edge detections of two directions very close to each other. Ignoring the geometry of the object, it can be assumed $\psi(\cos\gamma)$ is isotropic. The larger the object size (relative to the voxel size) is, the quicker the value of $\psi(\cos\gamma)$ decreases to zero as γ increases.

APPENDIX C

Derivation of Euler-Lagrange Equation

In this section, we provide a detailed derivation of the associated Euler-Lagrange equation (5.3) for the energy functional (5.2).

Let S^2 denote the unit sphere and $g(\theta, \phi)$ be a scalar function defined over S^2. The energy functional is

$$E(f) = \int_{S^2} \mu(f(\theta,\phi) - g(\theta,\phi))^2 d\Omega + \int_{S^2} \|\nabla f(\theta,\phi)\|^2 d\Omega \tag{C.1}$$

In spherical coordinates system, the gradient is

$$\nabla = \frac{\partial}{\partial r}\hat{r} + \frac{1}{r}\frac{\partial}{\partial \theta}\hat{\theta} + \frac{1}{r\sin\theta}\frac{\partial}{\partial \phi}\hat{\phi}. \tag{C.2}$$

And on the unit sphere, it reduces to

$$\nabla = \frac{\partial}{\partial \theta}\hat{\theta} + \frac{1}{\sin\theta}\frac{\partial}{\partial \phi}\hat{\phi}. \tag{C.3}$$

So the equation (C.1) can be rewritten as:

$$\begin{aligned} E(f) &= \int_{\theta=0}^{\pi}\int_{\phi=0}^{2\pi} [(\frac{\partial f}{\partial \theta})^2 + \frac{1}{\sin^2\theta}(\frac{\partial f}{\partial \phi})^2 + \mu(f-g)^2]\sin\theta d\theta d\phi \\ &= \int_{\theta=0}^{\pi}\int_{\phi=0}^{2\pi} F(f, \frac{\partial f}{\partial \theta}, \frac{\partial f}{\partial \phi}) d\theta d\phi \end{aligned} \tag{C.4}$$

where $F(f, \frac{\partial f}{\partial \theta}, \frac{\partial f}{\partial \phi}) = [(\frac{\partial f}{\partial \theta})^2 + \frac{1}{\sin^2\theta}(\frac{\partial f}{\partial \phi})^2 + \mu(f-g)^2]\sin\theta$. We will denote $\frac{\partial f}{\partial \theta}$ and $\frac{\partial f}{\partial \phi}$ by f_θ and f_ϕ from now on. From calculus of variations [32], we know that functional

E is stationary if and only if its first variation δE vanishes. We introduce an arbitrary function $\eta(\theta, \phi)$, which possesses a continuous second derivative and vanishes outside the boundary. Let ϵ be a parameter,

$$\delta E = \epsilon \left. \frac{d}{d\epsilon} E(f + \epsilon\eta) \right|_{\epsilon=0} \tag{C.5}$$

This is equivalent to equation

$$\delta E = \epsilon \int_{\theta=0}^{\pi} \int_{\phi=0}^{2\pi} (F_f \eta + F_{f_\theta} \eta_\theta + F_{f_\phi} \eta_\phi) d\theta d\phi \tag{C.6}$$

By Gauss's integral theorem and imposing the condition $\eta = 0$ on the boundary, we obtain

$$\delta E = \epsilon \int_{\theta=0}^{\pi} \int_{\phi=0}^{2\pi} \eta \left\{ F_f - \frac{\partial}{\partial\theta} F_{f_\theta} - \frac{\partial}{\partial\phi} F_{f_\phi} \right\} d\theta d\phi \tag{C.7}$$

The equation $\delta E = 0$ must be valid for any arbitrary continuously differentiable function η. Therefore we can conclude $f(\theta, \phi)$ must satisfy the Euler-Lagrange differential equation

$$F_f - \frac{\partial}{\partial\theta} F_{f_\theta} - \frac{\partial}{\partial\phi} F_{f_\phi} = 0 \tag{C.8}$$

Substitution of $F(f, f_\theta, f_\phi) = [(\frac{\partial f}{\partial\theta})^2 + \frac{1}{\sin^2\theta}(\frac{\partial f}{\partial\phi})^2 + \mu(f-g)^2] \sin\theta$ into equation (C.8) yields

$$\begin{aligned}
& F_f - \frac{\partial}{\partial\theta} F_{f_\theta} - \frac{\partial}{\partial\phi} F_{f_\phi} \\
= \;& 2\mu \sin\theta (f-g) - 2\frac{\partial}{\partial\theta}(\sin\theta \frac{\partial f}{\partial\theta}) - 2\frac{1}{\sin\theta}\frac{\partial^2 f}{\partial\phi^2} \\
= \;& 2\sin\theta \left[\mu(f-g) - \frac{1}{\sin\theta}\frac{\partial}{\partial\theta}(\sin\theta\frac{\partial f}{\partial\theta}) - \frac{1}{\sin^2\theta}\frac{\partial^2 f}{\partial\phi^2} \right] \\
= \;& 2\sin\theta \left[\mu(f-g) - \nabla^2 f \right] \\
= \;& 0
\end{aligned} \tag{C.9}$$

And this gives out the Euler-Lagrange equation (5.3),

$$\nabla^2 f - \mu(f-g) = 0 \tag{C.10}$$

BIBLIOGRAPHY

BIBLIOGRAPHY

[1] R. J. Adler, *The Geometry of Random Fields*, Wiley, 1981.

[2] A. Albano, "Representation of digitized contours in terms of conic arcs and straight-line segments," *Computer Graphics and Image Processing*, vol. 3, , 1974.

[3] G. B. Arfken, *Mathematical Methods For Physicists*, Academic Press, Orlando, 3 edition, 1985.

[4] G. Aubert and L. Blanc-Féraud, "Some remarks on the equivalence between 2D and 3D classical snakes and geodesic active contours," *International Journal of Computer Vision*, vol. 34, no. 1, pp. 19–28, 1999.

[5] N. Ayache, P. Cinquin, I. Cohen, L. Cohen, F. Leitner, and O. Monga, "Segmentation of complex three-dimensional medical objects: a challenge and a requirement for computer-assisted surgery planning and performance," in *Computer-Integrated Surgery: Technology and Clinical Applications*, pp. 59–74, MIT Press, 1996.

[6] L. Bers, F. John, and M. Schechiter, *Partial Differential Equations*, John Wiley and Sons, 1964.

[7] J. A. K. Blokland, A. M. Vossepoel, A. R. Bakker, and E. K. J. Paulwels, "Delineating elliptical objects with an application to cardiac scintigrams," *IEEE Transactions on Medical Imaging*, vol. 6, no. 1, pp. 57–66, 1987.

[8] G. J. Boer and L. Steinberg, "Fourier series on sphere," *Atmosphere*, vol. 13, pp. 180, 1975.

[9] R. M. Bolle and B. C. Vemuri, "On three-dimensional surface reconstruction methods," *IEEE Trans. on Pattern Analysis and Machine Intelligence*, vol. 13, no. 1, pp. 1–13, Jan. 1991.

[10] G. Bonneau, "Multiresolution analysis on irregular surface meshes," *IEEE Trans. on Visualization and Computer Graphics*, vol. 4, no. 4, pp. 365–378, 1998.

[11] F. L. Bookstein, "Fitting conic sections to scattered data," *Computer Graphics and Image Processing*, vol. 9, pp. 56–71, 1979.

[12] N. A. Borghese and S. Ferrari, "A portable modular system for automatic acquisition of 3-D objects," *IEEE Trans. on Instrumentation and Measurement*, vol. 49, no. 5, pp. 1128–1136, Oct. 2000.

[13] J. P. Boyd, "The choice of spectral functions on a sphere for boundary and eigenvalue problems: A comparison of Chebyshev, Fourier and associated Legendre expansions," *Monthly Weather Review*, vol. 106, pp. 1184–1191, Aug. 1978.

[14] J. P. Boyd, *Chebyshev and Fourier Spectral Methods*, Springer-Verlag, New York, 1989.

[15] C. Brechbühler, G. Gerig, and O. Kübler, "Parametrization of closed surfaces for 3-D shape description," *Computer Vision and Image Understanding*, vol. 61, no. 2, pp. 154–170, March 1995.

[16] Y. Bresler and A. Macovski, "Three-dimensional reconstruction from projections with incomplete and noisy data by object estimation," *IEEE Transactions on Acoustics Speech Signal Processing*, vol. 35, pp. 1139–1152, 1987.

[17] L. G. Brown, "A survey of image registration techniques," *ACM Computing Surveys*, vol. 24, no. 4, pp. 325–376, Dec. 1992.

[18] L. G. Brown, G. Q. Maguire, and M. E. Noz, "Landmark-based 3D fusion of SPECT and CT images," in *Proceedings of the SPIE, Sensor Fusion VI*, volume 2059, pp. 166–174, 1993.

[19] G. Burel, "Three-dimensional invariants and their application to object recognition," *Signal Processing*, vol. 45, pp. 1–22, 1995.

[20] G. Burel and H. Henocq, "Determination of the orientation of 3D objects using spherical harmonics," *Graphical Models and Image Processing*, vol. 57, no. 5, pp. 400–408, 1995.

[21] V. Caselles, F. Catte, T. Coll, and F. Dibos, "A geometric model for active contours," *Numerische Mathematik*, vol. 66, pp. 1–31, 1993.

[22] V. Caselles, R. Kimmel, and G. Sapiro, "Geodesic active contours," *International Journal of Computer Vision*, vol. 22, no. 1, pp. 61–79, 1997.

[23] T. F. Chan and L. A. Vese, "Active contours without edges," *IEEE Trans. on Image Processing*, vol. 10, no. 2, pp. 266–277, Feb. 2001.

[24] P. Charbonnier, L. Blanc-Féraud, A. G., and B. M., "Deterministic edge-preserving regularization in computed imaging," *IEEE Transactions on Image Processing*, vol. 6, no. 2, pp. 298–311, Feb. 1997.

[25] H. Cheong, "Double Fourier series on a sphere: Applications to elliptic and vorticity equations," *Journal of Computational Physics*, vol. 157, no. 1, pp. 327–349, January 2000.

[26] I. Cohen and L. D. Cohen, "Hyperquadric model for 2D and 3D data fitting," in *Proceedings of the 12th IAPR International. Conference on Pattern Recognition*, volume 2, pp. 403–405, 1994.

[27] L. D. Cohen and I. Cohen, "Finite-element methods for active contour models and balloons for 2-D and 3-D images," *IEEE Transactions on Pattern Analysis and Machine Intelligence*, vol. 15, no. 11, pp. 1131–1147, 1993.

[28] A. Collignon, F. Maes, D. Delaere, D. Vandermeulen, P. Suetens, and G. Marchal, *Information Processing in Medical Imaging*, chapter Automated Multi-modality Image Registration Based On Information Theory, pp. 263–274, Kluwer Academic, Dordrecht, 1995.

[29] D. R. Cooper and N. Yalabik, "On the computational cost of approximating and recognizing noise-perturbed straight lines and quadratic arcs in the plane," *IEEE Trans. on Computers*, vol. 25, , 1976.

[30] T. F. Cootes, C. J. Taylor, D. H. Cooper, and J. Graham, "Active shape models - their training and application," *Computer Vision and Image Understanding*, vol. 61, no. 1, pp. 38–59, Jan. 1995.

[31] S. Cormier, N. Boujemaa, F. Tranquart, and L. Pourcelot, "Multimodal brain images registration with severe pathological information missing," in *Proceedings of the First Joint BMES/EMBS Conference*, volume 2, pp. 13–16, Oct. 1999.

[32] R. Courant and D. Hilbert, *Methods of Mathematical Physics*, Interscience, 1953.

[33] C. A. Davatzikos and J. L. Prince, "An active contour model for mapping the cortex," *IEEE Trans. on Medical Imaging*, vol. 14, pp. 65–80, 1995.

[34] D. DeCarlo and D. Metaxas, "Blended deformable models," *IEEE Transactions on Pattern Analysis and Machine Intelligence*, vol. 18, no. 4, pp. 443–448, April 1996.

[35] D. DeCarlo and D. Metaxas, "Shape evolution with structural and topological changes using blending," *IEEE Transactions on Pattern Analysis and Machine Intelligence*, vol. 20, no. 11, pp. 1186–1205, Nov. 1998.

[36] H. Delingette and J. Montagnat, "Topology and shape constraints on parametric active contours," Technical report, INRIA, France, 2000.

[37] P. Diaconis and D. Rockmore, "Efficient computation of the Fourier transform on finite groups," *Journal of the American Mathematical Society*, vol. 3, no. 2, pp. 297–332, 1990.

[38] P. C. Doerschuk and J. E. Johnson, "Ab inito reconstruction and experimental design for cryo electron microscopy," *IEEE Trans. on Information Theory*, vol. 46, no. 5, pp. 1714–1729, Aug. 2000.

[39] J. R. Driscoll and D. M. Healy, "Computing Fourier transform and convolutions on the 2-sphere," *Advances in Applied Mathematics*, vol. 15, pp. 202–250, 1994.

[40] K. B. Eom, "Long-correlation image models for textures with circular and elliptical correlation structures," *IEEE Trans. on Image Processing*, vol. 10, no. 7, pp. 1047–1055, July 2001.

[41] S. Erturk and T. J. Dennis, "3D model representation using spherical harmonics," *Electronics Letters*, vol. 33, no. 11, pp. 951–952, May 1997.

[42] O. Faugeras, *Three-Dimensional Computer Vision*, MIT Press, 1993.

[43] J. A. Fessler and A. O. Hero, "Penalized maximum-likelihood image reconstruction using space-alternating generalized em algorithms," *IEEE Trans. on Image Processing*, vol. 4, no. 10, pp. 1417–29, 1995.

[44] J. A. Fessler and A. Macovski, "Object-based 3-D reconstruction of arterial trees from magnetic resonance angiograms," *IEEE Transactions on Medical Imaging*, vol. 10, no. 1, pp. 25–39, March 1991.

[45] A. F. Frangi, D. Rueckert, J. A. Schnabel, and W. J. Niessen, "Automatic 3D ASM construction via atlas-based landmarking and volumetirc elastic registration," in *Proceedings of 17th International Conference of Information Processing in Medical Imaging*, M. F. Insana and R. M. Leahy, editors, pp. 78–91, Davis, CA, USA, June 2001, Springer-Verlag.

[46] P. Funk *Math. Ann.*, vol. 77, pp. 136–152, 1916.

[47] C. Giertsen, "Volume visualization of sparse irregular meshes," *IEEE Computer Graphics and Applications*, vol. 12, no. 2, pp. 40–48, Mar. 1992.

[48] R. Gnanadesikan, *Methods for Statistical Data Analysis of Multivariate Observations*, Wiley, New York, 1977.

[49] A. Goshtasby, "Image registration by local approximation methods," *Image and Vision Computing*, vol. 6, no. 4, pp. 255–261, Nov. 1988.

[50] D. Gottlieb and S. A. Orszag, *Numerical Analysis of Spectral Methods: Theory and Applications*, Society for Industrial and Applied Mathematics, Philadelphia, 1977.

[51] A. Gray, *Modern Differential Geometry of Curves and Surfaces with MATHEMATICA*, CRC Press, second edition, 1998.

[52] A. Gupta, T. O'Donnell, and A. Singh, "Segmentation and tracking of cine cardiac MR and CT images using a 3-D deformable models," in *Proceedings of IEEE Conference on Computers in Cardiology*, 1994.

[53] P. Haigron, G. Lefaix, X. Riot, and R. Collorec, "Application of spherical harmonics to the modelling of anatomical shapes," *Journal of Computing and Information Technology*, vol. 6, no. 4, pp. 449–461, December 1998.

[54] S. Han, D. B. Goldgof, and K. W. Bowyer, "Using hyperquadrics for shape recovery from range data," in *IEEE Proceedings. Fourth International Conference on Computer Vision*, pp. 492–496, 1993.

[55] D. M. Healy, D. N. Rockmore, and S. B. Moore, "An FFT for the 2-sphere and applications," in *Proceedings of International Conference on Acoustics, Speech, and Signal Processing, 1996.ICASSP-96*, volume 3, pp. 1323–1326, Atlanta, GA, May 1996.

[56] E. Hecke *Math. Ann*, vol. 78, pp. 398–404, 1918.

[57] D. R. Hernández, *Lectures on Probability and Second Order Random Fields*, World Scientific, 1995.

[58] C. T. Ho and L. H. Chen, "A fast ellipse/circle detector using geometric symmetry," *Pattern Recognition*, vol. 28, no. 1, pp. 117–124, 1995.

[59] E. W. Hobson, *The Theory of Spherical and Ellipsoidal Harmonics*, Cambridge, 1931.

[60] R. J. Jaszczak, "Tomographic radiopharmaceutical imaging," *Proceedings of the IEEE*, vol. 76, no. 9, pp. 1079–94, 1988.

[61] S. Jehan-Besson, M. Barlaud, and G. Aubert, "Video object segmentation using Eulerian region-based active contours," in *Proceedings Eighth IEEE International Conference on Computer Vision*, volume 1, pp. 353–60, Vancouver, BC, Canada, July 2001.

[62] K. Kanatani, "Analysis of 3-D rotation fitting," *IEEE Transactions on Pattern Analysis and Machine Intelligence*, vol. 16, pp. 543–549, 1994.

[63] M. Kass, A. Witkin, and D. Terzopoulos, "Snakes: Active contour models," *International Journal of Computer Vision*, vol. 1, no. 4, pp. 321–331, 1987.

[64] T. Kayikcioglu, A. Gangal, and M. Ozer, "Reconstructing ellipsoids from three projection contours," *Pattern Recognition Letters*, vol. 21, pp. 959–968, 2000.

[65] V. S. Khoo, D. P. Dearnaley, D. J. Finnigan, A. Padhani, S. F. Tanner, and M. O. Leach, "Magnetic resonance imaging (MRI): considerations and applications in radiotherapy treatment planning," *Radiotherapy and Oncology*, vol. 42, no. 1, pp. 1–15, 1997.

[66] B. B. Kimia, A. R. Tannenbaum, and S. W. Zucker, "Shapes, shocks, and deformations I: The components of two-dimensional shape and the reaction-diffusion space," *International Journal of Computer Vision*, vol. 15, no. 3, pp. 189–224, 1995.

[67] K. F. Koral, Y. Dewaraja, L. A. Clarke, J. Li, K. R. Zasadny, and S. G. Rommelfanger, "Tumor absorbed dose estimates versus response in tositumomab therapy of previously-untreated patients with follicular non-Hodgkin's lymphoma: preliminary report," *Cancer Biotherapy and Radiopharmaceuticals*, vol. 15, no. 4, pp. 347–355, 2000.

[68] K. F. Koral, Y. Dewaraja, J. Li, S. Lin, C. L. Barrett, and D. D. Regan, "Initial results for hybrid SPECT-conjugate-view tumor dosimetry in I-131 anti-B1-antibody therapy of previously-untreated lymphoma patients," *Journal of Nuclear Medicine*, vol. 41, no. 9, pp. 1579–1586, 2000.

[69] E. L. Kramer, M. E. Noz, J. J. Samger, A. J. Megibow, and G. Q. Maquire, "CT-SPECT fusion to correlate radiolabeled monoclonal antibody uptake with abdominal CT findings," *Radiology*, vol. 172, pp. 861–865, 1989.

[70] D. J. Kriegman and J. Ponce, "On recognizing and positioning curved 3-D objects from image contours," *IEEE Transactions on Pattern Analysis and Machine Intelligence*, vol. 12, no. 12, pp. 1127–1137, 1990.

[71] M. E. Leventon, W. E. L. Grimson, and O. Faugeras, "Statistical shape influence in geodesic active contours," in *Proceedings IEEE Conference on Computer Vision and Pattern Recognition*, volume 1, pp. 316–323, Jun. 2000.

[72] L. Liu, P. H. Bland, D. M. Williams, B. G. Schunck, and C. R. Meyer, "Application of robust sequential edge detection and linking to boundaries of low contrast lesions in medical images," in *Proceedings CVPR '89*, pp. 582–587, 1989.

[73] X. Lv, J. Zhou, and C. Zhang, "A novel algorithm for rotated human face detection," in *Proceedings IEEE Conference on Computer Vision and Pattern Recognition. CVPR 2000*, volume 1, pp. 13–15, June 2000.

[74] G. Q. Maguire, M. E. Noz, H. Rusinek, J. Jaeger, E. L. Kramer, J. J. Sanger, and G. Smith, "Graphics applied to medical image registration," *IEEE Computer Graphics and Applications*, vol. 11, no. 2, pp. 20–8, 1991.

[75] R. Malladi, J. Sethian, and B. Vemuri, "Shape modelling with front propagation: A level set approach," *IEEE Trans. on Pattern Analysis and Machine Intelligence*, vol. 17, no. 2, pp. 158–174, 1995.

[76] A. Matheny and D. B. Goldgof, "The use of three and four dimensional surface harmonics for rigid and nonrigid shape recovery and representation," *IEEE Transactions on Pattern Analysis and Machine Intelligence*, vol. 17, no. 10, pp. 967–981, Oct. 1995.

[77] T. McInerney and D. Terzopoulos, "Deformable models in medical image analysis," in *Proceedings of the IEEE Workshop on Mathematical Methods in Biomedical Image Analysis*, pp. 171–180, San Francisco, CA, USA, June 1996.

[78] T. McInerney and D. Terzopoulos, "Topology adaptive deformable surfaces for medical image volume segmentation," *IEEE Transactions on Medical Imaging*, vol. 18, no. 10, pp. 840–850, Oct. 1999.

[79] M. Merickel, "3D reconstruction: the registration problem," *Computer Vision, Graphics, and Image Processing*, vol. 42, no. 2, pp. 206–219, 1988.

[80] C. R. Meyer, J. L. Boes, B. Kim, P. H. Bland, K. R. Zasadny, P. V. Kison, K. F. Koral, K. A. Frey, and R. L. Wahl, "Demonstration of accuracy and clinical versatility of mutual information for automatic multimodality image fusion using affine and thin-plate spline warped geometric deformations," *Medical Image Analysis*, vol. 1, no. 3, pp. 195–206, Apr. 1997.

[81] D. Mumford and J. Shah, "Optimal approximation by piecewise smooth functions and associated variational problems," *Communications on pure and applied mathematics*, vol. 42, pp. 577–685, 1989.

[82] A. F. Nikiforov, S. K. Suslov, and V. B. Uvarov, *Classical Orthogonal Polynomials of a Discrete Variable*, Springer-Verlag, 1991.

[83] S. A. Orszag, "Fourier series on spheres," *Monthly Weather Review*, vol. 102, pp. 56–75, 1974.

[84] S. J. Osher and J. A. Sethian, "Fronts propagation with curvature dependent speed: Algorithms based on Hamilton-Jacobi formulations," *Journal of Computational Physics*, vol. 79, pp. 12–49, 1988.

[85] K. A. Paton, "Conic sections in chromosome analysis," *Pattern Recognition*, vol. 2, , 1970.

[86] E. Persoon and K. S. Fu, "Shape discrimination using Fourier descriptors," *IEEE Transactions on Pattern Analysis and Machine Intelligence*, vol. 8, no. 3, pp. 388–397, May 1986.

[87] R. Piramuthu, *Robust Fusion of MRI and ECT Data, and Acceleration of EM Algorithm Using Proximal Point Approach*, PhD thesis, The Univ. of Michigan, Ann Arbor, May 2000.

[88] W. H. Press, B. P. Flannery, S. A. Teukolsky, and W. T. Vetterling, *Numerical Recipes in C: The Art of Scientific Computing*, Cambridge University Press, 1988.

[89] D. Rockmore, "Computation of Fourier transforms on the symmetric group," in *Computers and mathematics*, pp. 156–165, Springer, 1989.

[90] C. Scarfone. *Single Photon Emission Computed Tomography*. http://www.bae.ncsu.edu/bae/course/bae590f/1995/scarfone, 1995.

[91] M. D. Srinath, *Introduction to Statistical Signal Processing with Applications*, Prentice Hall, 1996.

[92] L. H. Staib and J. S. Duncan, "Parametrically deformable contour model," in *Proceedings IEEE Conference on Computer Vision and Pattern Recognition (CVPR)*, pp. 98–103, 1989.

[93] L. H. Staib and J. S. Duncan, "Model-based deformable surface finding for medical images," *IEEE Transactions on Pattern Analysis and Machine Intelligence*, vol. 15, no. 5, pp. 1996, Oct. 1996.

[94] H. Stark and J. W. Woods, *Probability, Random Processes, and Estimation Theory for Engineers*, Prentice Hall, second edition, 1994.

[95] P. Taylor, "Invited review: computer aids for decision-making in diagnostic radiology - a literature review," *British Journal of Radiology*, vol. 68, pp. 945–957, 1995.

[96] D. Terzopoulos and D. Metaxas, "Dynamic 3D models with local and global deformations: Deformable superquadrics," *IEEE Transactions on Pattern Analysis and Machine Intelligence*, vol. 13, no. 9, pp. 703–714, July 1991.

[97] S. R. Titus, *Improved Penalized Likelihood Reconstruction of Anatomically Correlated Emission Computed Tomography Data*, PhD thesis, The Univ. of Michigan, Ann Arbor, Dec. 1996.

[98] Unknown, editor, *Mathematics Handbook*, China Science Publisher, 1992.

[99] B. C. Vemuri and Y. Guo, "Snake pedals: Compact and versatile geometric models with physics-based control," *IEEE Transactions on Pattern Analysis and Machine Intelligence*, vol. 22, no. 5, pp. 445–459, May 2000.

[100] P. Viola and W. M. Wells III, "Alignment by maximization of mutual information," in *Proceedings of IEEE International Conference on Computer Vision*, pp. 16–23, Los Alamitos, CA, Jun. 1995.

[101] R. G. Voigt, D. Gottlieb, and M. Y. Hussaini, *Spectral Methods for Partial Differential Equations*, Society for Industrial and Applied Mathematics, Philadelphia, 1984.

[102] D. H. Von Seggern, *PHB practical handbook of curve design and generation*, CRC Press, 1994.

[103] Y. Wang and L. H. Staib, "Elastic model based non-rigid registration incorporating statistical shape information," in *Medical Image Computing and Computer Aided Intervention*, pp. 1162–1173. Springer, 1998.

[104] E. T. Whittaker, *A course of modern analysis; an introduction to the general theory of infinite processes and of analytic functions; with an account of the principal transcendental functions*, Cambridge The university Press, 1950.

[105] E. Wigner, *Group Theory and its Application to Quantum Mechanics of Atomic Spectra*, Academic Press, New York, 1959.

[106] W. Y. Wu and M. J. J. Wang, "Elliptical detection by using its geometric properties," *Pattern Recognition*, vol. 26, no. 10, pp. 1499–1509, 1993.

[107] C. Xu, *Deformable Models With Application to Human Cerebral Cortex Reconstruction from Magnetic Resonance Images*, PhD thesis, The Johns Hopkins University, 2000.

[108] C. Xu and J. L. Prince, "Snakes, shapes, and gradient vector flow," *IEEE Trans. on Image Processing*, vol. 7, no. 3, pp. 359–369, March 1998.

[109] C. Xu, A. Yezzi, and J. L. Prince, "On the relationship between parametric and geometric active contours," Technical Report ECE 99-14, Johns Hopkins University, Dec. 1999.

[110] M. I. Yadrenko, *Spectral theory of random fields*, Optimization Software, 1983.

[111] S. Y. K. Yee, "Studies on Fourier series on spheres," *Monthly Weather Review*, vol. 108, pp. 676–678, 1980.

[112] S. Y. K. Yee, "Solution of Poisson's equation on a sphere by truncated double Fourier series," *Monthly Weather Review*, vol. 109, pp. 501–505, 1981.

[113] R. K. K. Yip, K. S. Tam, and D. N. K. Leung, "Modification of hough transform for circles and ellipses detection using a 2-dimensional array," *Pattern Recognition*, vol. 25, no. 9, pp. 1007–1022, 1992.

[114] A. C. Zaanen, *Linear Analysis*, North Holland, 1956.

[115] Y. Zhang, M. Brady, and S. Smith, "Segmentation of brain MR images through a hidden markov random field model and the expectation-maximization algorithm," *IEEE Trans. on Medical Imaging*, vol. 20, no. 1, pp. 45–57, Jan. 2001.

[116] S. C. Zhu, Y. Wu, and D. Mumford, "Filters, random fields and maximum entropy (frame): Towards a unified theory for texture modeling," *International Journal of Computer Vision*, vol. 27, no. 2, pp. 107–126, 1998.